A New Stokes-Einstein Relation for Size Determination of Nanoparticles

Xinli Zhang
orcid.org/0000-0001-9245-9414

A thesis presented for the degree of
Doctor of Philosophy

June 2017

School of Chemistry
The University of Melbourne
Parkville, Victoria, Australia

Submitted in total fulfilment of the requirements
of the degree of Doctor of Philosophy

Abstract

Hydrodynamic size of sub-10 nm particles determined by the Stokes-Einstein relation (SER) is typically twice their structural size. Recent studies found that viscosity of liquids near a surface is larger than that of the pure liquids. In Chapter 2, thus we assume that an increased local viscosity exists around diffusing particles, a few nanometers in size, in order to derive a new SER. A new expression for the hydrodynamic size is then obtained by solving the Naiver-Stokes equations to the leading order based on the assumption, instead of using the viscosity of pure solvent which results in the traditional SER. This new theory could improve the accuracy of size determination for nanoparticles.

Molecular dynamics simulations of simple nanoparticles and dendrimers in Lennard-Jones liquids are performed to test the new SER. Then the diffusion coefficient of solutes and viscosity of solvent are calculated from time correlation functions to obtain the hydrodynamic radius (r_h) by the traditional SER. We find that the r_h of particles with rough surface and high internal density grows faster than the true size. This suggests deviation of the traditional SER. The deviation is consistent with the increases in viscosity found by applying the new SER to the simulated simple particles. Experimental size data of cadmium selenide (CdSe) quantum dots in literatures is also discussed in Chapter 2. Appropriate agreement between the experiments, simulations and the new theory is found. The assumption of increased local viscosity is independently confirmed by persistence times of solvent particles, with motions regarded as a continuous-time random walk (CTRW). It has been reported that these time intervals, obtained from the sampled trajectories by simulations, are proportional to the local viscosities. We detect changes in the viscosity of solvent near the simple nanoparticles and dendrimers. The shear viscosity of solvent is found between 1.5 and 2.5 times of the pure solvent viscosity.

The new Stokes-Einstein relation is further tested in Chapter 3 by more realistic models, which are alkanethiol ligand grafted gold nanoparticles in water. The gold nanoparticle/water systems are investigated by the nanoscale molecular dynamics simulation. We employ the persistence times method to estimate shear viscosity of water near the diffusing gold nanoparticles with the same procedures applied to the simple models in Chapter 2. A similarly increasing pattern of viscosity near the grafted nanoparticles with that near the simple nanoparticles without ligands grafted on the surface is then detected. But the increases near the grafted nanoparticles are larger that near the bare ones. This implies that the ligands strengthen deviation from the SER according to the mechanism we proposed. We further discuss simulation of nanoparticles with ligands, literature data on grafted nanoparticles in different solvents, and the new Stokes-Einstein relation. Local viscosities inferred from the new theory are consistent with those estimated from the persistence times. With the known parameters for the new theory, structural sizes of the gold nanoparticles with ligands are predicted successfully. The role of ligands on the deviation from the SER is then confirmed by hydrodynamic-structural radii curves of grafted and bare nanoparticles.

We further investigate the dendrimers simulated in Chapter 2 to explore generality of the new SER in Chapter 4. Two sequences of dendrimers are examined, which are dendrimers of a single generation with growing branch length, and dendrimers of a fixed short branch length with growing generations. Local hydrodynamics of solvent near the simulated dendrimers is estimated by persistence times and exchange times using a different analysis method from that applied in Chapter 2 and 3. There are no evident changes in the local hydrodynamics found near the dendrimers of a single generation, while the local dynamics slows down near those of growing generations. The changing pattern in viscosity near the latter is similar with that near nanoparticles studied in Chapter 2 and 3. This suggests the generality of

the new theory. That the dendrimers of a single generation obey the traditional SER and those of increasing generations deviate from it is consistent with the changes in the local hydrodynamics according to our assumption for the breakdown of SER. The new theory is then applied to the dendrimers and it is tested to be able to predict sizes of the dendrimers accurately. In addition, experimental data of complex dendrimers is also included to verify our simulation results.

The studies we present in this thesis are performed with a view to improving size determination of objects up to 10 nm by the new Stokes-Einstein relation. We propose that mechanism for the deviation of SER is an increased local viscosity of solvent near a diffusing solute in viscous liquids and obtain a new SER. Application of the new theory is neither sensitive to the surface structures of the particles, nor the nature of interactions between the particle and surrounding solvent. It could be applied to a wide range of sub-10 nm particles, especially important to ligand-coated nanoparticles.

Declaration

This is to clarify that:

(i) The thesis comprises only my original work towards the PhD except where indicated in the preface;

(ii) Due acknowledgement has been made in the text to all other material used;

(iii) The thesis is fewer than 100,000 words in length, exclusive of tables, maps, bibliographies and appendices.

Xinli Zhang

Preface

This thesis contains work that has been published or submitted for publication:

(1) **Zhang, X.**, Tran, S., Gray-Weale, A. A. The hydrodynamic drag on diffusing nanoparticles for size determination. *J. Phys. Chem. C*, 120, 21888-21896, **2016**.

(2) **Zhang, X.**, Gray-Weale, A. A. Local hydrodynamics of solvent near diffusing dendrimers: A test of the new Stokes-Einstein relation. *J. Polym. Sci. B: Polym. Phys.*, 2017, 55, 1380-1391.

(3) **Zhang, X.**, Gray-Weale, A. A. Determination of gold nanoparticle sizes by a new Stokes-Einstein relation. In submission.

The candidate was the primary author and contributed $>$ 50% of the content in these publications. The candidate reviewed literatures, made research plans and carried out numerical simulations. The candidate analysed the data from simulations and prepared the manuscripts under the supervision of Dr. Angus Gray-Weale. Cauchy's equation was solved in Chapter 2 with the help of Dr. Angus Gray-Weale. He also helped with the language editing throughout the thesis.

Acknowledgements

I am grateful to all who have helped me with the project presented in this thesis. First and foremost, I would like to thank my supervisor Dr. Angus Gray-Weale. He always guides me with incredible patience throughout my research. I thank his continuous encouragement when I was anxious and I also thank his strong support on my ideas of the project. I thank his great suggestions and guidance on my thesis.

I would also like to thank my supervisor Dr. Alessandro Soncini. He is always there to talk with me with great patience. This helps me to quickly recover from depression especially during the last few months of my PhD candidate. I thank him for providing suggestions on my completion seminar slides and my thesis.

I would also like to thank my advisory committee members Prof. Paul Mulvaney and Dr. Georgina Such for great suggestions and comments on my project during the last three and half years. I especially appreciate the collaboration with Prof. Paul Mulvaney, where I obtained my chance working on this project.

I thank the Victorian Life Sciences Computation Initiative (VLSCI) and National Computational Infrastructure (NCI) for the grant of computing time. I would like to express my appreciation and thanks to Dr. Michael Kuiper and Jin Zhang who work for the Computing Facility in VLSCI for the great suggestions on the technical problems.

Special thanks to my family and friends. Thank you for being around all the time and helping me relax when I was extremely stressful. I thank you for supporting me consistently.

Contents

Nomenclature and Abbreviations

a	Radius of an idealised spherical particle
AFM	Atomic force microscope
AMBER	Assisted model building with energy refinement
AuNP-x	A passivated gold nanoparticles with x atoms of the core
α	Largest surface viscosity increase
CHARMM	Chemistry at Harvard Macromolecular Mechanics
COM	Center of mass
CTRW	Continuous-time random walk
D	Diffusion coefficient
DLS	Dynamic light scattering
$D(r)$	Local diffusion coefficient at position r
$\delta\zeta$	Perturbations in friction coefficient
$\delta\eta$	Perturbations in viscosity
δf	Perturbations in body force
Δ	Dimensionless increases in viscosity
ϵ	Interaction force parameter
F_d	Drag force
f_i	A component of a body force
ζ	Friction coefficient
G	Generation of dendrimers
GK	Green-Kubo expressions
G1-1,2,3,4	Four dendrimers of a single generation with different branch length 1, 2, 3 and 4
G1,2,3,4-1	Four dendrimers of fixed short branch length with different generations 1, 2, 3 and 4
η	Viscosity of solvent
η^{local}	Local viscosity of solvent
η^{bulk}	Viscosity of bulk solvent
η_0	Viscosity of pure solvent
$\eta(r)$	Local viscosity at position r
k	Boltzmann constant
L	Length of the simulation box

MD	Molecular dynamics
MSD	Mean-squared displacement
n	Boundary conditions coefficient
NAMD	Nanoscale molecular dynamics
NPs	Nanoparticles
NPT	Isothermal-isobaric ensemble
NVT	Canonical ensemble
N_r	Total number of solvent particles inside a bin at position r
OPLS	Optimized potentials for liquid simulations
QDs	Quantum dots
σ	Length parameter
r	Distance from the center of mass of a particle
R_g	Radius of gyration
r_h	Hydrodynamic radius
$\hat{r_h}$	New hydrodynamic radius
s	Radius of solvent particles
SER	Stokes-Einstein relation
SV-AUC	Sedimentation velocity analytical ultracentrifugation
T	Absolute temperature
TEM	Transmission electron microscopy
T_g	Glass transition temperature
t_p	Persistence time
$\langle t_p \rangle_r^{har}$	Harmonic average of persistence times at a distance r
$\langle t_p \rangle_r^{arith}$	Arithmetic average of persistence times at a distance r
TraPPE	Transferable potentials for phase equilibria
t_x	Exchange time
$\langle t_x \rangle_r^{har}$	Harmonic average of exchange times at a distance r
$\langle t_x \rangle_r^{arith}$	Arithmetic average of exchange times at a distance r
UA	United-atom
U_{ij}	Potential energy exerted between two atoms i and j

List of Figures

List of Tables

Chapter 1

Introduction

1.1 Stokes-Einstein relation

The Einstein relation, a kinetic relation, was revealed independently by Albert Einstein,[1] William Sutherland[2] and Marian Smoluchowski at the start of the 20th century.[3] It describes the mobility of particles undergoing random motions in liquids,[4, 5] which are referred as Brownian motion observed by Brown in 1828.[6] The motion of particles results from fluctuating collisions of liquid molecules.[7] The random motions are treated as diffusive when the mean-squared displacement (MSD) is proportional to the time t taken by the particle,[7]

$$\langle [\vec{r}(t) - \vec{r}(0)]^2 \rangle = 6Dt, \tag{1.1}$$

where D is the diffusion coefficient of the particle. Consider a diffusing solute with a constant velocity in a viscous fluid of relatively smaller particles. Two forces exerted on the solute are in balance. One force results from the random buffeting on the solute by the small liquid particles.[8] The other contribution is a friction force acted by the viscous liquid, which is also termed drag force. The drag force is in the opposite direction of the velocity, and the

magnitude of the drag force is proportional to that of the velocity,

$$F_d = \zeta v, \tag{1.2}$$

where F_d is the drag force, ζ is the friction coefficient, and v is the velocity of solute. The frictional force results from both Brownian motions and viscous dissipation according to the fluctuation-dissipation theorem.[9, 10] The relation between friction coefficient and diffusion coefficient is expressed by the Einstein relation,

$$D = \frac{kT}{\zeta}, \tag{1.3}$$

where k is the Boltzmann constant and T is the absolute temperature.

The frictional force coefficient (ζ), which is related to the size of a spherical solute diffusing in a viscous liquid as shown in Figure 1.1, was derived by George Gabriel Stokes in 1851.[11] The expression for the relation was obtained by solving the Naiver-Stokes equations for a laminar flow with a small Reynolds number.[12] A laminar flow is a fluid moving in steady motions at low velocities. The flow passes parallel to the surface of a solid particle and the layers in the fluid pass each other without cross-current.[13] Reynolds number (Re) is a dimensionless parameter to measure flow patterns in various flow situations,

$$Re = \frac{\rho u L}{\mu}, \tag{1.4}$$

where ρ is the fluid density, u is the relative velocity of fluid and solute, L is the diameter of a spherical solute and μ is the dynamic viscosity of the fluid. For a sphere in a fluid, the laminar flow occurs when the Reynolds number is up to 10.[14]

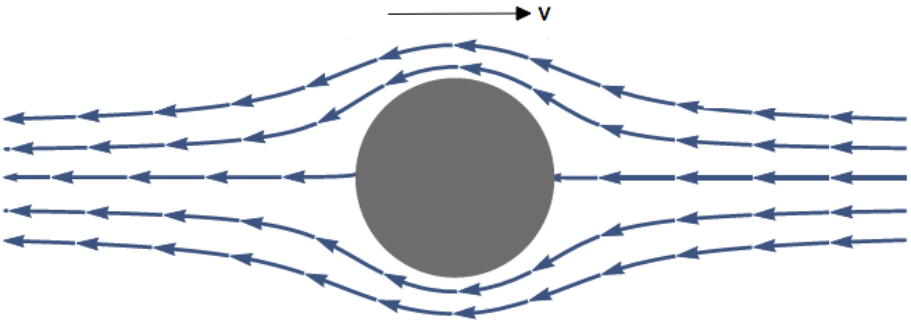

Figure 1.1: A spherical particle diffuses at a velocity of v in a flow with a low Reynolds number.

Two types of friction coefficients were solved due to different boundary conditions between the particles and fluid.[15, 16] If there is only normal force exerted on the particle by the fluid and the relative fluid velocity at the interface of solute-solvent reduces to zero only in the normal direction, slip boundary conditions apply. While if both tangential and normal forces exist and the relative fluid velocity reduces to zero in both tangential and normal directions, stick boundary conditions apply. Here the friction coefficients are expressed by a universal equation for both slip and stick conditions, which is Stokes' law,

$$\zeta = n\pi\eta R, \tag{1.5}$$

where $n = 4$ for the slip boundary conditions, $n = 6$ for the stick boundary conditions, η is the viscosity of pure fluid and R is the radius of a particle. The Stokes-Einstein relation (SER) is then obtained by substituting the friction coefficient ζ, expressed by Stokes' law (eq. 1.5), to the Einstein relation (eq. 1.3),

$$D = \frac{kT}{n\pi\eta R}. \tag{1.6}$$

The size measured by the Stokes-Einstein relation is termed hydrodynamic radius or Stokes'

radius r_h,

$$r_h = \frac{kT}{n\pi\eta D}. \tag{1.7}$$

The Stokes-Einstein relation is a classic method to determine sizes of macroscopic particles diffusing in much smaller and lighter solvent particles[17] such as polystyrene spheres in dilute aqueous solutions[18] and silica particles in cyclohexane.[19] The SER is also used to predict the self-diffusion coefficient of particles in pure liquids of high density.[20–22] Later the SER was frequently applied to particles in microscale level or non-continuum mediums where the SER holds only under certain conditions. For example, Michele[23] reported that the SER is valid for particles in diatomic molecular liquids only at high temperatures; and Liu[24] reported that the SER can be successfully applied to nanoparticles in polymer melts only when their sizes are larger than those of polymer chains in the matrix.

1.2 Size measurement for nanoparticles

1.2.1 Application of nanoparticles

Nanoparticles, with a size range of 1-100 nm, have received growing attention due to their applications in research and industry such as nanocomposites, dendrimers and quantum dots. Polymeric nanoparticles are used as drug delivery with advantages, including stability of drug during transportation, reduced side effects, sustainable release, high drug loading, preservation of drug activity and precise targeting,[25–27] over the potential carriers of liposomes. Gold nanoparticles possess more potential applications apart from the drug delivery because of their tunable optical,[28] charging[29] and catalytic[30] properties. Functionalized gold nanoparticles have been used for therapeutic applications,[28] electron transistors[31] and enzyme mimics.[32] Dendrimers, which are highly branched polymers, have also been extensively applied to medicines.[33–35] For example, peptide dendrimers have been applied as antigens

for immunoassays and they are used to detect antibodies for serodiagnosis. The dendrimers have promising applications as inhibitors, mimetics and immunogens.[36] Quantum dots are used as electronic materials[37] because of the strong stability and long-term brightness. They also have biological applications, such as targeting and imaging cancer cell in living tissue of animals.[38–40]

Most of the properties of nanoparticle are size dependent,[41, 42] such as diffusion, electronics, magnetics, catalytic activity and optics. The properties dominate the application of nanoparticles. The diffusive motions are influenced dramatically by the size of particles and they are crucial for biological functionalities in a liquid environment,[43, 44] such as targeting, releasing and imaging. The importance of size determination is, therefore, born out. In order to predict properties of nanoparticle, design a particular function and meet the increasing requirements from research and industry, accurate size measurement is demanded.[31]

1.2.2 Equipments for size measurement

The methods of dynamic light scattering (DLS) and sedimentation velocity analytical ultracentrifugation (SV-AUC) are used to study the size distributions of nanoparticles in liquids.[45, 46] They are widely applied to biology, pharmacy, physics and chemistry.[47, 48]

Dynamic light scattering

The DLS techniques mainly include photon correlation spectroscopy (PCS)[49, 50] and depolarized Fabry-Perot interferometry (FPI).[51–53] The crucial step to determine the size of nanoparticles is measuring the translational coefficient for PCS and rotational diffusion coefficient for FPI, respectively. Here we limit our discussion to PCS only. The translational diffusion coefficient (D) is calculated from scattered intensity signals, which are reflected by

nanoparticles in a diluted solution,[48]

$$g^{(1)}(t) = e^{-q^2 Dt}, \tag{1.8}$$

where $g^{(1)}(t)$ is the normalized time autocorrelation of scattered electric field in its first order and q is the length of the scattering vector. $g^{(1)}(t)$ can be calculated from,

$$C(t) = \frac{\langle I(t)I(0)\rangle}{\langle I(0)I(0)\rangle} = [1 + \gamma[g^{(1)}(t)]^2], \tag{1.9}$$

where $C(t)$ is the time correlation of the scattered intensity and γ is an experimental constant.[54, 55] q in eq. 1.8 is given by,

$$q = \frac{4\pi}{\lambda} \sin \frac{\theta}{2}, \tag{1.10}$$

where λ is the wavelength of the light in the scattering medium and θ is the scattering angle.[48, 56] The radius (R) of spherical nanoparticles can be calculated by the Stokes-Einstein relation (eq. 1.6) together with the translational diffusion coefficient measured by the PCS experiments.

Sedimentation velocity analytical ultracentrifugation

The SV-AUC has become a modern method to measure the size of nanoparticles, proteins and quantum dots. The measurement is based on the fractionation technique. It can detect any minute changes in mass, density and shape of the nanoscale particles in the original solvent without dilution. The facts that the measurement is non-intrusive and the sample can be recovered afterwards make the method powerful. It allows characterization of the hydrodynamic properties, which determines both sedimentation coefficient s and diffusional

coefficient D of every particle.[57] The two coefficients are related by the Svedberg equation,[58]

$$s = \frac{u}{w^2 r} = \frac{DM(1 - \bar{v}\rho_s)}{RT}, \tag{1.11}$$

where u is the observed terminal velocity of a particle, w is the angular velocity of the rotor, r is the radial distance, M is the molecular mass, R is the gas constant, $\bar{v}$ is the partial specific volume which is the inverse particle density and ρ_s is the solvent density. The s is in Svedberg Units (S) with $1S$ being 10^{-13} *sec*.

The diffusion coefficient D of spherical compact particles can be expressed by the Stokes-Einstein relation,

$$D = \frac{RT}{6\pi\eta N_A r_h}, \tag{1.12}$$

where η is the viscosity of solvent, N_A is the Avogadro's number and r_h is the hydrodynamic radius. Equation 1.12 is derived from equation 1.6 by using the following relation,

$$kT = \frac{RT}{N_A}. \tag{1.13}$$

The sedimentation coefficient is directly related to the effective size of the nanoparticles by combining eq. 1.11 and 1.12,[59]

$$s = \frac{M(1 - \bar{v}\rho_s)}{6\pi\eta N_A r_h}. \tag{1.14}$$

If the nanoparticles are treated in dilute solutions without considering interactions among them and the mass of a single nanoparticle is M/N_A, the Svedberg equation eq. 1.14 can be rearranged to be,

$$s = \frac{2r_h^2}{9\eta}(\rho_p - \rho_s), \tag{1.15}$$

where η is the viscosity of solvent, ρ_p is the density of particle, and ρ_s is the density of solvent. Therefore, the size determination of nanoscale particles can be achieved by measuring the sedimentation coefficient using eq. 1.14 or eq. 1.15.

1.2.3 Role of Stokes' law on size determination

As seen from the mechanism of size measurement for both the DLS and SV-AUC, the Stokes-Einstein relation is fundamental. The validity of the two methods for size measurement is based on the assumption that the SER is valid down to a few nanometers. For example, Carney and coworkers[42] assumed that the Stokes' diameter approximately equals to the diameter of $Au_{144}(SR)_{60}$ nanoclusters when determining the size distributions using the 2D AUC. Hong[60] also used the hydrodynamic radius of coated nanoparticles calculated by the SER as the structural radius for an estimation of the viscosity of solvent. When it comes to calculating the thickness of ligands on the surface of nanoparticles, the hydrodynamic radius is assumed to be the total structural radius of the particle.[61–63] The thickness is usually obtained from the difference between the hydrodynamic radius and the radius of cores measured by the transmission electron microscopy[64] (TEM).

However, deviations from the SER for particles up to 10 nm were found by both experimental and numerical research. Diffusion coefficient of cadmium selenide nanoparticles diffusing in a polymeric liquid predicted by the SER was found approximately 200 times slower than that measured by the X-ray photo correlation spectroscopy[65] (XPCS). Later a critical size where the SER breaks down for bare nanoparticles in simple liquids was reported to be a few nanometers by molecular dynamics simulation.[17] Walser[66] also found that the product of diffusion coefficient and viscosity of water varies as the mass of water increases. However, the product should be independent of mass if the SER works. Note here that the Einstein relation is not in question, and the failure of SER comes from Stokes' law.

The non-ideal diffusive behaviours could result from the ignorance of factors including liquid densities, concentration, charges and the relative sizes of solute and solvent. Cappelezzo and Coworkers[22] reported that when the pure simple fluids are at reduced density of 0.20, the boundary conditions coefficient n in Stokes' law is lower than 4. This means that the diffusion coefficient of a particle diffusing in the simple pure liquids predicted by the Stoke's law is underestimated. Liu and coworkers[24] investigated the influence of particles concentration on the diffusive behaviour. They found that the diffusion coefficients are underestimated by the Stoke's law when the volume fraction of nanoparticles is smaller than 0.2 and the diffusion is overestimated when the volume fraction is higher than 0.2. The charges also influence the diffusion of particles. It was found that the gold nanoparticles with positive charges diffuse much faster than the negatively charged gold nanoparticles of the same size.[67] However, the diffusion coefficients of the two nanoparticles calculated by Stokes' law should be the same due to the fact that they were studied under the same conditions except the charges. The relative size of solute and solvent particles also affects the diffusivity of the solute. It was reported that when the size of nanoparticles is in the same size of polymer chains in the matrix or even smaller, the diffusion coefficient is underestimated by Stokes' law.[24, 68] Careful considerations of the above factors should be made when applying the Stokes-Einstein relation to other molecular models, such as supercooled liquids, quantum dots in simple liquids, polymers in polymer matrix and proteins in water.

1.3 Prior studies on Stokes' law for nanoparticles

The validity of Stokes' law has been examined by both simulations and experiments. Researchers found that it breaks down for supercooled liquids,[20, 69–72] hard sphere fluids,[73] polymers,[72] dendrimers,[74] proteins,[75, 76] quantum dots[57, 77] and nanocomposites.[17, 65] Here we discuss nanoscale solutes in a solvent from two size regimes. The small size regime is

referred when the solute is smaller than the solvent particles; while the large size regime is referred when the solute is larger than the solvent particles. The breakdown of Stokes' law happens under both of the two conditions, and possible origins are discussed in the following.

1.3.1 Prior studies on small size regime

The matrix for nanocomposites is usually a polymeric liquid with chemical chains identical with that of ligands on the nanoparticle. This is due to that the interaction between the nanoparticle and matrix is the same as that between the polymers in the matrix.[78] For example, polystyrene (PS) nanoparticles are distributed in linear polystyrene[78] and poly(vinyl chloride) (PVC)/calcium carbonate ($CaCO_3$) nanocomposites are dispersed in PVC matrix.[79] Systems of polymer grafted nanoparticles in polymer melts were studied by theory and modeling for structural and hydrodynamic properties.[80–82] Note here we focus on the hydrodynamics. The prior studies indicate that the relative size of nanocomposites and free polymers in the matrix is a crucial indicator for the validity of Stokes' law. Liu and coworker[24] found that the SER underestimates the diffusion coefficient of nanoparticles in polymer melts when the nanoparticle radius is smaller than the gyration radius (R_g) of the free polymers in the matrix by molecular dynamic (MD) simulations. Later, Egorov[68] reported the same conclusion by both a mode-coupling theory and MD simulations.

The failure of Stokes' law is also supported by experimental observations. Tuteja and coworkers[65] reported that the SER underestimates the diffusion coefficients of quantum dots diffusing in polystyrene melts. The hydrodynamic radius of quantum dots is 4.7 nm and the gyration radius of polystyrene chains is ∼17 nm. Omari[83] later reported that the ratio of diffusion coefficients measured by the fluctuation correlation spectroscopy (FCS) to those predicted by the SER is two for gold colloids in a semidilute solution of entangled PS in toluene. The radius of gold colloids is ∼2.5 nm and the gyration radius of PS is ∼18 nm.

In the same year, Grabowski[84] independently found that the gold nanoparticles diffuse in poly(butyl methacrylate) (PBMA) melt ∼250 times faster than that predicted by the SER, where the gold particle size is smaller than the entanglement mesh length of long chains of PBMA.

Apart from the nanocomposites in polymer melts, Stokes' law also fails for small solutes in a simple solvent.[85] Pollack[86] studied xenon diffusing in n-octane, n-decane and n-tetradecane. He found that diffusion coefficients obtained from experimental methods are not consistent with that predicted from Stokes' law. Later, Kowert[87] reported slower diffusion calculated by Stokes' law for dioxygen in 1-alkenes and biphenyl in perfluoro-n-alkanes than the measured values. The deviations were also observed by using computational methods,[88–90] in qualitative agreement with that observed by using the experimental methods.

To explain the underestimation of diffusion by the Stokes-Einstein relation, the effective viscosity experienced by the diffusing solute in the polymer matrix is questioned and the local viscosity is believed to be smaller than the pure solvent viscosity applied to Stokes' law.[24, 85] The viscosity experienced by the small solute is microviscosity which is contributed by the friction of segments of polymers in the matrix, rather than the bulk viscosity which is contributed by the friction of polymer chains. The microviscosity is smaller than the bulk viscosity due to that the segments relax faster than the chains. For simple liquids, the breakdown of Stokes' law is thought being caused by the hopping motions of the solutes, which are similar to those of the supercooled liquids at the glass transition temperature (T_g).[73, 91, 92]

1.3.2 Prior studies on large size regime

Stokes' law has been widely applied to spherical solutes with macroscale sizes and the validity is well accepted. It works well when the size of nanoparticles is larger than that of polymer

chains in a melt matrix. However, it fails when the size of solute down to a few nanometers in the large size regime. The critical size where the breakdown happens is predicted by an MD simulation system of a bare nanoparticle in simple liquids.[17] Carney and coworkers[42] measured the hydrodynamic size of pentadecanethiol (PDT) capped gold nanoparticles in toluene, and found that the hydrodynamic size is about twice the size seen from the TEM. Lees and coworkers[77] determined the size of CdSe quantum dots (QDs) diffusing in aqueous media experimentally by both the TEM and Stokes-Einstein relation, and found the observed size of QDs from the TEM is much smaller than that from the SER. Demeler and coworkers[57] also reported that the effective size of both CdSe diffusing in 1-octadecene and PbS diffusing in octane, obtained from the SER, is much larger than that from the TEM. Halle and Pronk independently found that the diffusion of proteins in water is much slower than that calculated by the SER.[75, 76]

The measurement of nanoscale particles size by the SER is based on the hydrodynamics of solute and solvent. Note here it is the viscosity of pure solvent used in the SER. However, the viscosity of liquids near a surface has been found higher than that of the bulk liquid. The surface could be flat or curved, solid or soft.

In 2007, Li and coworkers[93] have done research on viscous water confined by subnanometer gaps using both experiments using atomic force microscope (AFM) and models using grand canonical molecular dynamics simulations. They found that the viscosity near hydrophilic surfaces, such as mica and glass, increased orders of magnitude, but there is no increase observed near hydrophobic surfaces, such as graphite. In the same year, Goertz and coworkers[94] reported that the increased viscosity of water near hydrophilic surfaces, such as amorphous silica, is $\sim 10^6$ times greater than the pure water viscosity. Three years later, a sharp viscosity increase of nanoconfined water films, which are less than 3-4 molecular lay-

ers, was observed by mechanical measurements.[95] The increase in viscosity near hydrophobic surfaces was also reported in 2013, but the effect are weaker than that near the hydrophilic ones. Ortiz-Young and coworkers[96] demonstrated an increased shear viscosity near solid flat surfaces by experiments using AFM and a modified Newtonian viscosity formula. They reported that the shear viscosity of water confined by the surfaces is about 3×10^4 times of the pure water. The surfaces they studied include both hydrophilic and hydrophobic surfaces. Hoang[97] correlated the increased viscosity of fluid near a solid surface positively to density inhomogeneities for both dilute and dense fluids by MD simulations.

Apart from the flat surfaces, spherical-like surfaces, especially proteins also confine the surrounding liquid, causing increases in the viscosity. It was proposed about a decade ago that the viscosity of water in the first hydration shell around a spherical protein could be different from that of the pure water.[75] The dynamics of water in the two regions were studied in femtosecond time resolution.[98] The relaxation time of bulk water was found to be $\sim$1 ps, while the water in the solvation shell at the surface of proteins of Subtilisin Carlsberg (SC) and Monellin relaxed slower consuming 38 ps and 16 ps, respectively.[98] The reason for the slower hydrodynamics is believed to be that a monolayer of water molecules are tightly bound at the surface of proteins.[99–102] Recently it was[76] demonstrated that the viscosity of water near a protein is about two times of that of bulk water and the viscosities were estimated by the persistence and exchange times method.

1.4 Molecular dynamics

1.4.1 Motion equations and trajectories

The molecular dynamics (MD) method is usually employed to study liquid systems for structures, hydrodynamics and thermodynamics. All of the targeted properties in this study

investigated by the MD method are obtained from the manipulation of individual trajectory of atoms, including positions and velocities. Motions of the atoms result from collisions among the surrounded atoms following Newton's second law,

$$m\vec{a_i} = \vec{F_i} = \sum_{\substack{j=1 \\ j\neq i}}^{N} \vec{F_{ij}}, \tag{1.16}$$

where m is the mass of atom i, $\vec{a_i}$ is the acceleration of the atom , $\vec{F_i}$ is the total force exerted on the atom, N is the number of surrounding atoms, and $\vec{F_{ij}}$ is the force of atom j exerted on atom i. In order to calculate the forces, the relation between the force and potential is involved,

$$\vec{F_{ij}} = - \bigtriangledown U_{ij}(r), \tag{1.17}$$

where U_{ij} is the potential exerted on the atom i by atom j, and r is the distance between the two atoms. The force parameters given in the simulation configuration files are referred as potential function parameters. The trajectories are then calculated by supercomputers using leapfrog integration,

$$v_{ix}(t + \Delta t/2) = v_{ix}(t - \Delta t/2) + \Delta t a_{ix}(t), \tag{1.18}$$

$$r_{ix}(t + \Delta t) = r_{ix}(t) + \Delta t v_{ix}(t + \Delta t/2), \tag{1.19}$$

where v_{ix}, r_{ix} and a_{ix} are the velocity, coordination and acceleration of atom i at the x direction, respectively, and Δt is the time interval. The coordinates are adjusted after each integration step using the periodic boundary conditions to resemble infinite systems,

$$r_{ix} = \begin{cases} r_{ix} - L_x & r_{ix} \geq L_x/2 \\ r_{ix} + L_x & r_{ix} < -L_x/2, \end{cases} \tag{1.20}$$

where L_x is the simulation box length in each direction. In this thesis, we adopt cubic box for all of the simulations. The adjustments can be explained in this way that if the atom moves out of the box, it is brought back by the two algorithms.

The equations of motion are energy preserved. The conventional MD produces properties based on the microcanonical (NVE) ensemble with the number of atoms, volume and energy fixed. However, in practical experiments, it is the temperature (T) and pressure (P) that are controlled but the energy is not conserved. New algorithms are thus needed in order to keep the targeted T and P. The Nosé-Hoover chain method is introduced to control the temperature in Chapter 2 and 4 for the canonical (NVT) ensemble. The equations of motion, which define the dynamics of Nosé-Hoover thermostat with a single chain, are constructed based on the conservation of probability in phase space,[103]

$$\dot{r} = \frac{p_i}{m_i}, \tag{1.21}$$

$$\dot{p_i} = F_i - p_i \frac{p_{\xi_1}}{Q_1}, \tag{1.22}$$

$$\dot{\xi_j} = \frac{p_{\xi_j}}{Q_j}, j = 1, ..., M, \tag{1.23}$$

$$\dot{p_{\xi_1}} = [\sum_{i=1}^{N} \frac{p_i^2}{m_i} - N_f k_B T] - p_{\xi_1} \frac{p_{\xi_2}}{Q_2}, \tag{1.24}$$

$$\dot{p_{\xi_j}} = [\frac{p_{\xi_{j-1}}^2}{Q_{j-1}} - k_B T] - p_{\xi_j} \frac{p_{\xi_{j+1}}}{Q_{j+1}}, \tag{1.25}$$

$$\dot{p_{\xi_M}} = [\frac{p_{\xi_{M-1}}^2}{Q_{M-1}} - k_B T], \tag{1.26}$$

where r, p and m are the position, momentum and mass of the i th particle, respectively, ξ is a dimensionless degree of freedom with an associated effective mass Q, Q determines strength of the thermostat, p_ξ is the corresponding conjugate momentum, M is the number

of thermostat on a chain and 5 is adopted in this study, N_f is the number of freedom degrees, and k_B is the Boltzmann constant. The basic idea of the algorithm is to scale the velocity by a friction-like factor $\frac{p_{\xi_1}}{Q_1}$ shown in the last term of eq. 1.22, which meets dynamics described by eq.1.24. The two equations reveal the mechanism of keeping the temperature constant. The friction-like factor changes to control the temperature according to the difference between the kinetic energy at instantaneous and the kinetic energy at target temperature. If the difference is positive, the factor increases; otherwise, it decreases.

Langevin dynamics is employed to control fluctuations in the temperature to approximate NVT ensembles in Chapter 3. The dynamic equations are performed for motions of solute in a continuum of small solvent particles,

$$\dot{r} = \frac{p_i}{m_i}, \tag{1.27}$$

$$\dot{p_i} = F_i - \gamma_i p_i + \sigma_i \xi_i, \tag{1.28}$$

where γ_i is the friction coefficient of a damping force, $-\gamma_i p_i$ is created by solvent particles as the solute passing through and pushing them away, and $\sigma_i \xi_i$ is the random force with dispersion σ_i. The random force results from random collisions between the small solvent particles and solute. In order to control the temperature, σ_i and γ are related by

$$\sigma_i^2 = 2\gamma m_i k_B T / \Delta t, \tag{1.29}$$

where Δt is the time step used for integration of the motion equations. Eq.1.29 is a fluctuation-dissipation relation because the heat energy generated by friction of the solute is the same as the kinetic energy of its random motions. The dissipation in energy is a reverse process of thermal fluctuations. Note here that we observe similar behaviours for the two

types of thermostat in this study mentioned above.

The combination of Langevin piston dynamics[104] and Nosé-Hoover constant pressure method[105] is employed to control pressure. The two methods together with the aforementioned temperature control method,which is called Langevin dynamics, are used to simulate isothermal-isobaric (NPT) ensemble in Chapter 3. The equations of motion, which define the combined dynamics for the pressure control, are

$$\dot{r_i} = \frac{p_i}{m_i} + \frac{p_\epsilon}{W} r_i, \tag{1.30}$$

$$\dot{p_i} = F_i - \frac{p_\epsilon}{W} p_i - \frac{p_\xi}{Q} p_i + R_i, \tag{1.31}$$

$$\dot{V} = 3V \frac{p_\epsilon}{W} \tag{1.32}$$

$$\dot{p_\epsilon} = 3V(P_{int} - P_{ext}) - \frac{p_{\xi c} p_\epsilon}{Q} + R_c, \tag{1.33}$$

$$W = 3N\tau^2 k_B T, \tag{1.34}$$

$$\langle R_i^2 \rangle = 2m_i \frac{p_\xi}{Q} k_B T / \Delta t, \tag{1.35}$$

$$\langle R_c^2 \rangle = 2W \frac{p_{\xi c}}{Q} k_B T / \Delta t, \tag{1.36}$$

where p_ϵ is the barostat momentum, W is the mass of a piston served by an additional degree of freedom of an extended system, R_i is the noise on the ith atom, V is the volume, P_{int} is the instantaneous pressure inside the simulation box, P_{ext} is the applied external pressure, $\frac{p_{\xi c}}{Q}$ is the friction-like factor on the piston and R_c is the noise on the piston.

Here in this thesis, the investigated properties, diffusion and viscosity, are time averaged behaviours, therefore, we adopt equilibrium simulations for the trajectories calculation. The equilibrium states are checked by the constant kinetic energy. At equilibrium, according to

the principle of equipartition, if we employ ensembles at a constant temperature, the kinetic energy per degree of freedom is

$$\langle \frac{1}{2} m v^2 \rangle = \frac{1}{2} kT, \tag{1.37}$$

where m is the mass of an atom, v is the velocity in one direction, k is the Boltzmann constant and T is the absolute temperature.

1.4.2 Force fields

Interatomic potentials are required when constructing models for molecular dynamics simulation. Parameters for the potential energy calculation, presented in the configurations files, are referred as force fields. A force field could be simple or complex, based on the resolution of simulated atoms.

In the simple force fields, atoms of a chemical group are represented by a single effective interaction site,[106, 107] which reduces degrees of freedom. The system without the chemical detail of atoms can be simulated to long time and length scales. Global features can be captured well in this way for molecules of complex structures. Chapter 2 and 4 will describe the construction of models of dendrimer and nanoparticle with the simple force fields.

Atomistic force fields include all-atom (AA)[108] and united-atom (UA)[109] force fields. The two force fields are chosen based on that whether the non-polar hydrogen atom placed at the carbon atom is considered individually or not for the interaction between atoms. In the AA force field, parameters are given for every atom, so the accuracy is ensured. It is only feasible for short time and length scale simulations. The force parameters are well developed for the AA force field. Programs defining these parameters are well developed, including CHARMM,[110] AMBER,[111] OPLS[112] and TraPPE.[113] In the UA force field, hydrogen atoms

of methyl and methylene groups are grouped together with the carbon atom to form a single interaction site. The above-mentioned programs for the AA force field are also developed for the corresponding versions of UA force fields. In Chapter 2 and 3, the UA force field is applied to the modeling of ligands of gold nanoparticles and the AA force field is applied to the modeling of water.

Both the simple and atomistic force fields possess advantages and disadvantages. None of them can simulate the realistic systems universally. Combinations of them become more and more important for a comprehensive improvement of the result by mapping or transferring them to each other. For instance, Harmandaris[114] reintroduced GROMOS atomistic model of polystyrene from its coarse-grained (CG) model and also reintroduced CG model from its atomistic model. Wassenaar and coworkers also back mapped MARTINI CG models to GROMOS and CHARMM36 atomistic models and tested this method by proteins and lipid bilayers.[115]

1.4.3 Transport properties

Transport properties, which are diffusion coefficient, shear viscosity and thermal conductivity, reflect the response of a system to an imposed driving force within the frame work of a continuum fluid. Here in this study, only the first two are calculated. The Green-Kubo (GK) expression was performed for the calculation,

$$\gamma = \int_0^\infty \langle A(t)A(0)\rangle dt, \tag{1.38}$$

where γ is the transport coefficient, which is diffusion coefficient if A is velocity or shear viscosity if A is pressure tensor. The other method for the calculation is the Einstein relations,

$$\langle[\vec{r}(t) - \vec{r}(0)]^2\rangle = 6\gamma_1 t, \tag{1.39}$$

$$\langle[mr(t)v(t) - mr(0)v(0)]^2\rangle = 6\gamma_2 t, \tag{1.40}$$

where $\vec{r}$ is the true position of a particle without the periodic boundary conditions considered, γ_1 is the diffusion coefficient of a particle, m is the mass of a particle, v is the velocity of a particle and γ_2 is the viscosity of liquid.

The two definitions for the transport properties are completely equivalent. However, practically the Einstein relation for viscosity is not stable under the periodic boundary conditions due to that discontinuities occur when particles cross the boundaries. This violates the assumption made during the original derivation. Modifications have been made to remove the violation,[116] but the applications are still limited. In this thesis, we adopt the GK expression for the calculation of shear viscosity of solvent and diffusion coefficients of solute in Chapter 2 and 4. We apply the Einstein relation for diffusion coefficients of solute in Chapter 3 due to that it demands much less storage than the GK method for atomistic systems.

1.5 Persistence and exchange time theory

Measurement of the transport properties for heterogeneous systems, such as supercooled liquid, needs to be performed locally. This is realized by two relaxation times of a particle during a continuous-time random walk. The relaxation times can scale with the diffusion coefficient and viscosity locally. The two characteristic times are persistence time, t_p, and exchange time, t_x. The t_p is the mean first passage time of a particle starting at a random

position, and t_x is the waiting time between two random walk jumps, as shown in Fig 1.2.

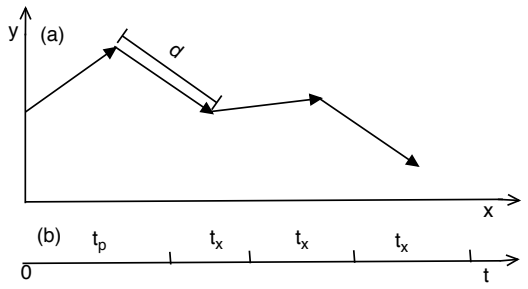

Figure 1.2: (a) Motions of a particle with fixed jump length d; (b) Persistence time and exchange time of a particle starting at a random position.

The two time scales are calculated as the time a particle traveling a fixed length as shown in Figure 1.2. The fixed jump length is chosen as the size of a solvent particle which can be obtained from the first peak of the radial distance function of the solvent (RDF). This distance is the shortest that ensures the motion of particles to be diffusive. We chose this distance for a meaningful result of diffusive behaviours in this study. Even though longer distances than the size of a solvent particle will also work, the shortest one ensures the high efficiency in regards to the calculation. According to the way in which the fixed jump length is chosen and defined, the d would be different for systems with different solvents.

The two time intervals are calculated from trajectories of all solvent particles and the trajectories are obtained by the molecular dynamics simulation. Firstly, the positions of the nanoparticle in each time frame are moved to the origin (0,0,0) and the coordinates of solvent particles are also moved by the same vector with the consideration of the periodic boundary conditions. Secondly, the solvent region around the solute is divided into $\sim$100 spherical shells or bins. The time taken by a solvent particle traveling a jump length initially from a random start is then calculated for each solvent particle in each time frame. The persistence time of each solvent particle is then obtained from the average of all time frames. The followed time interval after the first one taken by a solvent particle traveling a jump length is

also calculated. The exchange time of each solvent particle is then obtained from the average of all time frames. Lastly, the persistence time and exchange time of a bin, which is the persistence time and exchange time at a given radial distance to the origin, are obtained by the average of all solvent particles inside the bin.

The local relations hold based on the equilibrium between the diffusion flux J_{diff} and the frictional flux J_{drift} according to Pronk and coworkers' arguments,[76]

$$J_{drift} \approx -k_B T \mu \frac{n^0 n^1}{\Delta x}, \tag{1.41}$$

$$J_{diff} = n^0 n^1 v, \tag{1.42}$$

where μ is the isotropic hydrodynamic friction at fluid in a select cell, n^0 is the original number of particles, n^1 is the extra number of particles because of an applied potential, Δx is the length of the cell in one dimension and v is the rate of a particle diffusing cross the cell boundary. The rate is proportional to the inverse of t_p and the viscosity is proportional to the inverse of μ. The relation between the viscosity and persistence time is then obtained by balancing the two fluxes,

$$\eta_x \propto k_B T \langle t_p \rangle_x, \tag{1.43}$$

and relation between the diffusion coefficient and exchange time is also obtained,

$$D_x \propto \langle t_x \rangle_x, \tag{1.44}$$

where the subscript x in η_x, D_x, $\langle t_p \rangle_x$, $\langle t_x \rangle_x$ represents the local viscosity, diffusion coefficient, persistence time and exchange time at the position x, respectively. In Chapter 2 and 3, the local viscosity of solvent around nanoparticles is estimated by the persistence time. In Chapter 4, apart from the estimation of local viscosity of solvent near dendrimers by the

persistence time, the local diffusivity of the solvent is also estimated by the exchange time.

1.6 Research objectives

The size measurement of nanoparticles would have been addressed if the Stokes-Einstein relation worked for particles in all sizes. However, it fails for particles in a few nanometers. Note we focus on the large size regime aforementioned. The hydrodynamic radius measured by equipments, such as the analytical ultracentrifugation (AUC) and dynamic light scattering (DLS) based on the SER, overestimates the true size. It makes the size determination of nanoparticles difficult. Several causes of the deviation have been proposed, including the interaction force between the solute particle and surrounding solvent particles, the relative sizes of the solute and solvent particles, hopping motions in heterogeneous liquid and the difference between macroviscosity and nanoviscosity. However, the origin still remains elusive and an effective modification to the SER is absent. In this thesis, we present a new Stokes-Einstein relation, modified by allowing increases in viscosity of surrounding solvent near nanoparticles. The new theory should substitute the traditional Stokes-Einstein relation for a better size determination. We perform molecular dynamics simulation to investigate the hydrodynamics of solutes, a few nanometers in size, in a liquid solvent. The hydrodynamic properties we have studied in this thesis include the diffusion of solute and viscosity of solvent. Systems of dendrimers in Lennard-Jones liquids, bare nanoparticles in Lennard-Jones liquids and ligands grafted gold nanoparticles in water are involved in this thesis to reproduce the deviation behaviours observed in experiments. We detect changes in the local viscosity of solvent and finally test the new theory.

The new theory presented in this thesis is solved from Cauchy's equation,

$$\rho \frac{\mathrm{D}u_i}{\mathrm{D}t} = \frac{\partial \sigma_{ij}}{\partial x_j} + \rho f_i, \tag{1.45}$$

where ρ is the mass density of the fluid, u_i is the corresponding components of the fluid's velocity field, σ_{ij} is the stress tensor, x_j for $j = 1, 2, 3$ are the Cartesian coordinates of a fixed point and f_i is a component of a body force per unit mass. Cauchy's equation is an application of Newton's second law and describes the forces on volume element of the fluid.

The following three chapters fulfill the major objectives of the project. We propose a new Stokes-Einstein relation by solving Cauchy's equation allowing an increase in viscosity of solvent near a diffusing solute; and we detect the assumed increases in the local viscosity by applying the persistence and exchange time method to the investigated solute/solvent systems; and we finally test the new Stokes-Einstein relation by successfully predict the sizes of nanoparticles with different structures.

Bibliography

[1] A. Einstein. *Investigations on the theory of the brownian movement.* Dover publications, inc., 1956.

[2] W. Sutherland. A dynamical theory of diffusion for non-electrolytes and the molecular mass of albumin. *Philos. Mag.*, 9(54):781–785, 1905.

[3] M. A. Islam. Einstein-Smoluchowski diffusion equation : A discussion. *Phys. Scripta*, 70:120–125, 2004.

[4] E. W. Montroll and G. H. Weiss. Random walks on lattices. II. *J. Math. Phys.*, 6(2):167, 1965.

[5] E. W. Montroll. Random walks on lattices. III. Calculation of first-passage times with application to exciton trapping on photosynthetic units. *J. Math. Phys.*, 10(4):753, 1969.

[6] R. Brown. A brief account of microscopical observations made in the months of June, July and August 1827, on the particles contained in the pollen of plants; and on the general existence of active molecules in organic and inorganic bodies. *Philos. Mag.*, 4(21):161–173, 1828.

[7] M. Rubinstein and H. C. Ralph. *Polymer Physics*. Oxford university press, New York, 2003.

[8] G. F. Mazenko. *Nonequilibrium Statistical Mechanics*. Wiley-VCH, 2003.

[9] R. Kubo. The fluctuation-dissipation theorem. *Rep. Prog. Phys.*, 29(1):306, 1966.

[10] J. Weber. Fluctuation dissipation theorem. *Phys. Rev.*, 101(6):1620–1626, 1956.

[11] M. Vergeles, P. Keblinski, J. Koplik, and J. R. Banavar. Stokes drag and lubrication flows: A molecular dynamics study. *Phys. Rev. E*, 53(5):4852–4864, 1996.

[12] D. J. Acheson. *Elementary Fluid Dynamics*. Clarendon press, 1990.

[13] G. K. Batchelor. *An Introduction to Fluid Dynamics*. Cambriage University Press, 2000.

[14] C. E. Tansley and D. P. Marshall. Flow past a cylinder on a β plane, with application to gulf stream separation and the antarctic circumpolar current. *J. Phys. Ocenaogr.*, 31:3274–3283, 2001.

[15] J. R. Schmidt and J. L. Skinner. Hydrodynamic boundary conditions, the Stokes-Einstein law, and long-time tails in the Brownian limit. *J. Chem. Phys.*, 119(15):8062, 2003.

[16] J. R. Schmidt and J. L. Skinner. Brownian motion of a rough sphere and the Stokes-Einstein law. *J. Phys. Chem. B*, 108(21):6767–6771, 2004.

[17] Z. Li. Critical particle size where the Stokes-Einstein relation breaks down. *Phys. Rev. E*, 80(6):061204, 2009.

[18] S. P. Lee, W. Tscharnuter, and B. Chu. Calibration of an optical self-beating spectrometer by polystyrene latex spheres and confirmation of the Stokes-Einstein formula. *J. Polym. Sci. Part B Polym. Phys.*, 10(12):2453–2459, 1972.

[19] M. M. Kops-Werkhoven. Dynamic behavior of silica dispersions studied near the optical matching point. *J. Chem. Phys.*, 77(5):2242, 1982.

[20] S. Sengupta, S. Karmakar, C. Dasgupta, and S. Sastry. Breakdown of the Stokes-Einstein relation in two, three, and four dimensions. *J. Chem. Phys.*, 138(12):12A548, 2013.

[21] J. A. Hodgdon and F. H. Stillinger. Stokes-Einstein violation in glass-forming liquids. *Phys. Rev. E*, 48(1):207–213, 1993.

[22] M. Cappelezzo, C. A. Capellari, S. H. Pezzin, and L. A. F. Coelho. Stokes-Einstein relation for pure simple fluids. *J. Chem. Phys.*, 126(22):224516, 2007.

[23] C. De Michele and D. Leporini. Viscous fow and jump dynamics in molecular supercooled liquids. 1. Translations. *Simulation*, 63(3):13, 1999.

[24] J. Liu, D. Cao, and L. Zhang. Molecular dynamics study on nanoparticle diffusion in polymer melts: A test of the Stokes-Einstein law. *J. Phys. Chem. C*, 112(17):6653–6661, 2008.

[25] V. J. Mohanraj and Y. Chen. Nanoparticles - A Review. *Trop. J. Pharm. Res.*, 5(1):561–573, 2006.

[26] L. Mu and S. S. Feng. A novel controlled release formulation for the anticancer drug paclitaxel (Taxol): PLGA nanoparticles containing vitamin E TPGS. *J. Control. Release*, 86(1):33–48, 2003.

[27] A. Vila, A. Sánchez, M. Tobío, P. Calvo, and M. J. Alonso. Design of biodegradable particles for protein delivery. *J. Control. Release*, 78(1-3):15–24, 2002.

[28] S. Zeng, K. Yong, I. Roy, X. Dinh, X. Yu, and F. Luan. A review on functionalized gold nanoparticles for biosensing applications. *Plasmonics*, 6(3):491–506, 2011.

[29] T. Gregory Schaaff, G. Knight, M. N. Shafigullin, R. F. Borkman, and R. L. Whetten. Isolation and selected properties of a 10.4 kDa gold: glutathione cluster compound. *J. Phys. Chem. B*, 102(52):10645–10646, 1998.

[30] A. Mohanty, N. Garg, and R. Jin. A universal approach to the synthesis of noble metal nanodendrites and their catalytic properties. *Angew. Chem. Int. Ed.*, 49(29):4962–4966, 2010.

[31] M. H. Magnusson, K. Deppert, J. Malm, J. Bovin, and L. Samuelson. Gold nanoparticles: Production, reshaping, and thermal charging. *J. Nanopart. Res*, 1:243–251, 1999.

[32] Y. Jv, B. Li, and R. Cao. Positively-charged gold nanoparticles as peroxidase mimic and their application in hydrogen peroxide and glucose detection. *Chem. Commun.*, 46(42):8017–8019, 2010.

[33] A. W. Bosman, H. M. Janssen, and E. W. Meijer. About dendrimers: Structure, physical properties, and applications. *Chem. Rev.*, 99(7):1665–1688, 1999.

[34] C. C. Lee, J. A. MacKay, J. M. J. Fréchet, and F. C. Szoka. Designing dendrimers for biological applications. *Nature Biotechnol.*, 23(12):1517–1526, 2005.

[35] R. Esfand and D. A. Tomalia. Poly(amidoamine) (PAMAM) dendrimers: From biomimicry to drug delivery and biomedical applications. *Drug Discov. Today*, 6(8):427–436, 2001.

[36] K. Sadler and J. P. Tam. Peptide dendrimers: Applications and synthesis. *Rev. Mol. Biotechnol.*, 90(3-4):195–229, 2002.

[37] V. I. Klimov, A. A. Mikhailovsky, S. Xu, A. A. Malko, J. A. Hollingsworth, C. A. Leatherdale, H. J. Eisler, and M. G. Bawendi. Optical gain and stimulated emission in nanocrystal quantum dots. *Science*, 290(5490):314–317, 2000.

[38] X. Gao, Y. Cui, R. M. Levenson, L. W. K. Chung, and S. Nie. In vivo cancer targeting and imaging with semiconductor quantum dots. *Nature Biotechnol.*, 22(8):969–976, 2004.

[39] X. Michalet, F. F. Pinauad, L. A. Bentolila, J. M. Tsay, J. J. Li, G. Sundaresan, A. M. Wu, S. S. Gambhir, and S. Weiss. Quantum dots for live cells, in vivo imaging, and diagnostics. *Science*, 307:538–545, 2005.

[40] D. R. Larson, W. R. Zipfel, R. M. Williams, S. W. Clark, M. P. Bruchez, F. W. Wise, and W. W. Webb. Water-soluble quantum dots for multiphoton fluorescence imaging in vivo. *Science*, 300(2003):1434–1436, 2003.

[41] P. C. Ray. Size and shape dependent second order nonlinear optical properties of nanomaterials and their application in biological and chemical sensing. *Chem. Rev.*, 110(9):5332–5365, 2010.

[42] R. P. Carney, J. Y. Kim, H. Qian, R. Jin, H. Mehenni, F. Stellacci, and O. M. Bakr. Determination of nanoparticle size distribution together with density or molecular weight by 2D analytical ultracentrifugation. *Nat. Commun.*, 2:335, 2011.

[43] G. L. Lukacs, P. Haggie, D. Lechardeur, N. Freedman, S. Verkman, and A. S. Verkman. Cell biology and metabolism: Size-dependent DNA mobility in cytoplasm. *J. Biol. Chem*, 275(3):1–6, 2000.

[44] D. Chowdhury, A. Schadschneider, and K. Nishinari. Physics of transport and traffic phenomena in biology: From molecular motors and cells to organisms. *Phys. Life Rev.*, 2(4):318–352, 2005.

[45] J. B. Falabella, T. J. Cho, D. C. Ripple, V. A. Hackley, and M. J. Tarlov. Characterization of gold nanoparticles modified with single-stranded DNA using analytical ultracentrifugation and dynamic light scattering. *Langmuir*, 26(15):12740–12747, 2010.

[46] A. Bootz, V. Vogel, D. Schubert, and J. Kreuter. Comparison of scanning electron microscopy, dynamic light scattering and analytical ultracentrifugation for the sizing of poly(butyl cyanoacrylate) nanoparticles. *Eur. J. Pharm. Biopharm.*, 57(2):369–375, 2004.

[47] H. Xia, K. Ishii, and T. Iwai. Hydrodynamic radius sizing of nanoparticles in dense polydisperse media by low-coherence dynamic light scattering. *Jpn. J. Appl. Phys.*, 44(8):6261–6264, 2005.

[48] R. Pecora. Dynamic light scattering measurement of nanometer particles in liquids. *J. Nanopart. Res*, 2:123–131, 2000.

[49] D. P. Chowdhury, C. M. Sorensen, T. W. Taylor, J. F. Merklin, and T. W. Lester. Application of photon correlation spectroscopy to flowing Brownian motion systems. *Appl. Opt.*, 23(22):4149, 1984.

[50] E. Gulari, E. Gulari, Y. Tsunashima, and B. Chu. Photon correlation spectroscopy of particle distributions. *J. Chem. Phys.*, 70(8):3965, 1979.

[51] D. Fioretto, L. Comez, M. E. Gallina, A. Morresi, L. Palmieri, M. Paolantoni, P. Sassi, and F. Scarponi. Separate dynamics of solute and solvent in water-glucose solutions by depolarized light scattering. *Chem. Phys. Lett.*, 441(4-6):232–236, 2007.

[52] A. K. Rizos and K. L. Ngai. Solvent rotational mobility in 1,2-polybutadiene/aroclor solutions by dielectric relaxation and Fabry-Perot interferometry. *Macromolecules*, 27(24):7076–7078, 1994.

[53] W. Steffen, A. Patkowski, H. Glaser, G. Meier, and E. W. Fischer. Depolarized-light-scattering study of orthoterphenyl and comparison with the mode-coupling model. *Phys. Rev. E*, 49(4):2992–3002, 1994.

[54] R. Pecora. *Dynamic light scattering: Applications of photon correlation spectroscopy.* Plenum Press, New York and London, 1985.

[55] A. Bennett. *Screening Lengths of Polymers in Solution.* 2003.

[56] W.I. I. Goldburg. Dynamic light scattering. *Am. J. Phys.*, 67(12):1152–1160, 1999.

[57] B. Demeler, T. L. Nguyen, G. E. Gorbet, V. Schirf, E. H. Brookes, P. Mulvaney, A. O. El-Ballouli, J. Pan, O. M. Bakr, A. K. Demeler, B. I. Hernandez Uribe, N. Bhattarai, and R. L. Whetten. Characterization of size, anisotropy, and density heterogeneity of nanoparticles by sedimentation velocity. *Anal. Chem.*, 86(15):7688–7695, 2014.

[58] J. Lebowitz, M. S. Lewis, and P. Schuck. Modern analytical ultracentrifugation in protein science: A tutorial review. *Protein Sci.*, 11(9):2067–2079, 2002.

[59] P. H. Brown and P. Schuck. Macromolecular size-and-shape distributions by sedimentation velocity analytical ultracentrifugation. *Biophys. J.*, 90(12):4651–4661, 2006.

[60] B. Hong, A. Chremos, and A. Z. Panagiotopoulos. Simulations of the structure and dynamics of nanoparticle-based ionic liquids. *Farad. Discuss*, 154:29, 2012.

[61] O. Ueberschär, C. Wagner, T. Stangner, C. Gutsche, and F. Kremer. The effective hydrodynamic radius of single DNA-grafted colloids as measured by fast Brownian motion analysis. *Polymer*, 52(8):1829–1836, 2011.

[62] R. A. Sperling, T. Liedl, S. Duhr, S. Kudera, M. Zanella, C. A J Lin, W. H. Chang, D. Braun, and W. J. Parak. Size determination of (bio)conjugated water-soluble colloidal nanoparticles: A comparison of different techniques. *J. Phys. Chem. C*, 111(31):11552–11559, 2007.

[63] A. H. R. Koch, G. Lévêque, S. Harms, K. Jaskiewicz, M. Bernhardt, A. Henkel, C. Sönnichsen, K. Landfester, and G. Fytas. Surface asymmetry of coated spherical nanoparticles. *Nano Lett.*, 14(7):4138–4144, 2014.

[64] Ludwig Reimer. *Transmission electron microscopy: Physics of image formation and microanalysis*. Springer-Verlag Berlin Heidelberg, 1984.

[65] A. Tuteja, M. E. Mackay, S. Narayanan, S. Asokan, and M. S. Wong. Breakdown of the continuum Stokes-Einstein relation for nanoparticle diffusion. *Nano Lett.*, 7(5):1276–81, 2007.

[66] R. Walser, A. E. Mark, and W. F. V. Gunsteren. On the validity of Stokes' law at the molecular level. *Chem. Phys. Lett.*, 303:583–586, 1999.

[67] E. Heikkilä, A. A. Gurtovenko, H. Martinez-Seara, H. Häkkinen, I. Vattulainen, and J. Akola. Atomistic simulations of functional Au_{144} $(SR)_{60}$ gold nanoparticles in aqueous environment. *J. Phys. Chem. C*, 116(17):9805–9815, 2012.

[68] S. A. Egorov. Anomalous nanoparticle diffusion in polymer solutions and melts: A mode-coupling theory study. *J. Chem. Phys.*, 134(8):084903, 2011.

[69] J. Kim and T. Keyes. On the breakdown of the Stokes-Einstein law in supercooled liquids. *J. Phys. Chem.*, 109(45):21445–8, 2005.

[70] R. Zangi and L. Kaufman. Frequency-dependent Stokes-Einstein relation in supercooled liquids. *Phys.l Rev. E*, 75(5):051501, 2007.

[71] G. C. Sosso, J. Behler, and M. Bernasconi. Breakdown of Stokes-Einstein relation in the supercooled liquid state of phase change materials. *Phys. Status Solidi (B)*, 249(10):1880–1885, 2012.

[72] F. Puosi and D. Leporini. Communication: Fast and local predictors of the violation of the Stokes-Einstein law in polymers and supercooled liquids. *J. Chem. Phys.*, 136(21):211101, 2012.

[73] S. K. Kumar, G. Szamel, and J. F. Douglas. Nature of the breakdown in the Stokes-Einstein relationship in a hard sphere fluid. *J. Chem. Phys.*, 124(21):214501, 2006.

[74] P. K. Maiti and B. Bagchi. Diffusion of flexible, charged, nanoscopic molecules in solution: Size and pH dependence for PAMAM dendrimer. *J. Chem. Phys.*, 131(21):214901, 2009.

[75] B. Halle and M. Davidovic. Biomolecular hydration: From water dynamics to hydrodynamics. *Proc. Natl. Acad. Sci. U.S.A.*, 100(21):12135–12140, 2003.

[76] S. Pronk, E. Lindahl, and P. M. Kasson. Dynamic heterogeneity controls diffusion and viscosity near biological interfaces. *Nat. Commun.*, 5:3034, 2014.

[77] E. E. Lees, M. J. Gunzburg, T. L. Nguyen, G. J. Howlett, J. Rothacker, E. C. Nice, A. H. A. Clayton, and P. Mulvaney. Experimental determination of quantum dot size distributions, ligand packing densities, and bioconjugation using analytical ultracentrifugation. *Nano Lett.*, 8(9):2883–2890, 2008.

[78] M. E. Mackay, A. Tuteja, P. M. Duxbury, C. J. Hawker, B. Van Horn, Z. Guan, G. Chen, and R. S. Krishnan. General strategies for nanoparticle dispersion. *Science (New York, N.Y.)*, 311(5768):1740–1743, 2006.

[79] X. Xie, Q. Liu, R. K. Li, X. Zhou, Q. Zhang, Z. Yu, and Y. Mai. Rheological and mechanical properties of PVC/CaCO3 nanocomposites prepared by in situ polymerization. *Polymer*, 45(19):6665–6673, 2004.

[80] V. V. Ginzburg. Polymer-grafted nanoparticles in polymer melts: Modeling using the combined SCFT–DFT approach. *Macromolecules*, 46(24):9798–9805, 2013.

[81] A. Jayaraman and K. S. Schweizer. Effective interactions, structure, and phase behavior of lightly tethered nanoparticles in polymer melts. *Macromolecules*, 41(23):9430–9438, 2008.

[82] C. Pastorino, K. Binder, T. Kreer, and M. Müller. Static and dynamic properties of the interface between a polymer brush and a melt of identical chains. *J. Chem. Phys.*, 124(6):64902, 2006.

[83] R. A. Omari, A. M. Aneese, C. A. Grabowski, and A. Mukhopadhyay. Diffusion of nanoparticles in semidilute and entangled polymer solutions. *J. Phys. Chem. B*, 113(25):8449–8452, 2009.

[84] C. A. Grabowski, B. Adhikary, and A. Mukhopadhyay. Dynamics of gold nanoparticles in a polymer melt. *Appl. Phys. Lett.*, 94(2):18–21, 2009.

[85] R. K. Murarka, S. Bhattacharyya, and B. Bagchi. Diffusion of small light particles in a solvent of large massive molecules. *J. Chem. Phys.*, 117(23):10730, 2002.

[86] G. L. Pollack, R. P. Kennan, J. F. Himm, and D. R. Stump. Diffusion of xenon in liquid alkanes: Temperature dependence measurements with a new method. Stokes–Einstein and hard sphere theories. *J. Chem. Phys.*, 92(1):625, 1990.

[87] B. A. Kowert, K. T. Sobush, N. C. Dang, L. G. Seele, C. F. Fuqua, and C. L. Mapes. Diffusion of dioxygen in 1-alkenes and biphenyl in perfluoro-n-alkanes. *Chem. Phys. Lett.*, 353(1-2):95–99, 2002.

[88] F. Ould-Kaddour and J. Barrat. Molecular-dynamics investigation of tracer diffusion in a simple liquid. *Phys. Rev. A*, 45(4):2308–2314, 1992.

[89] A. J. Easteal and L. A. Woolf. Tracer diffusion in hard-sphere liquids from molecular dynamics simulations. *Chem. Phys. Lett.*, 167(4):329–333, 1990.

[90] F. Ould-Kaddour and D. Levesque. Molecular-dynamics investigation of tracer diffusion in a simple liquid: Test of the Stokes-Einstein law. *Phys. Rev. E- Stat. Nonlin. Soft Matter Phys.*, 63(1 II):1–9, 2001.

[91] S. Bhattacharyya and B. Bagchi. Anisotropic local stress and particle hopping in a deeply supercooled liquid. *Phys. Rev .Lett.*, 89(2):25504, 2002.

[92] B. Doliwa and A. Heuer. Hopping in a supercooled Lennard-Jones liquid: Metabasins, waiting time distribution, and diffusion. *Phys. Rev. E*, 67(3):030501, 2003.

[93] T. D. Li, J. Gao, R. Szoszkiewicz, U. Landman, and E. Riedo. Structured and viscous water in subnanometer gaps. *Phys. Rev. B-Condens. Matter Mater. Phys.*, 75(11):1–6, 2007.

[94] M. P. Goertz, J. E. Houston, and X. Zhu. Hydrophilicity and the viscosity of interfacial water. *Langmuir*, 23(10):5491–5497, 2007.

[95] S. H. Khan, G. Matei, S. Patil, and P. M. Hoffmann. Dynamic solidification in nanoconfined water films. *Phys. Rev. Lett.*, 105(10):106101, 2010.

[96] D. Ortiz-Young, H. Chiu, S. Kim, K. Voïtchovsky, and E. Riedo. The interplay between apparent viscosity and wettability in nanoconfined water. *Nat. Commun.*, 4:2482, 2013.

[97] H. Hoang and G. Galliero. Local viscosity of a fluid confined in a narrow pore. *Phys. Rev. E- Stat. Nonlin. Soft Matter*, 86(2):1–10, 2012.

[98] S. K. Pal, J. Peon, B. Bagchi, and A. H. Zewail. Biological water: Femtosecond dynamics of macromolecular hydration. *J. Phys. Chem. B*, 106(48):12376–12395, 2002.

[99] R. M. Venable and R. W. Pastor. Frictional models for stochastic simulations of proteins. *Biopolymers*, 27(6):1001–1014, 1988.

[100] D. Brune and S. Kim. Predicting protein diffusion coefficients. *Proc. Natl. Acad. Sci. U.S.A.*, 90(9):3835–3839, 1993.

[101] V. V. Krishnan and M. Cosman. An empirical relationship between rotational correlation time and solvent accessible surface area. *J. Biomol. NMR.*, 12:177–182, 1998.

[102] J. García De La Torre. Hydration from hydrodynamics. General considerations and applications of bead modelling to globular proteins. *Biophys. Chem.*, 93(2-3):159–170, 2001.

[103] A. Cheng and K. M. Merz. Application of the Nosé-Hoover chain algorithm to the study of protein dynamics. *J. Phys. Chem.*, 100(5):1927–1937, 1996.

[104] S. E. Feller, Y. Zhang, R. W. Pastor, and B. R. Brooks. Constant pressure molecular dynamics simulation: The Langevin piston method. *J. Chem. Phys.*, 103(11):4613, 1995.

[105] G. J. Martyna, D. J. Tobias, and M. L. Klein. Constant pressure molecular dynamics algorithms. *J. Chem. Phys.*, 101:4177, 1994.

[106] A. J. Rzepiela, M. Louhivuori, C. Peter, and S. J. Marrink. Hybrid simulations: Combining atomistic and coarse-grained force fields using virtual sites. *Phys. Chem. Chem. Phys.*, 13(22):10437–10448, 2011.

[107] C. Clementi. Coarse-grained models of protein folding: toy models or predictive tools? *Curr. Opin. Struct. Biol.*, 18(1):10–15, 2008.

[108] A. D. MacKerell, D. Bashford, M Bellott, R. L. Dunbrack, J. D. Evanseck, M. J. Field, S. Fischer, J. Gao, H. Guo, S. Ha, and et. al. All-atom empirical potential for molecular modeling and dynamics studies of proteins. *J. Phys. Chem. B*, 102(18):3586–616, 1998.

[109] D. Dubbeldam, S. Calero, T. J. H. Vlugt, R. Krishna, T. L. M. Maesen, and B. Smit. United atom force field for alkanes in nanoporous materials. *J. Phys. Chem. B*, 108(33):12301–12313, 2004.

[110] B. R. Brooks, R. E. Bruccoleri, B. D. Olafson, D. J. States, S. Swaminathan, and M. Karplus. CHARMM: A program for macromolecular energy, minimization, and dynamics calculations. *J. Comput. Chem*, 4(2):187–217, 1983.

[111] W. D. Cornell, P. Cieplak, C. I. Bayly, I. R. Gould, K. M. Merz, D. M. Ferguson, D. C. Spellmeyer, T. Fox, J. W. Caldwell, and P. A. Kollman. A second generation force field for the simulation of proteins, nucleic acids, and organic molecules. *J. Am. Chem. Soc.*, 117(19):5179–5197, 1995.

[112] W. L. Jorgensen, D. S. Maxwell, and J. Tirado-Rives. Development and testing of the OLPS all-atom force field on conformational energetics and properties of organic liquids. *J. Am. Chem. Soc.*, 118(15):11225–11236, 1996.

[113] B. Chen and J. I. Siepmann. Transferable potentials for phase equilibria. 3. Explicit-hydrogen description of normal alkanes. *J. Phys. Chem. B*, 103(25):5370–5379, 1999.

[114] V. A. Harmandaris, N. P. Adhikari, N. F. A. Van Der Vegt, and K. Kremer. Hierarchical modeling of polystyrene: From atomistic to coarse-grained simulations. *Macromolecules*, 39(19):6708–6719, 2006.

[115] T. A. Wassenaar, K. Pluhackova, R. A. Böckmann, S. J. Marrink, and D. P. Tieleman. Going backward: A flexible geometric approach to reverse transformation from coarse grained to atomistic models. *J. Chem. Theory Comput.*, 10(2):676–690, 2014.

[116] S. Viscardy, J. Servantie, and P. Gaspard. Transport and Helfand moments in the Lennard-Jones fluid. I. Shear viscosity. *J. Chem. Phys.*, 126(18), 2007.

Chapter 2

The hydrodynamic drag on diffusing nanoparticles for size determination

2.1 Abstract

Size estimates of proteins and nanoparticles obtained from measured diffusivities using the Stokes-Einstein relation are typically twice the true size. We report here a new drag law obtained by allowing for the increase in shear viscosity near the surface of the particle, and solving the Navier-Stokes equations for viscous flow to leading order in this increase. This improvement in the description of the drag force permits accurate size measurements for particles with radii of a few nanometres. We discuss literature data on the hydrodynamic radii of CdSe quantum dots of known size, simulations of both nanoparticles and dendritic structures, and literature data on protein simulations. The experimental data agree well with the drag law that allows for a viscosity increase near the surface. We use the persistence time method to examine local changes in viscosity and so find independent confirmation of the expected increase in viscosity near the surfaces of simulated diffusing particles. Typical increases in shear viscosity near the surfaces of the diffusing particles are between 50 and 150% of its bulk value.

2.2 Introduction

Fundamental to the determination of particle radii from dynamic light scattering (DLS) or sedimentation velocity analytical ultracentrifugation (SV-AUC) is the assumption that the Stokes-Einstein relation (SER) is valid down to nanoscale.[1–4] Deviations from Stokes' law on the molecular level have been detected by numerical[5–10] and experimental[7, 9–12] studies. Halle showed that the diffusion coefficients of globular proteins are half that expected from the SER, so that a hydrodynamic radius inferred by the SER from diffusion observations is twice the true radius.[13] Halle suggested that the discrepancy comes from an increase in the viscosity of water in the first solvation shell around the proteins. The viscosity of water confined between surfaces was later found to be larger than that in bulk water.[14–18] Characterization of any increase in viscosity in the solvent near a diffusing particle and measurements of the hydrodynamic size of particles with known true sizes could improve the description of drag forces on nanosized objects and therefore allow for more accurate measurements of their sizes. We here explore this possibility by solving the Navier-Stokes equations for Stokes flow to leading order in the increase in viscosity near a particle surface, by using Molecular Dynamics (MD) simulations to confirm the viscosity increase and by comparing the predictions to measurements of the hydrodynamic size of CdSe quantum dots. Our solution of the Navier-Stokes equations replaces Stokes' law for the drag on a sphere with stick boundary conditions[19] and so leads to a new relationship between diffusion coefficient and size.

Ortiz-Young *et al.*[18] investigated the change in viscosity of water confined between an Atomic Force Microscope (AFM) tip and surfaces of varying hydrophilicity. They argued that the viscosity increase due to confinement between the tip and surface is a function of the gap between the surface and tip, but that a slip length should be included in this gap.

It is the variation in slip length that captures the variation in viscosity between surfaces. Couette flow near a flat solid surface exhibits layered structures indicated by the density peaks near the surface,[20, 21] and a nanostructured surface could induce the organization of water.[22]

Stokes' law for a diffusing nanoparticle in a polymer matrix can break down if the nanoparticle is smaller than the gyration radius (R_g) of the free polymers in the matrix.[11, 23, 24] Conversely, when the nanoparticle is larger than the R_g, Stokes' law works well, and macroscopic effects dominate the diffusion.[23, 24] We are interested here in the breakdown of Stokes' law when the diffusing particle is larger than the solvent particles. We expect to find that the extent of the deviation from Stokes' law varies between solvents.

The dynamics of the solvent in the vicinity of a nanoparticle could be the origin of a deviation from Stokes' law for the drag on the nanoparticle and so of the large hydrodynamic sizes inferred from the SER. The presence of a large particle might well constrain the motions of particles nearby. Following an analogy with the failure of Stokes' law for bulk, supercooled liquids, which has been attributed to dynamical heterogeneity,[7, 25–27] the local structures of solvents near surfaces have been studied.[28–30] Slowed dynamics of polymer melts near nanoparticles' surfaces were reported.[31] A positive correlation between the local density of a fluid and its local viscosity has been reported.[32, 33] Irregular particle surfaces also change the local dynamics of a fluid, as is shown by increased viscosity of water near proteins.[13, 30] An increase in fluid viscosity leads to a larger stress exerted on the nanoparticles.[34] Taken together, these studies support the view that the viscosity can be higher in the neighbourhood of a diffusing particle. The viscosity increase in turn affects the drag force on the particle, and so affects its diffusion. A viscosity increase leads to higher drag, slower diffusion, and a larger hydrodynamic radius, if that radius is calculated using the unmodified SER.

That hydrodynamic sizes are larger than structural sizes indicates that their diffusion is slower than that predicted by Stokes' law and raises the possibility that by some modification of Stokes' law for drag on the particle we might improve calibration of size measurements for particles in the nanometre size range.

The hypothesis that increased viscosity near the surface of a diffusing particle affects the drag on the particle may be partly tested by calculating this drag force, predicting the sizes that should be seen and comparing these to SV-AUC measurements. The ideal particles for this test are CdSe nanoparticles, which are monodisperse, with known true sizes. Such a test is useful but not complete, because a model based on viscosity increase might well fit increases caused by some other influence. We seek a picture of drag forces that is as widely applicable as possible, and it is not safe to assume that only a single mechanism operates. We therefore simulated particles, both nanoparticles and dendrimers, with hydrodynamic size behaviour similar to that of the CdSe particles. For the simulated particles, we can directly examine the dynamics of nearby solvent, and detect any increased viscosity.[30]

We first derive the effect of increased surface viscosity on drag, then describe methods of calculation of the diffusion coefficients, viscosities, particle structures, and changes to the solvent near the particles. We then discuss our molecular dynamics simulations, and some previously published simulations to which we compare our simulations. We compare hydrodynamic sizes obtained from the traditional SER for the real and simulated particles, report apparent changes in viscosity near these particles, and directly investigate the changes in the solvent near the diffusing particles. We discuss these results with a view to establishing an improved size determination method especially useful for particles with sizes up to 10 nm.

2.3 Theory

2.3.1 The effect of surface viscosity on drag

We follow the derivation of Stokes' law for the drag on a sphere moving uniformly through a viscous, incompressible fluid, and introduce a variable viscosity. Cauchy's equation arises from the application of Newton's second law to a volume element of the fluid,

$$\rho \frac{\mathrm{D}u_i}{\mathrm{D}t} = \frac{\partial \sigma_{ij}}{\partial x_j} + \rho f_i, \tag{2.1}$$

where the Einstein summation convention is used, the indices denote elements of Cartesian tensors, σ_{ij} is the stress tensor, f_i is a component of a body force per unit mass, ρ is the mass density of the fluid, x_j for $j = 1, 2, 3$ are the Cartesian coordinates of a fixed point, $\mathbf{r}$, in the flow, the fluid's velocity field, $\mathbf{u}(\mathbf{r})$ has corresponding components u_i, and the time derivative is defined to 'follow the fluid',[19]

$$\frac{\mathrm{D}}{\mathrm{D}t} = \frac{\partial}{\partial t} + u_i \frac{\partial}{\partial x_i}. \tag{2.2}$$

The stress tensor for an incompressible fluid may be written as,

$$\sigma_{ij} = -p\delta_{ij} + \eta(\mathbf{r}) \left(\frac{\partial u_i}{\partial x_j} + \frac{\partial u_j}{\partial x_i} \right), \tag{2.3}$$

where p is the pressure and δ_{ij} is the Kronecker delta. Note that we have explicitly allowed the shear viscosity, η, a dependence on position $\mathbf{r}$. This is the essential difference between the calculation presented here and the standard Stokes calculation.[19]

We assume that the shear viscosity may be written $\eta = \eta_0 + \delta\eta(\mathbf{r})$, where η_0 is the bulk viscosity, $\delta\eta(\mathbf{r})$ is a change in the viscosity near a diffusing particle, and $\mathbf{r}$ is a position

vector. We write the velocity field $\mathbf{u}(\mathbf{r}) = \mathbf{u}_0(\mathbf{r}) + \delta\mathbf{u}(\mathbf{r})$, and the pressure $p(r) = p_0 + \delta p(\mathrm{r})$, where again the subscript '0' denotes the Stokes solution obtained for $\delta\eta = 0$. Substituting the stress tensor (eq 2.3) into Cauchy's equation (eq 2.1), we find,

$$\rho\frac{\mathrm{D}u_i}{\mathrm{D}t} = -\partial_i p + \eta\left(\partial_j\partial_j u_i\right) + \left(\partial_j\eta\right)\left(\partial_j u_i + \partial_i u_j\right) + \rho f_i, \tag{2.4}$$

where we have used the assumption of incompressibility and abbreviated the notation so that the partial derivative with respect to x_i is written ∂_i. Following Stokes and Acheson we neglect the second term in the time derivative,[19] eq 2.2, because we expect viscous forces to dominate, and neglect its first term because we seek a steady state.

In the absence of any variation of the viscosity, we obtain the equation whose solution is the usual Stokes flow,

$$0 = -\partial_i p_0 + \eta_0\left(\partial_j\partial_j u_{0i}\right) + \rho f_i. \tag{2.5}$$

We treat $\delta\eta(\mathbf{r})$, $\delta\mathbf{u}$, and δp as small perturbations, and neglect any product or square or higher power of any of these three. That approach gives the leading correction to the velocity field $\delta\mathbf{u}_0$ due to a viscosity change $\delta\eta$. Rearranging the Navier-Stokes equations under this approximation gives,

$$0 = -\partial_i\delta p + \eta_0\left(\partial_j\partial_j\delta u_i\right) + \left[\delta\eta\left(\partial_j\partial_j u_{0i}\right) + \left(\partial_j\delta\eta\right)\left(\partial_j u_{0i} + \partial_i u_{0j}\right)\right] \tag{2.6}$$

Note that the fields carrying a subscript '0' are themselves the solution of the Navier-Stokes equations with $\delta\eta$, and so terms containing no perturbations disappear. In effect we subtract eq 2.5 from eq 2.4.

Eq 2.6 is of the same form as eq 2.5, with the body force ρf_i replaced by the term in

the square brackets, which contains all contributions from the change in viscosity, and depends on the unperturbed velocity field, $\mathbf{u}_0$, but not on the velocity perturbation, $\delta\mathbf{u}$. This comparison shows that the perturbation to the velocity field, $\delta\mathbf{u}$, is exactly that which would be obtained by adding the terms in square brackets to the body force term, ρf_i. We therefore define an effective perturbation to the body force, whose effects on the flow are identical to the leading order effect of the spatially varying viscosity perturbation,

$$\rho\,\delta f_i = \left[\delta\eta\left(\partial_j\partial_j u_{0i}\right) + \left(\partial_j\delta\eta\right)\left(\partial_j u_{0i} + \partial_i u_{0j}\right)\right]. \tag{2.7}$$

Consider the Stokes flow past a spherical particle of radius a, with stick boundary conditions, and carrying a local increase in shear viscosity near its surface, as shown in Figure 2.1. Both the unperturbed flow and the effective force perturbation, δf_i, are shown. To find the force on the particle due to the viscosity change, we need not solve for the perturbed velocity and pressure fields, but rather add up the total perturbation force on the fluid, to which the force on the particle must be equal and opposite, according to Newton. The change in the drag force on the particle is therefore,

$$\delta F = -2\pi\rho \int_0^\infty \mathrm{d}r \int_0^\pi \mathrm{d}\theta\, r^2 \sin\theta\, \delta\mathbf{f}(r,\theta) \tag{2.8}$$

$$= -2\pi \int_0^\infty \mathrm{d}r \int_0^\pi \mathrm{d}\theta r^2 \sin\theta \left[\delta\eta(r)\nabla^2\mathbf{u}_0 + \left(\nabla\delta\eta(r)\right)\left(\nabla\mathbf{u}_0 + (\nabla\mathbf{u}_0)^T\right)\right] \tag{2.9}$$

The evaluation of this integral is straightforward using the standard solution for $\mathbf{u}_0$ in terms of a stream function.[19]

We have considered only viscosity perturbations that decay monotonically from the surface of the particle at $r = a$ as shown in Figure 2.1. We find that the change in the drag

force is proportional to the change in viscosity at the surface, $\delta\eta(a)$, but independent of the distance over which $\delta\eta$ decays, or the form of this decay. This finding makes sense if we consider the balance of forces on fluid and particle.

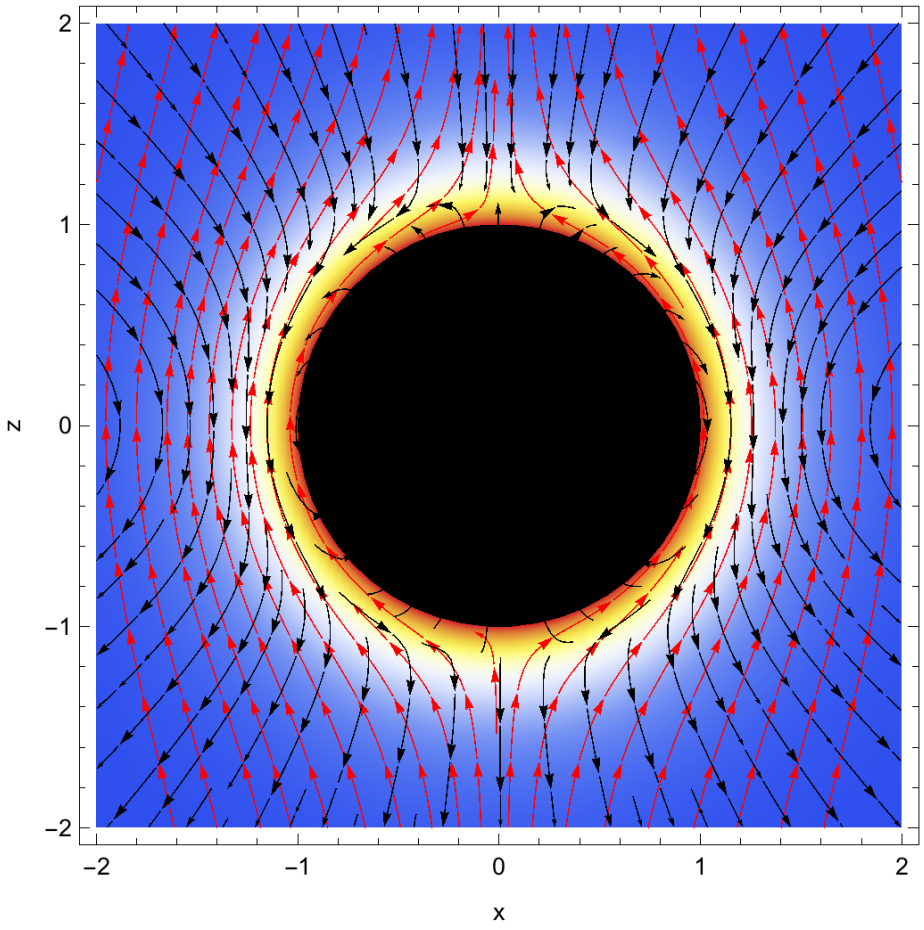

Figure 2.1: A particle of radius $a = 1$ with an increased viscosity at its surface, decaying as a Gaussian into the fluid. The viscosity is indicated by colour, with blue denoting the bulk viscosity. The Stokes flow obtained without the viscosity increase is shown as a vector field in red, and the effective force, eq 2.7 for $\delta\mathbf{f}$, is shown as a vector field in black.

The drag law that we find for flow past a particle of radius a with a local increase in shear

viscosity near its surface is,

$$\mathbf{F} = -6\pi\eta_0 a\mathbf{v} - 4\pi\delta\eta(a)a\mathbf{v}. \tag{2.10}$$

The second term in eq 2.10 is the only term in the tangential part of the force on the particle that does not depend on the thickness of the layer of increased viscosity. The other terms are exactly cancelled by the radial forces.

For a particle suspended in a liquid, the drag coefficient, ζ, is defined so that the drag force on the particle is $\mathbf{F} = -\zeta\mathbf{v}$, where $\mathbf{v}$ is the particle's velocity. If we consider the particle to be a sphere of radius a, Stokes' law relates the drag coefficient of a particle to the radius,

$$\zeta_0 = n\pi\eta a, \tag{2.11}$$

where $n = 4$ for slip boundary conditions and $n = 6$ for stick boundary conditions, and η is the viscosity of the pure liquid. We write the dimensionless increase in viscosity as $\Delta = \delta\eta(a)/\eta_0$, then using eq 2.10 we find,

$$\delta\zeta = 4\pi\eta_0\Delta a. \tag{2.12}$$

2.3.2 Calculation of structural and hydrodynamic radii

Real particles of interest are not simple spheres, and one may define their radii in a variety of ways. These ways are either structural or hydrodynamic. Examples of structural radii include van der Waals radii of nanoparticles, or of the cores of nanoparticles, the gyration radii R_g of dendrimers and polymers. These structural radii are functions of the positions of the atoms in the particle, and likely involve a canonical average over any fluctuations in

the particle's structure. Radii of gyration R_g is calculated by

$$R_g^2 = \frac{1}{N}\sum_{i=1}^{N}(\mathbf{R}_i - \mathbf{R}_{cm})^2, \tag{2.13}$$

with,

$$\mathbf{R}_{cm} = \frac{1}{N}\sum_{i=1}^{N}\mathbf{R}_i, \tag{2.14}$$

where i is the number of monomers of the dendrimers or composite NPs, N is the total number of monomers, $\mathbf{R}_i$ is the position vectors of the ith monomer and $\mathbf{R}_{cm}$ is the center of mass (COM).

A hydrodynamic definition of a particle's radius is available from the Stoke's law. The Stokes-Einstein relation (SER) between diffusion coefficient and particle size is,

$$D = \frac{kT}{6\pi\eta a}, \tag{2.15}$$

where k is the Boltzmann constant, T is the absolute temperature, and D is the translational diffusion coefficient of the particle. Eq 2.11 applies strictly only to spherical particles, and so too does eq 2.15. A hydrodynamic radius is defined by relaxing this requirement, and solving eq 2.15 for the radius,

$$r_h = \frac{kT}{n\pi\eta D}. \tag{2.16}$$

As discussed above, in the case of a globular protein this radius is typically double the true, structural radius.[13]

We may rewrite the SER with the drag law in eq 2.10. The diffusion coefficient becomes,

$$D = \frac{kT}{(6\pi\eta_0 + 4\pi\eta_0\Delta)\, a}. \tag{2.17}$$

It remains to consider the dependence of the viscosity change on the size of the particle. We expect that if our diffusing particle is no larger than the surrounding solvent, $\Delta = 0$. If Δ is constant at larger particle sizes, we would see an increasing deviation between the hydrodynamic and structural radii, and this has not been reported to the best of our knowledge, so we conclude that Δ must decay at least as fast as a^{-1}. Writing the radius of a solvent particle as s, the simplest expression for Δ that meets these requirements is,

$$\Delta = 4\alpha\frac{s}{a}\left(1 - \frac{s}{a}\right), \tag{2.18}$$

where α is the maximum value of Δ. Substituting this expression into eq 2.17 gives,

$$D = \frac{kT}{6\pi\eta_0 a\left(1 + \frac{8\alpha s}{3a}\left(1 - \frac{s}{a}\right)\right)}, \tag{2.19}$$

which may be solved to obtain,

$$\hat{r}_{\mathrm{h}} = \left(\frac{kT}{12\pi D\eta_0} - \frac{4\alpha s}{3}\right) + \sqrt{\frac{8}{3}\alpha s^2 + \left(\frac{kT}{12\pi D\eta_0} - \frac{4\alpha s}{3}\right)^2}. \tag{2.20}$$

Note that in the above a is the radius of an idealised spherical particle, where $\hat{r}_{\mathrm{h}}$ is a measured radius defined for a particle of arbitrary shape. Recall that s is the radius of a solvent particle, α is the largest surface viscosity increase seen for any particle size, D is the diffusion coefficient, η_0 is the shear viscosity in the bulk solvent, T is the absolute temperature, and k is the Boltzmann constant. Our hypothesis is that this expression should be used in place of the usual SER for the hydrodynamic measurement of size for objects of

radii up to about 10 nm.

2.3.3 Calculating transport coefficients from MD simulations

The transport coefficients in the SER, that is the shear viscosity and diffusion coefficient, were calculated from Green-Kubo expressions applied to molecular dynamics trajectories.[35] The simulated systems are described below. The shear viscosity of the bulk solvent is given by,

$$\eta = \frac{V}{kT} \int_0^\infty \langle \sum_{\alpha<\beta} \sigma_{\alpha\beta}(t)\sigma_{\alpha\beta}(0) \rangle \, \mathrm{d}t, \tag{2.21}$$

where $\sigma_{\alpha\beta}$ is the off-diagonal component of the stress tensor, V is the volume of the cubic simulation box $V = L^3$, k is the Boltzmann constant, T is the temperature, and $\langle \ldots \rangle$ denotes the canonical ensemble average. Note that this formula is suitable for calculation of the viscosity of the pure solvent. We describe the estimation of local changes in viscosity from the persistence time below.

The diffusion coefficients of the bare NPs and dendrimers were calculated using,

$$D = \frac{1}{3N_m} \int_0^\infty \langle \sum_{j=1}^{N_m} \mathbf{v}_j(t) \cdot \mathbf{v}_j(0) \rangle \, \mathrm{d}t, \tag{2.22}$$

where N_m is the particle number, $\mathbf{v}_j$ is the velocity of particle j, and $\langle \ldots \rangle$ denotes the ensemble average.

2.3.4 Local viscosity from the persistence time

Two time intervals may be defined that characterise the dynamics of the solvent in which the diffusing particle is suspended. The motion of a solvent particle is regarded as a Continuous

Time Random Walk.[30, 36] The exchange time, t_x, is defined as the random walk waiting time. More specifically, we follow Pronk *et al.* in choosing a distance over which the motion is diffusive, and regarding it as the fixed jump length in the random walk. The exchange time is then the time taken for a particle to take a step in the walk. The persistence time, t_p, is calculated as the interval between a randomly chosen time and the next exchange event, that is, the next end of a step in the random walk. Because the persistence time calculation starts at a randomly chosen time, the average persistence time is weighted towards the longest exchange times. A wide range of exchange times may arise from the dynamical heterogeneity seen in supercooled liquids and glasses, and in this case we expect t_{p} and t_{x} to become very different.

The diffusion coefficient of a solvent particle is related to the exchange time,

$$D(r) \propto \frac{1}{\langle t_x \rangle_r}, \tag{2.23}$$

where $\langle \cdot \rangle_r$ is an average over solvent particles initially a distance r from the centre of mass of the solute. We are most interested in determining the variations of these relaxation times in the vicinity of a diffusing, suspended, and roughly spherical particle. We follow the interpretation of the persistence time for supercooled liquids by regarding it as a measure of the persistence of a local structural fluctuation which affects the motion of a solvent particle passing through it.[30] We therefore expect that the local viscosity is proportional to the persistence time,

$$\eta(r) \propto kT \langle t_p \rangle_r. \tag{2.24}$$

The persistence time may be regarded as a mean first passage time, which is the time taken by a particle to reach a given distance from its start for the first time.[37–40] We choose this distance to be 1.1σ with σ being the length parameter in the Lennard-Jones potential, which is close to the position of the first peak in the radial distribution function for the solvent

particles.[30]

In calculating the changes in persistence times near a diffusing solute, we divide the surrounding region into spherical shells or bins. A persistence time is assigned to a bin if it is calculated for a particle starting in that bin. We average over all the persistence times calculated for a particular bin, and as usual over the configurations sampled from a MD trajectory. Following Pronk *et al.*, for a single configuration, we use a harmonic mean of the persistence times calculated for each bin,

$$\langle t_p \rangle_{r,f} = \frac{N_\mathrm{r}}{\sum_{i=1}^{N_\mathrm{r}} \frac{1}{t_p^i}}, \tag{2.25}$$

where f denotes the fth frame of the trajectories in the simulation, i indicates the ith solvent particle in the bin at distance r from the solute, and N_r is the total number of the solvent particles inside the bin.

We examine both the arithmetic and harmonic means of the persistence times across configurations sampled from a simulation trajectory. The two averages are,

$$\langle t_p \rangle_r^{har} = \frac{N_\mathrm{f}}{\sum_{f=1}^{N_\mathrm{f}} \frac{1}{\langle t_p \rangle_{r,f}}}, \tag{2.26}$$

and,

$$\langle t_p \rangle_r^{arith} = \frac{1}{N_\mathrm{f}} \sum_{f=1}^{N_\mathrm{f}} \langle t_p \rangle_{r,f}, \tag{2.27}$$

where f denotes the fth frame and N_f is the total number of the frames. Local viscosities are obtained from these average local persistence times as discussed above.

The local viscosities were measured by the $\langle t_p \rangle_r^{har}$ and $\langle t_p \rangle_r^{arith}$ for the composite NPs in Figure 2.5. The ratio of bulk viscosity (η^{bulk}) to local viscosity(η^{local}) was obtained as,

$$\frac{\eta^{bulk}}{\eta^{local}} = \frac{\langle t_p \rangle_{r=\frac{1}{2}L}}{\langle t_p \rangle_r}, \tag{2.28}$$

where L denotes the length of the simulation box.

2.4 Simulation methods

The particles in the simulations interact via the soft-sphere or Lennard-Jones potentials, further described below. In each simulation model a single diffusing particle is surrounded by solvent, under periodic boundary conditions. We use two models for nanoparticles without any ligands on their surfaces (see Figure 2.2 (a) and (b)). The first of these consists of a single site with a large diameter interaction, so that solvents are held at a large, chosen radius, and no tangential force acts on the solvents. The second is constructed by selecting all atoms in a cubically close-packed lattice within a certain radius of a central atom. We refer to these models as simple and composite nanoparticles, respectively. Comparison of the two provides information on the relative importance of radial and tangential forces. The dendrimer model (Figure 2.2 (c)) is an example of a flexible structure into which the solvent particles may diffuse.

The simple nanoparticle simulation system is composed of 2198 particles, including 2197 solvent atoms. The size of the simple nanoparticle is increased gradually from the size of the solvent particles. The composite nanoparticles are composed of 19, 46, 87, 156, 249, or 372 particles, and the simulation system is composed of 5324 particles in total. The core (G0) as well as the branches of the dendrimer shown in Figure 2.2 (c) are linear chains of

2M particles. There are 2197 or 5832 particles in each dendrimer simulation system. The number of particles of the solvent will change slightly with the dendrimer's size. The dendrimers are named GN-M where GN denotes the generation number of the dendrimers and M is the branch length. We will use the notations G1-1,2,3,4 and G1,2,3,4-1 in the following. G1-1,2,3,4 denotes a series of generation 1 dendrimers of varying the branch length, and G1,2,3,4-1 denotes dendrimers of various generation with each linear segment containing $2M = 2$ particles.

The interaction potentials between solvent and the simple nanoparticl, between solvent and the particles in a composite nanoparticle, and between solvent and a surface group (gray beads in Figure 2.2: (c)) of the dendrimer are of the Lennard-Jones form,

$$U_{ij}(r) = \begin{cases} 4\varepsilon[(\frac{\sigma}{r})^{12} - (\frac{\sigma}{r})^{6}] & r \leq r_c \\ 0 & r \geq r_c. \end{cases} \tag{2.29}$$

A soft sphere potential (Eq. 4.2) was used for all other interactions,

$$U_{ij}(r) = \begin{cases} \varepsilon(\frac{\sigma}{r})^{12} & r \leq r_c \\ 0 & r > r_c, \end{cases} \tag{2.30}$$

where $U_{ij}(r)$ is the potential between two atoms which are separated by a distance r, ε indicates the interaction strength, σ is the length parameter, and r_c is the cutoff radius. The monomers of the dendrimers interact with the neighbouring ones by rigid bonds. The bond length is 1 in the unit of Lennard-Jones which is fixed by the SHAKE algorithm.

The simulations were carried out in a cubic box. At least 100,000 time steps were performed to ensure the equilibration followed by 13 million time steps for the viscosity of the

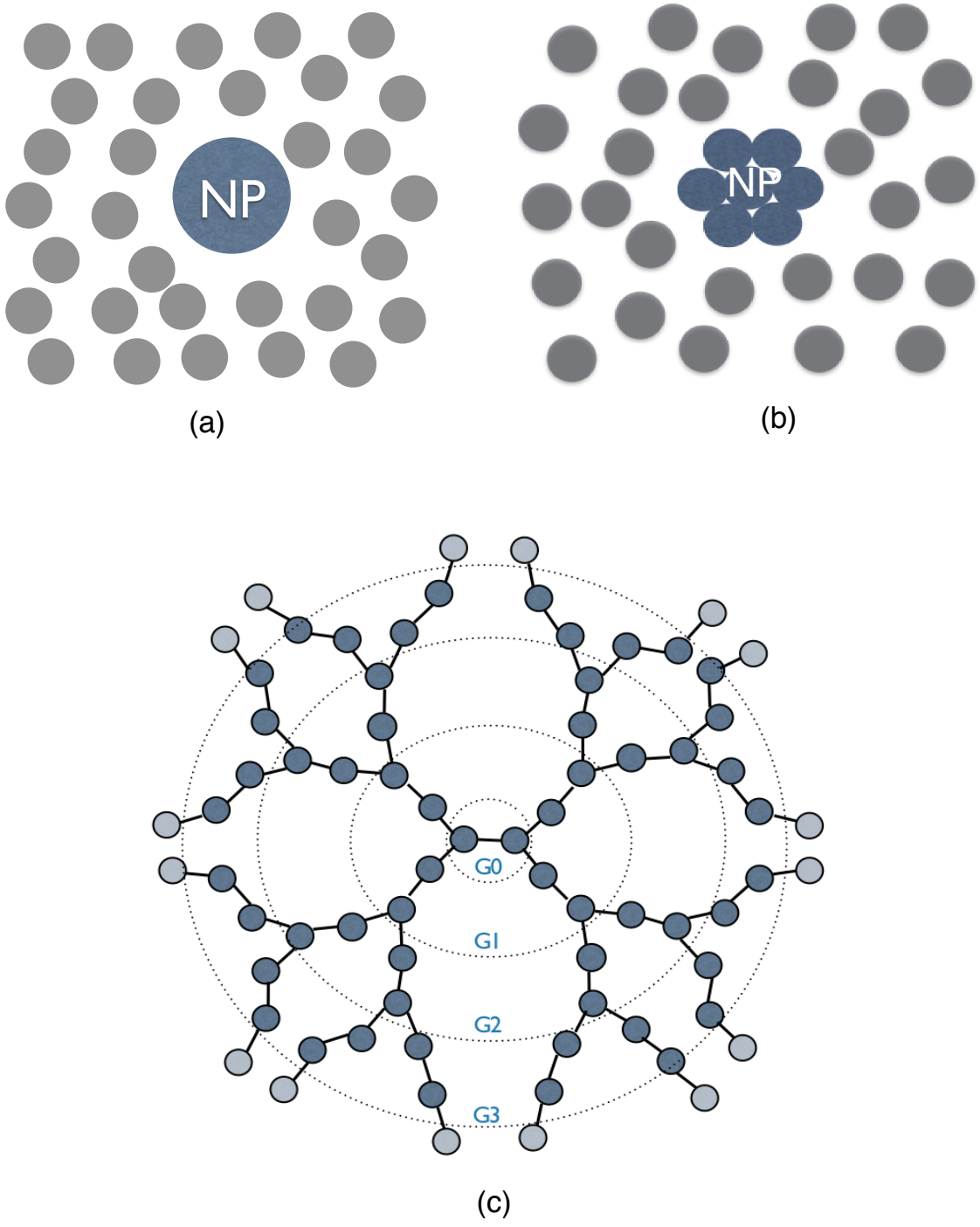

Figure 2.2: (a): Schematic showing simple bare nanoparticle with solvent. (b): Schematic showing bare composite nanoparticle with solvent. The nanoparticle is composed of many particles which are the same as the solvent particles. (c): Generic dendrimer structure with formulae GN-M. GN indicates the generation number and M is the length of a branch.

solvent to converge and by 2 to 7 million time steps for the diffusion of the solutes. The time step is $\Delta t = 0.001 m^{\frac{1}{2}} \sigma \varepsilon^{-\frac{1}{2}}$. All transport coefficients were calculated in the NVT ensemble. The box length is 16σ for the simple NPs, dendrimers G1,2,3,4 and G2,3-1, 22.15σ for dendrimer G4-1 and 21.5σ for the composite NPs. The temperature is $T = 3\epsilon k^{\frac{1}{2}}$. The Nose-Hoover chain thermostat is applied to balance the temperature. The relaxation time of the thermostat is $\tau = 0.25 m^{\frac{1}{2}} \sigma \varepsilon^{-\frac{1}{2}}$.

2.5 Results and discussion

We examine first differences between the hydrodynamic and structural radii of real and simulated particles. The differences vary with the sizes of the particles. Following previous work,[18, 30] we examine the possibility that a change in shear viscosity in the neighbourhood of the particle is responsible for size variation of the difference between the hydrodynamic and structural sizes. We test this hypothesis by comparison of the drag law derived above, eq 2.17 and 2.20, with measured and simulated hydrodynamics. In order to further test our proposed modification of Stokes' law we use the persistence time method to estimate changes in viscosity near simulated diffusing particles from changes in the persistence time of solvent motions.

2.5.1 Structural and hydrodynamic radii

The hydrodynamic radii r_{h} as functions of the structural sizes R, or R_{g}, for the real and simulated particles, are shown in Figure 2.3. The four types of particles are real nanoparticles with grafted oligomers, as measured by SV-AUC which are from Demeler and Lees's work[41, 42] ; simulated dendrimers; simulated 'simple' nanoparticles; and simulated composite nanoparticles.

The axes in Figure 2.3 are the measured sizes of grafted nanoparticles. The other data refer to simulations that use reduced, dimensionless units. The comparison therefore requires that we choose a length scale for each simulation. The length we choose is σ, described above, is the diameter of the soft-sphere solvent particle. For the simple nanoparticles we choose $\sigma_{\rm s} = 0.5$ nm, for the composite nanoparticles $\sigma_{\rm c} = 1.0$ nm, and for the dendrimers $\sigma_{\rm d} = 0.5$ nm. For each set of simulated data in dimensionless reduced units, both the hydrodynamic radii, $r_{\rm h}^*$, and the structural radii R^*, or $R_{\rm g}^*$, are multiplied by the relevant length σ. More specifically, for the simple nanoparticles we use,

$$r_{\rm h} = \sigma_{\rm s} r_{\rm h}^*, \tag{2.31}$$

$$R = \sigma_{\rm s} R^*, \tag{2.32}$$

where R^* is the radius of the simple nanoparticle that appears in the interaction potential between the particle and the surrounding solvent (see Simulation methods section above for details). For the composite nanoparticles we use,

$$r_{\rm h} = \sigma_{\rm c} r_{\rm h}^*, \tag{2.33}$$

$$R = \sigma_{\rm c} R_{\rm g}^*. \tag{2.34}$$

Note carefully that here we use the radius of gyration of the composite nanoparticle $R_{\rm g}^*$. For the dendrimers we use,

$$r_{\rm h} = \sigma_{\rm d} r_{\rm h}^*, \tag{2.35}$$

$$R = \sigma_{\rm d} R_{\rm g}^*. \tag{2.36}$$

Of the three types of nanoparticles and dendrimers, with various surface structures, some fall on the line $r_{\rm h} = R$ in Figure 2.3, and so obey Stokes' law. Others fall close to a different

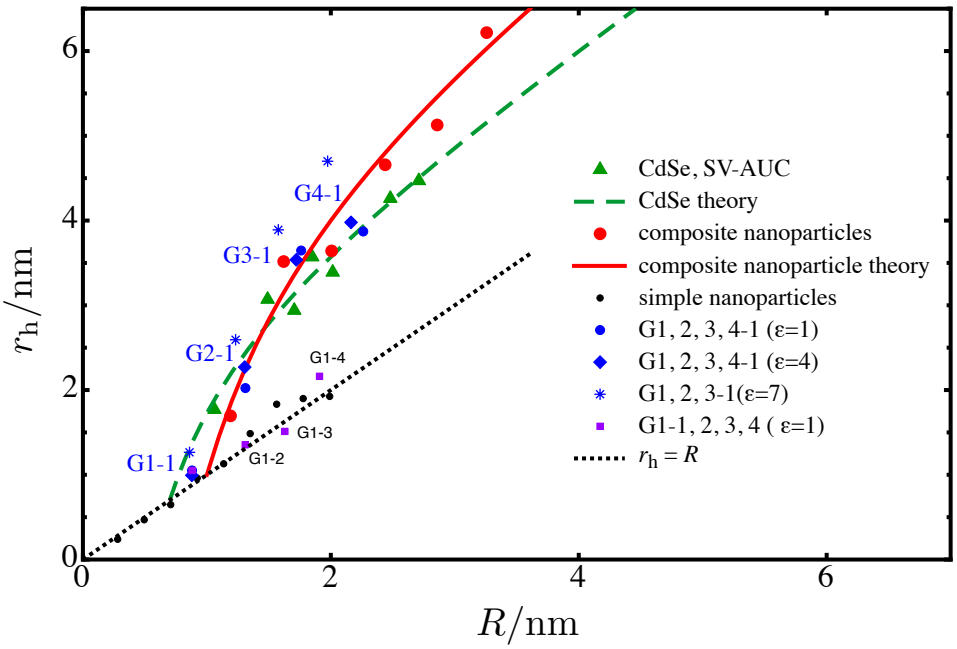

Figure 2.3: Hydrodynamic radii (r_h) of the CdSe nanoparticles from Demeler[41] and Lees[42] (green triangles) in comparison to those of the dendrimers (blue symbols), composite nanoparticles (red points) and simple nanoparticles (black circles). ε is the interaction force parameter. The two theory curves are based on eq 2.18, and the relevant parameters are given in Table 2.1.

curve, with hydrodynamic radii higher than structural radii. Note that all hydrodynamic radii in Figure 2.3 are obtained on the assumption that the standard form of the SER holds. It is the simple, bare nanoparticles, and the low density dendrimers that obey the SER; and the more complex particles that break it. We have plotted the usual r_h, rather than our improved $\hat{r}_h$, because this allows us to distinguish the two behaviours. Note that agreement of simulated data with the theory curves shown implies that eq 2.20 correctly predicts the true size as shown by Figure A2.4 in the Appendix.

The simple bare nanoparticles are constructed from single, simulated interaction sites, with a spherically symmetric potential describing the interaction with nearby solvent particles. Tangential forces on solvent particles near the surface of the solute are therefore absent,

and slip boundary conditions apply. Using the slip boundary version of Stokes' law, we find as expected that the hydrodynamic and structural sizes match well. Note that it is only for these simple, single-site particles that we use slip boundary conditions. Recall that in deriving and discussing eq 2.10 above we noted that the new term in the drag law arose from the tangential component of the force and does not depend on the thickness of the layer of increased viscosity, and that other terms in tangential and radial force components both cancel exactly. The importance of the tangential force is born out by the observation that simulated simple nanoparticles obey the SER.

The low density dendrimers, with a single generation, denoted G1-1, G1-2, G1-3, and G1-4 also obey Stokes' law, with stick boundary conditions. Note that by this we mean that the hydrodynamic radius obtained from the simulated diffusion of the particle is in agreement with its radius of gyration, and that this holds as the dendrimer doubles in radius. Our simulated solvent model is simple, a soft-sphere fluid of liquid-like density, and we have confirmed that it produces either stick or slip-like Stokes drag, depending on the particle structure. It is possible for a linear or slightly branched polymer to exhibit different dependences of hydrodynamic and structural size on mass, and such a species would not lie on the line $r_{\mathrm{h}} = R$ in Figure 2.3. Our slightly branched species, dendrimers G1-1, G1-2, G1-3, and G1-4, do lie on that line.

We can rule out any deviation from Stokes' law that occurs simply because the solute is only slightly larger than the solvent particles, because we have observed the SER works for both simple nanoparticles and generation 1 dendrimers.

Dendrimers of increasing generation become rapidly more dense at their centres, with a sharper fall of density towards their outer edges. We examine also a series of dendrimers

that increase not only in size but also in generation, denoted G1-1, G2-1, G3-1, and G4-1. Three sets of such dendrimers with three different interaction strengths between the solvent and the particles on the outermost ends of the dendrimers branches, $\epsilon = 1, 4$, and 7, are studied. These dendrimers have hydrodynamic radii that grow more quickly than the structural radii, R. Recall that the structural radii for the dendrimers are calculated as radii of gyration (see above for details). The solvent interaction strength does have a weak influence on the hydrodynamic radii, but only when the depth of the potential energy well is set to 7, corresponding to solvent particles that can bind tightly to the dendrimer.

The striking effect on the hydrodynamic radii appears when we increase not only the size of the dendrimer, but also its generation. We have confirmed that Stokes' law with stick boundaries at the gyration radius holds for generation 1 dendrimers, G1-1, G1-2, G1-3, and G1-4, and found that Stokes' law breaks down when the generation is increased without changing solvent, monomers, bonds, or interactions, in the series G1-1, G2-1, G3-1, and G4-1.

We note that the deviations from Stokes' law for simulated composite nanoparticles, which have no ligands, for dendrimers of increasing generation are approximately the same. The slight outliers are the data for dendrimers with very strong solvent interactions. We note that for the real nanoparticles, the structural radius is the core radius that does not include the ligands. We might expect that this definition resembles the gyration radius for the dendrimers of increasing generation, as in both cases oligomeric structures extend outside the structural radius. However we might choose to describe the sizes of our particles, we find for particles of sufficient internal density that exert tangential forces on solvent at their peripheries, very similar deviations from Stokes' law. The form of this deviation is not sensitive to the surface structure, and so we can rule out ligands at the surface as a source of this deviation.

The simple, single-site, simulated nanoparticles obey Stokes' law, and exert no tangential force on the solvent. This points to the tangential force as the origin of the change in the drag law. This agrees with previous study by Ortiz-Young *et al.*,[18] who investigated the normal and shear forces in water as an AFM tip approached flat surfaces, and found for surfaces with low wettabilities that the tangential force increases more significantly as the tip approaches the surface.[18] We conclude that the radial component of the force is little affected by the local dynamics of the solvent, but the tangential component increases significantly, and in a manner consistent with a local increase in viscosity.

2.5.2 Magnitude of changes in viscosity

Using the modified Stokes-Einstein relation, eq 2.17, we calculated the local viscosity needed to bring the hydrodynamic radii into agreement with the structural radii, $\hat{r}_{\mathrm{h}} = R$. The simulated composite nanoparticles and measured CdSe QDs have local viscosities that give $\hat{r}_{\mathrm{h}} = R$ a little over twice the bulk. These estimated local viscosity increases are shown in Figure 2.4. The predictions of eq 2.18 are also shown in Figure 2.4, and these match experiment and simulation as appropriate. The parameters used are shown in Table 2.1.

We compared our ratios of local to bulk viscosities with those reported for flat surfaces, curved surfaces, and the surfaces of proteins, all in water, obtained from molecular dynamics simulations. The data is indicated by stars in Figure 2.4. The hydrophobic or weakly hydrophilic surfaces show local viscosities near 2 to 3.5 times larger than the bulk viscosity. The increase in viscosity near a protein surface is a factor of 2 or 3. Taking our results together with the reported values,[30] we find that the measured diffusion coefficients are consistent with tangential drag force increased by a factor of 2 to 3. Note that Pronk *et al.* also discussed charged surfaces, and interpreted their behaviour in terms of interaction strength.

We do not discuss strongly hydrophilic surfaces here.

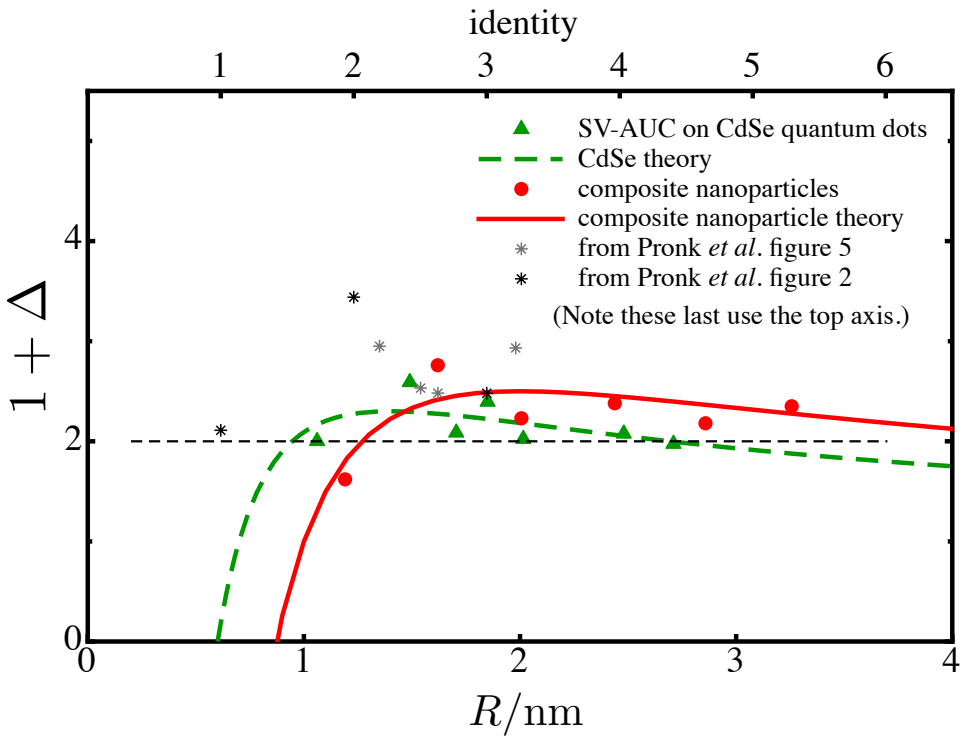

Figure 2.4: The ratio of bulk viscosity η^{bulk} to local viscosity η^{local} as a function of R for simulated composite nanoparticles (red solid circles), and for simulated proteins (stars). Note that for the second set of protein data from Pronk *et al.*, the upper horizontal axis is used, which does not indicate size, but rather numbers of the systems as in the original publication. These are: 1 - water near silica (c=0); 2 - water near silica (c=0.5); 3 - L-J fluids near a L-J particle surface. The parameter c controls surface charge. The two theory curves correspond to those in Figure 2.3, and use the parameters in Table 2.1. The black dashed line is $\frac{\eta^{local}}{\eta^{bulk}} = 2$.

Table 2.1: Parameters used to obtain the theory curves in Figures 2.4.

	α	s/nm
CdSe nanoparticle	1.3	0.7
composite simulated nanoparticle	1.5	1.0

2.5.3 Local viscosity from persistence times

As discussed above, the persistence time for solvent motions provides an estimate for a local change in viscosity. Noting the similarity between the effective viscosity increases seen in our work and those reported by Pronk *et al.*, we follow their approach and calculate the dependence of solvent persistence time on distance from the solute. The results reported so far indicate that measured diffusion coefficients are consistent with a local viscosity increase. Calculation of the persistence times from our molecular dynamics simulations provides an independent test of the hypothesis that the viscosity increases near the diffusing particle.

The locally averaged persistence times near the simulated composite nanoparticles are plotted in Figure 2.5. The t_p increases near the nanoparticle of various sizes regardless of which type of average over multiple configurations was used. Use of the arithmetic mean gives increases in persistence times consistent with the increase in local viscosities shown in Figure 2.4. The ratio of the local viscosity to bulk solvent viscosity depends only weakly on the sizes of the nanoparticles, which agrees with that from the modified form of the Stokes-Einstein relation mentioned above.

The method of averaging across simulated configurations influences the increase in persistence time. It is roughly 2 times that of the bulk using the arithmetic mean (Figure 2.5(a) and (b)), and roughly 1.3 times using the harmonic mean (Figure 2.5(c) and (d)). The harmonic mean gives relatively less weight to the large persistence times. The broad distribution of persistence times that this implies is expected.[30] Pronk *et al.* argue for the use of the harmonic mean.

The ratios of bulk solvent viscosity to local viscosity for our simulated dendrimers are plotted in Figure 2.6, obtained using both the arithmetic and harmonic mean. In both cases,

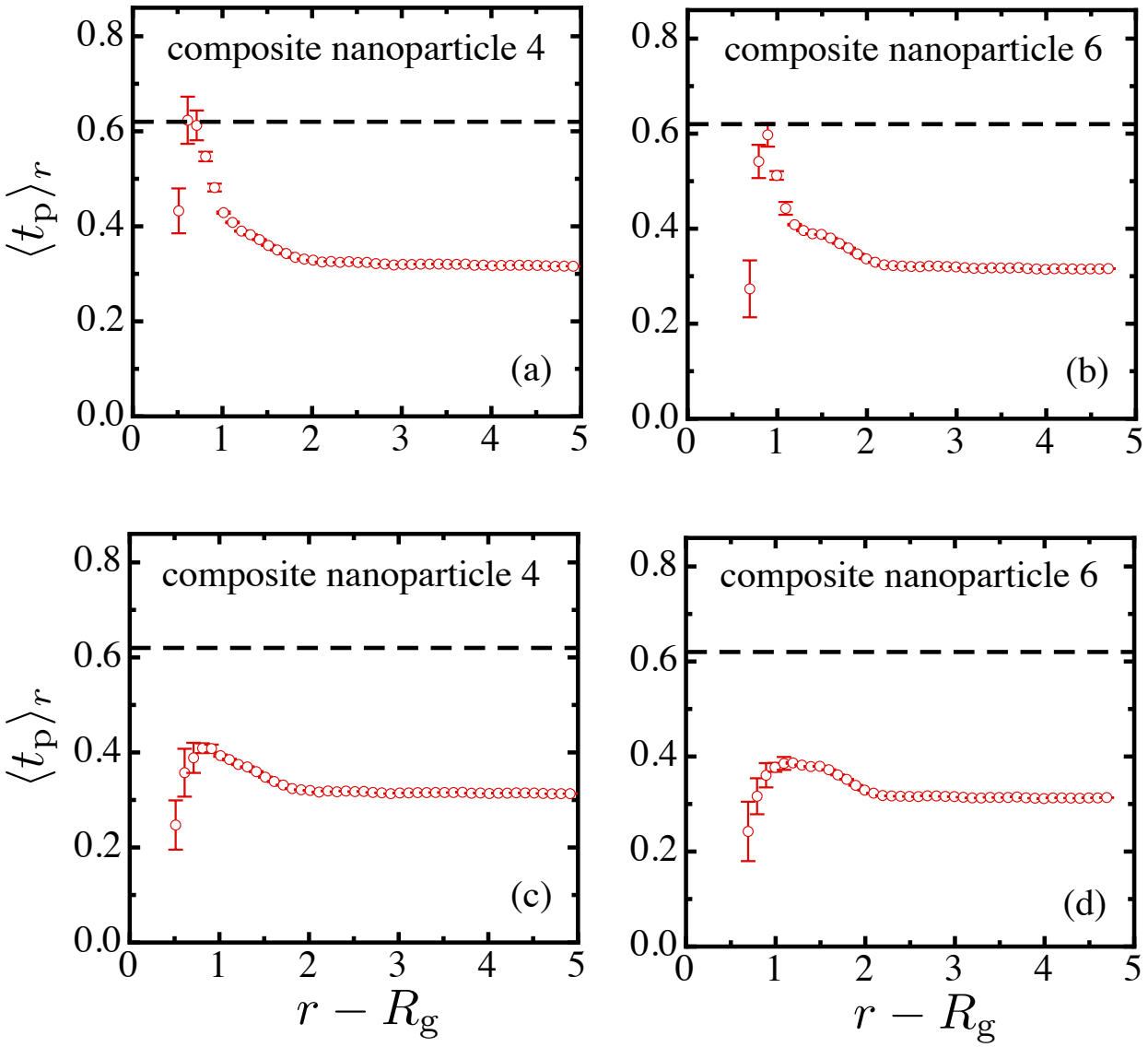

Figure 2.5: Persistence time t_p as a function of $(r - R_g)$ for the bare composite NPs. The dashed lines are twice the bulk persistence time. r is the distance to the COM of the NPs, σ is the length parameter, m is the mass of a solvent particles and ε is the interaction force parameter. The persistence times of solvent particles inside each circular bin were averaged by a harmonic mean. The $\langle t_p \rangle$ obtained from multiple configurations were averaged by an arithmetic mean as shown in a, b and by a harmonic mean as shown in c, d. The 'composite NP x' stands for the xth composite NP (see above for details). t_p of other four bare composites NPs can be found in the Appendix.

the results are compared to the corresponding data reported for proteins. The ratios tend to decrease in the neighbourhood of the dendrimers. Using the arithmetic average, both

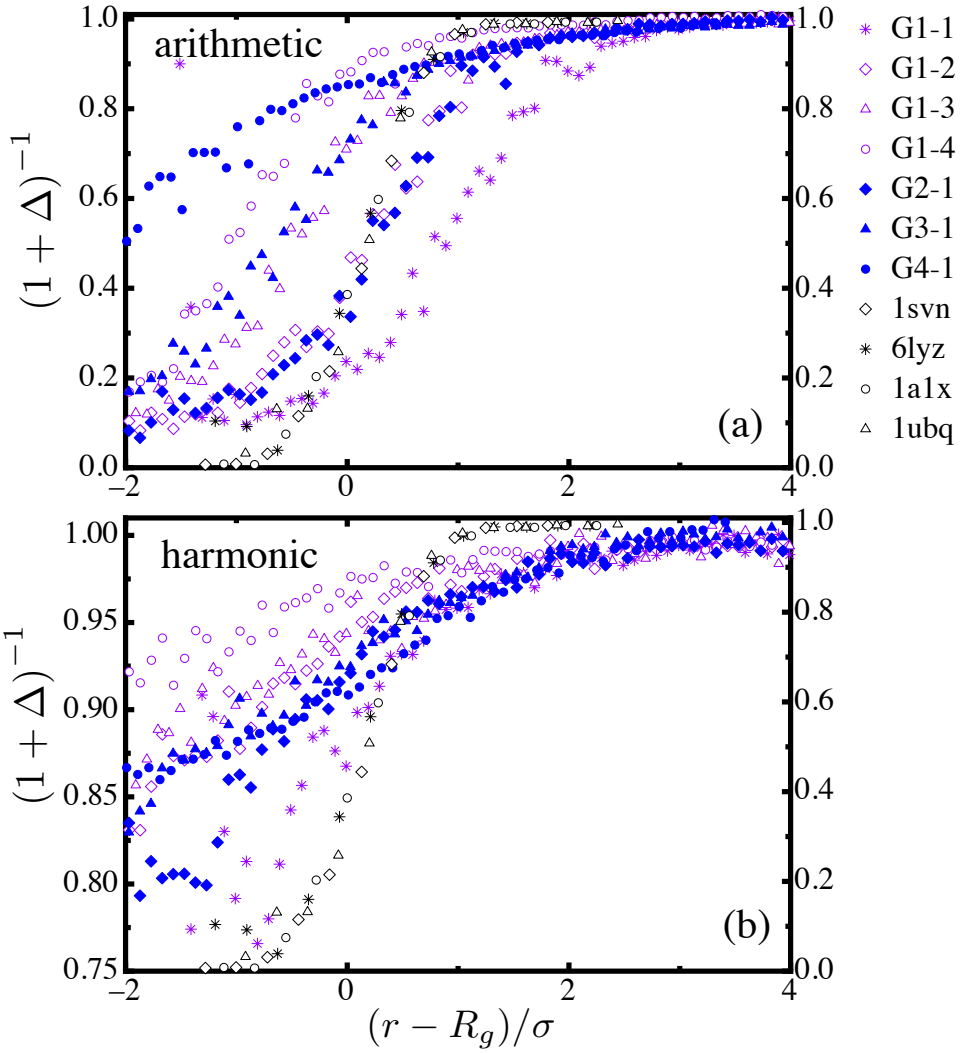

Figure 2.6: The ratio of bulk and local viscosity of solvent from t_p as a function of the distance to R_g of the dendrimers G1-1,2,3,4 (purple symbols) and G2,3,4-1 (blue symbols) compared with those of the proteins (black symbols) taken from the literature.[30] The dendrimers correspond to the left Y axis and the proteins correspond to the right Y axis. The *arithmetic* and *harmonic* stand for that the persistence times were obtained by arithmetic average and harmonic average over multiple configurations, respectively. r is the distance to the center of mass of the NPs and σ is the length parameter.

series of dendrimers show the biggest change in local viscosity for the smallest dendrimer. The effect is similarly strong for the two sets of dendrimers. The behaviour of the harmonic mean is quite different. For the series of dendrimers with increasing generation, G1-1, G2-1, G3-1, to G4-1, the viscosity change near the particle is nearly constant. For the series of

first generation dendrimers, G1-1, G1-2, G1-3, to G1-4, the viscosity change near the particle becomes weaker as the particle grows. The viscosity change for G1-4 is about one third of that for G1-1. G4-1 has a viscosity change almost identical to the G1-1. The harmonic mean results match the effective viscosity changes qualitatively shown above in Figure 2.4, confirming the use of the harmonic mean reported in the literature.[30]

2.6 Conclusions

We find that deviations from Stokes' law for the drag on a spherical object in a viscous fluid are consistent with an increase in the shear viscosity near the particle. We find agreement between theory and experiment, and between theory and simulation, shown in Figure 2.3 and 2.4. These results support the hypothesis that eq 2.20 should be used in place of the usual SER in hydrodynamic size determination.

This conclusion is based on simulations of, and comparisons between, three types of particles. These are a simple, single-site, particle that exerts no tangential force on the surrounding solvent; a composite nanoparticle made up of solvent-like particles assembled in a face-centred cubic structure; a sequence of first generation dendrimers; and a sequence of dendrimers of increasing generation. These particles allow us to reproduce the standard Stokes drag law; to isolate the tangential and normal components of the drag force; and to rule out the effects of ligands at the particle surface. The hypothesis of increased effective viscosity is consistent with the measured diffusivity, and receives independent support from the calculation of persistence times, which increase in the neighbourhood of the simulated particles.

We find that the deviation from Stokes' law depends only weakly on the strength of the forces between the solute and solvent. The deviation is not affected by the presence of

ligands at the surface. These observations are consistent with the interpretation of the hydrodynamic radii in terms of persistence times. A distribution of persistence times reflects a distribution of possible structures, a dynamical heterogeneity, and the appearance of 'slow' structures with increases in viscosity. We find that the diffusing solutes which exclude solvent, as the dendrimers that increase in generation as they grow show longer persistence times for nearby solvent. Particles into which the solvent can pass show some increase in persistence time, but this becomes weak as the particles grow. The presence of a sufficiently dense diffusing particle constrains the motion of nearby solvent, and so increases the local viscosity. This in turn slows the diffusion of the particle and leads to the deviation from Stokes' law. Determination of this increase in viscosity allows for an improvement in calibration for the dynamical measurement of the sizes of particles in the nanometre size range.

Our results show that the pattern of increased viscosity proposed for proteins and surfaces of varying hydrophilicity[30] also applies to a wide range of particles, and most importantly to nanoparticles bearing grafted ligands. In the latter case the ligands are typically chemically similar to the solvent, so as to promote dispersion of the particles into the solvent. Under these conditions the ligands at the surface behave like solvent molecules with very high persistence times.

Appendix

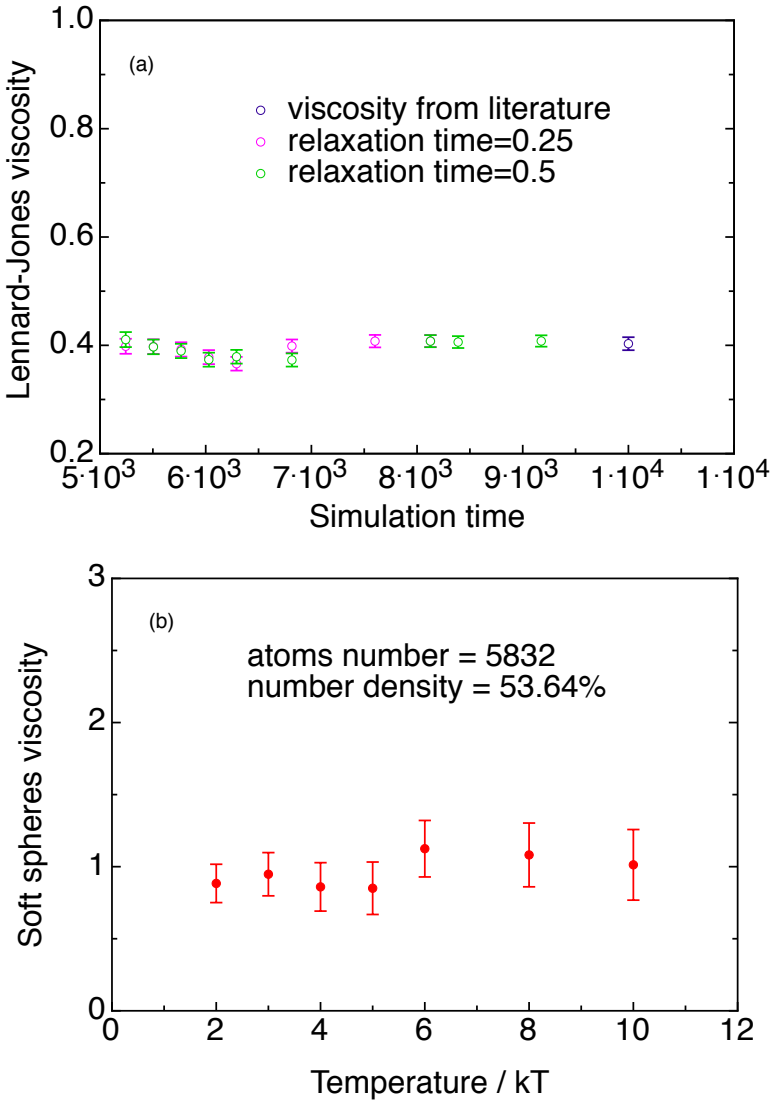

Figure A2.1: (a): The viscosity of the Lennard-Jones liquids (∘ and ∘) compared with the data from Cappelezzo (∘).[43] The main simulation parameters are the number density of the spheres $\frac{N}{V} = 40\%$, the temperature $kT = 1.5$ in units of ϵ. The error bars refer to the standard error. (b): The viscosity of the solvent (soft spheres) calculated from MD simulations. The main simulation parameters are the number density of the spheres $\frac{N}{V} = 53.64\%$, atom number = 5832. The error bars are plotted as the standard deviation. The viscosity is in unit of $\frac{\sqrt{m\epsilon}}{\sigma^2}$ and the *simulation time* is in units of $\sqrt{\frac{m\sigma^2}{\epsilon}}$, where m is the mass of particle, σ is the length parameter and ϵ is the interaction strength parameter.

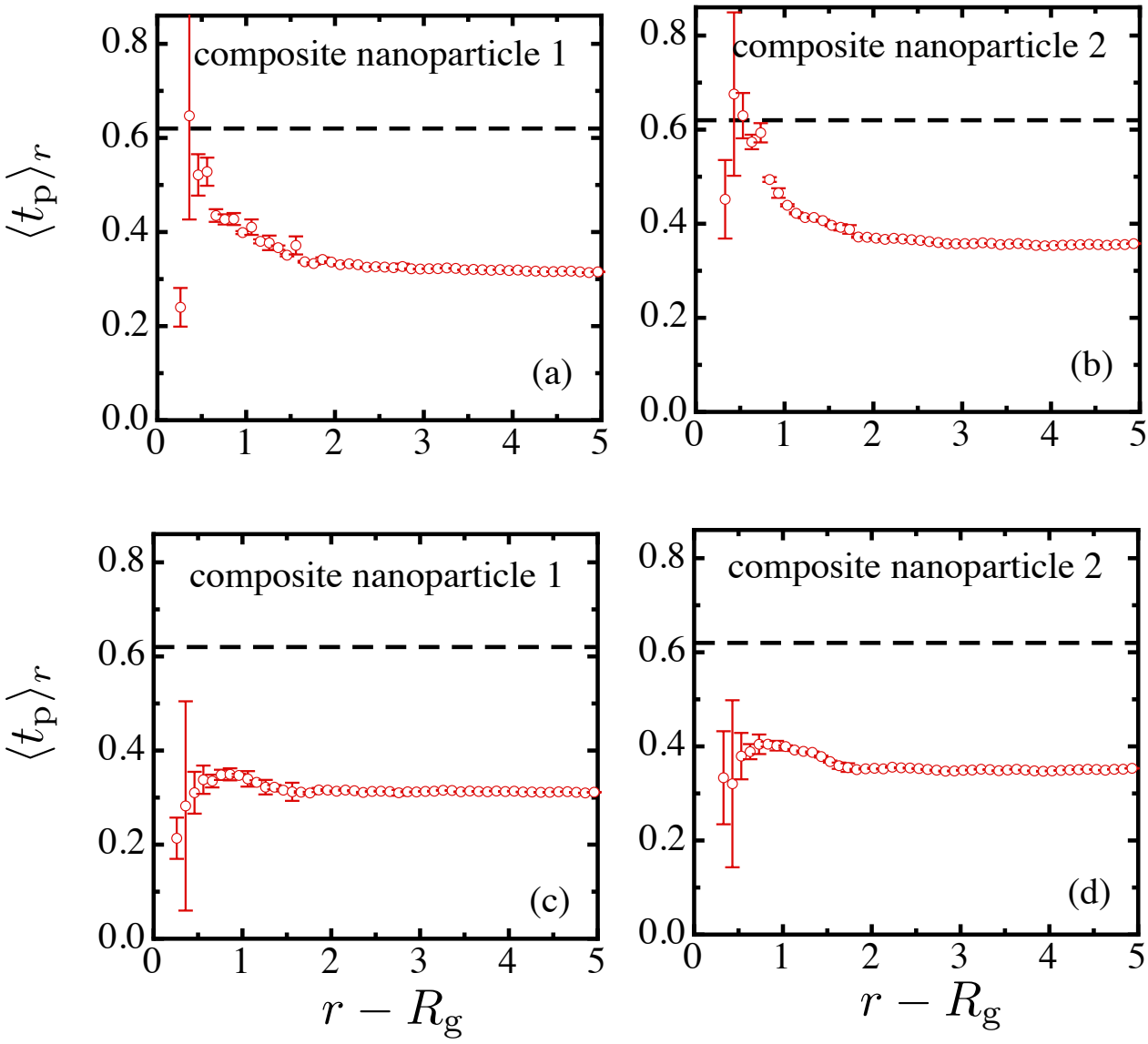

Figure A2.2: Persistence time t_p as a function of $(r - R_g)$ for the bare composite NP 1 and 2.

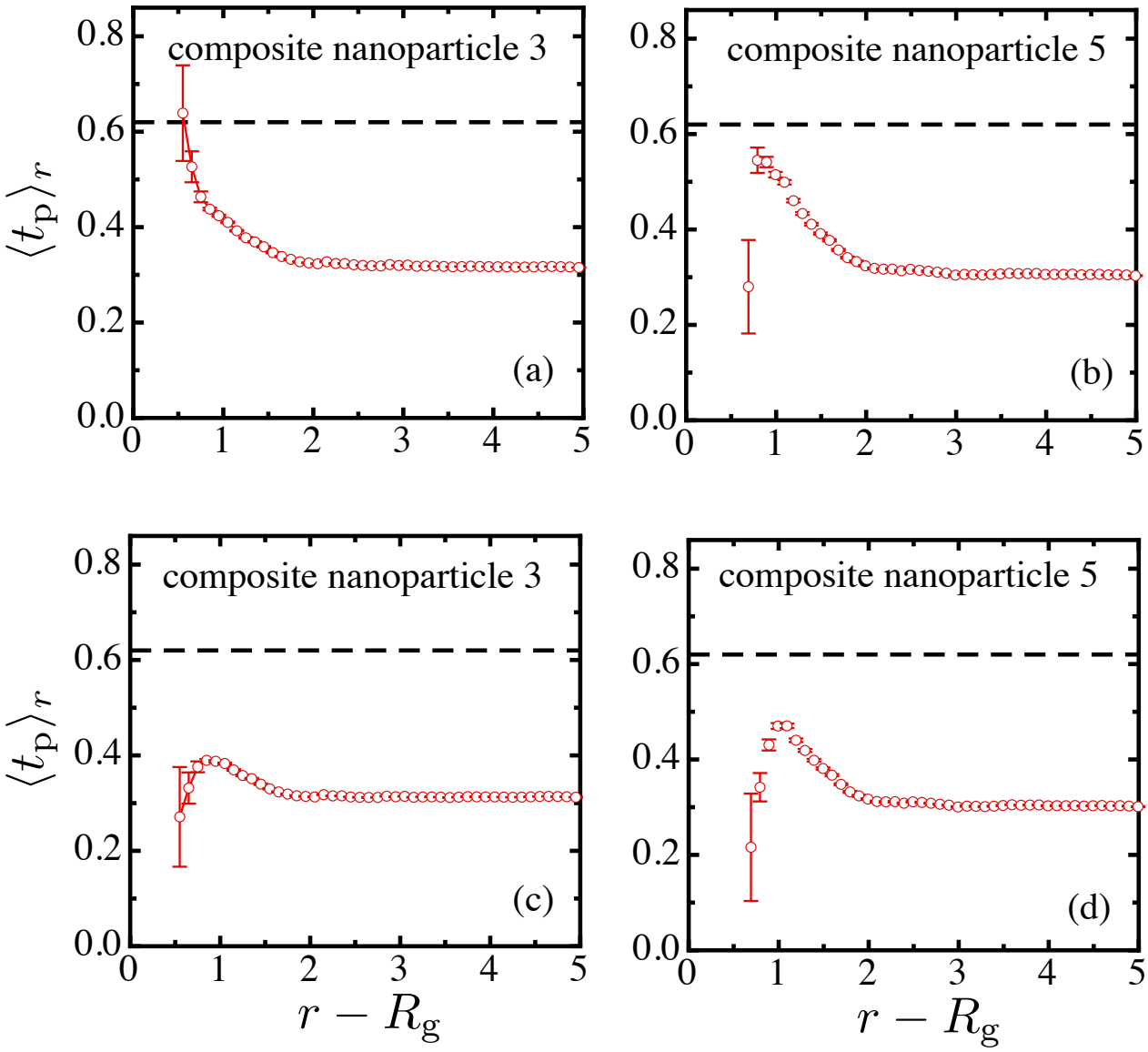

Figure A2.3: Persistence time t_p as a function of $(r - R_g)$ for the bare composite NP 3 and 5.

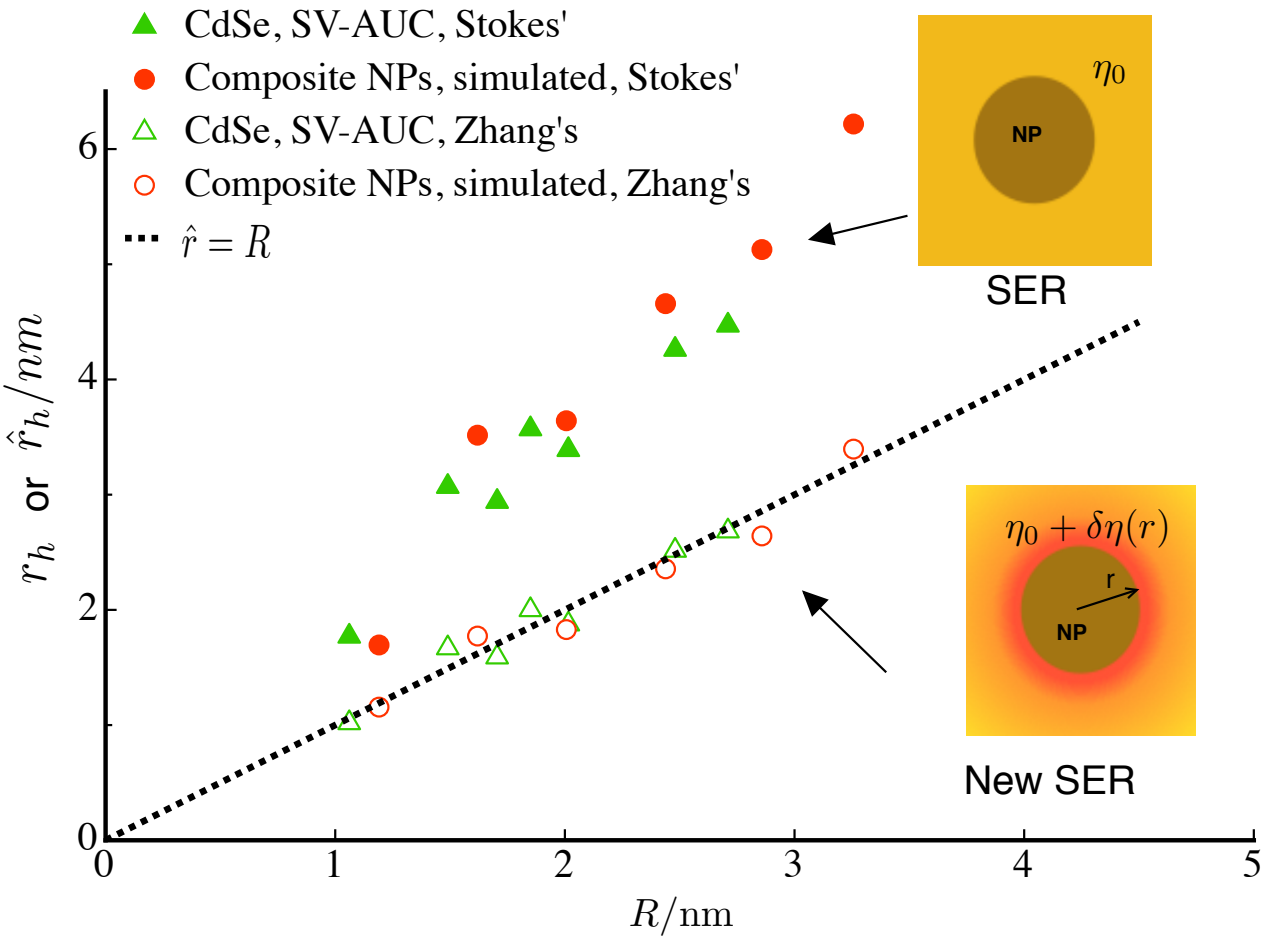

Figure A2.4: Hydrodynamic radius r_h obtained from the SER and the new hydrodynamic radius $\hat{r}_\mathrm{h}$ obtained from the new SER of our simulated nanoparticles and experimental nanoparticles from literatures as a function of structural radius R.

Bibliography

[1] J. A. Jamison, K. M. Krueger, C. T. Yavuz, J. T. Mayo, D. LeCrone, J. J. Redden, and V. L. Colvin. Size-dependent sedimentation properties of nanocrystals. *ACS Nano*, 2(2):311–319, 2008.

[2] R. P. Carney, J. Y. Kim, H. Qian, R. Jin, H. Mehenni, F. Stellacci, and O. M. Bakr. Determination of nanoparticle size distribution together with density or molecular weight by 2d analytical ultracentrifugation. *Nat. Commun.*, 2:335, 2011.

[3] J. M. Zook, V. Rastogi, R. I. Maccuspie, A. M. Keene, and J. Fagan. Measuring agglomerate size distribution and dependence of localized surface plasmon resonance absorbance on gold nanoparticle agglomerate size using analytical ultracentrifugation. *ACS nano*, 5(10):8070–8079, 2011.

[4] Y. Dieckmann, H. Cölfen, H. Hofmann, and A. Petri-fink. Particle size distribution measurements of manganese-doped ZnS nanoparticles. *Anal. Chem.*, 81(10):3889–3895, 2013.

[5] J. R. Schmidt and J. L. Skinner. Brownian motion of a rough sphere and the Stokes-Einstein law. *J. Phys. Chem. B*, 108(21):6767–6771, 2004.

[6] J. Kim and T. Keyes. On the breakdown of the Stokes-Einstein law in supercooled liquids. *J. Phys. Chem. B*, 109(45):21445–21448, 2005.

[7] S. Chen, F. Mallamace, C. Mou, M. Broccio, C. Corsaro, A. Faraone, and L. Liu. The violation of the Stokes – Einstein relation in supercooled water. *Proc. Natl. Acad. Sci. USA*, 103:12974–12978, 2006.

[8] Z. Li. Critical particle size where the Stokes-Einstein relation breaks down. *Phys. Rev. E*, 80(6):061204, 2009.

[9] P. Kumar, S. V. Buldyrev, S. R. Becker, P. H. Poole, F. W. Starr, and H. E. Stanley. Relation between the Widom line and the breakdown of the Stokes-Einstein relation in supercooled water. *Proc. Natl. Acad. Sci. USA*, 104(23):9575–9579, 2007.

[10] L. Xu, F. Mallamace, Z. Yan, F. W. Starr, S. V. Buldyrev, and H. Eugene Stanley. Appearance of a fractional Stokes–Einstein relation in water and a structural interpretation of its onset. *Nat. Phys.*, 5(8):565–569, 2009.

[11] A. Tuteja, M. E. Mackay, S. Narayanan, S. Asokan, and M. S. Wong. Breakdown of the continuum Stokes-Einstein relation for nanoparticle diffusion. *Nano lett.*, 7(5):1276–1281, 2007.

[12] J. C. Araque, S. K. Yadav, M. Shadeck, M. Maroncelli, and C. J. Margulis. How is diffusion of neutral and charged tracers related to the structure and dynamics of a room-temperature ionic-liquid? Large deviations from Stokes-Einstein behavior explained. *J. Phys. Chem. B*, 119:7015–7029, 2015.

[13] B. Halle and M. Davidovic. Biomolecular hydration: from water dynamics to hydrodynamics. *Proc. Natl. Acad. Sci. USA*, 100(21):12135–12140, 2003.

[14] T. D. Li, J. Gao, R. Szoszkiewicz, U. Landman, and E. Riedo. Structured and viscous water in subnanometer gaps. *Phys. Rev. B*, 75(11):115415, 2007.

[15] M. P. Goertz, J. E. Houston, and X. Y. Zhu. Hydrophilicity and the viscosity of interfacial water. *Langmuir*, 23(10):5491–5497, 2007.

[16] T. D. Li and E. Riedo. Nonlinear viscoelastic dynamics of nanoconfined wetting liquids. *Phys. Rev. Lett.*, 100(10):106102, 2008.

[17] S. H. Khan, G. Matei, S. Patil, and P. M. Hoffmann. Dynamic solidification in nanoconfined water films. *Phys. Rev. Lett.*, 105(10):106101, 2010.

[18] D. Ortiz-Young, H. Chiu, S. Kim, K. Voïtchovsky, and E. Riedo. The interplay between apparent viscosity and wettability in nanoconfined water. *Nat. Commun.*, 4:2482, 2013.

[19] D. J. Acheson. *Elementary Fluid Dynamics*. Oxford University Press, 1990.

[20] P. A. Thompson and M. Robbins. Shear flow near solids: Epitaxial order and flow boundary conditions Peter. *Phys. Rev. A*, 41(12):6830–6837, 1990.

[21] P. A. Thompson and S. M. Troian. A general boundary condition for liquid flow at solid surfaces. *Nature*, 389:360–362, 1997.

[22] J. J. Kuna, K. Voïtchovsky, C. Singh, H. Jiang, S. Mwenifumbo, P. K. Ghorai, M. M. Stevens, S. C. Glotzer, and F. Stellacci. The effect of nanometre-scale structure on interfacial energy. *Nat. Mater*, 8(10):837–842, 2009.

[23] J. Liu, D. Cao, and L. Zhang. Molecular dynamics study on nanoparticle diffusion in polymer melts: A test of the Stokes-Einstein law. *J. Phys. Chem. C*, 112(17):6653–6661, 2008.

[24] I. Kohli and A. Mukhopadhyay. Diffusion of nanoparticles in semidilute polymer solutions: Effect of different length scales. *Macromolecules*, 45:6143–6149, 2012.

[25] R. Zangi and L. Kaufman. Frequency-dependent Stokes-Einstein relation in supercooled liquids. *Phys. Rev. E*, 75(5):051501, 2007.

[26] F. Puosi and D. Leporini. Communication: Fast and local predictors of the violation of the Stokes-Einstein law in polymers and supercooled liquids. *J. Chem. Phys.*, 136(21):211101, 2012.

[27] O. Blondel and C. Toninelli. Is there a breakdown of the Stokes-Einstein relation in Kinetically Constrained Models at low temperature? *EPL*, (1):1–5, 2013.

[28] S. V. Castrillón, N. Giovambattista, U. A. Aksay, and P. G. Debenedetti. Evolution from surface-influenced to bulk-like dynamics in nanoscopically confined water. *J. Phys. Chem. B*, 113(23):7973–7976, 2009.

[29] K. Falk, F. Sedlmeier, L. Joly, R. R. Netz, and L. Bocquet. Molecular origin of fast water transport in carbon nanotube membranes: Superlubricity versus curvature dependent friction. *Nano Lett.*, 10(10):4067–4073, 2010.

[30] S. Pronk, E. Lindahl, and P. M. Kasson. Dynamic heterogeneity controls diffusion and viscosity near biological interfaces. *Nat. Commun.*, 5:3034, 2014.

[31] F. W. Starr, T. B. Schrø der, and S. C. Glotzer. Molecular dynamics simulation of a polymer melt with a nanoscopic particle. *Macromolecules*, 35(11):4481–4492, 2002.

[32] L. Pozhar. Structure and dynamics of nanofluids: Theory and simulations to calculate viscosity. *Phys. Rev. E*, 61(2):1432–1446, 2000.

[33] H. Hoang and G. Galliero. Local viscosity of a fluid confined in a narrow pore. *Phys. Rev. E*, 86(2):1–10, 2012.

[34] N. Tretyakov and M. Müller. Correlation between surface topography and slippage: A molecular dynamics study. *Soft Matter*, 9(13):3613, 2013.

[35] D. C. Rapaport. *The art of molecular dynamics simulation.* Cambridge University Press, 1995.

[36] Y. Jung, J. P. Garrahan, and D. Chandler. Dynamical exchanges in facilitated models of supercooled liquids. *J. Chem. Phys.*, 123(8):1–11, 2005.

[37] E. W. Montroll and G. H. Weiss. Random walks on lattices. II. *J. Math. Phys.*, 6(2):167, 1965.

[38] E. W. Montroll. Random walks on lattices. III. Calculation of first-passage times with application to exciton trapping on photosynthetic units. *J. Math. Phys.*, 10(4):753, 1969.

[39] P. Reimann, G. J. Schmid, and P. Hänggi. Universal equivalence of mean first-passage time and Kramers rate. *Phys. Rev. E*, 60(1):R1–R4, 1999.

[40] L. O. Hedges, L. Maibaum, D. Chandler, and J. P. Garrahan. Decoupling of exchange and persistence times in atomistic models of glass formers. *J. Chem. Phys.*, 127(21):1–4, 2007.

[41] B. Demeler, T. L. Nguyen, G. E. Gorbet, V. Schirf, E. H. Brookes, P. Mulvaney, A. O. El-Ballouli, J. Pan, O. M. Bakr, A. K. Demeler, B. I. Hernandez Uribe, N. Bhattarai, and R. L. Whetten. Characterization of size, anisotropy, and density heterogeneity of nanoparticles by sedimentation velocity. *Anal. Chem.*, 86(15):7688–7695, 2014.

[42] E. E. Lees, M. J. Gunzburg, T. L. Nguyen, G. J. Howlett, J. Rothacker, E. C. Nice, A. H. A. Clayton, and P. Mulvaney. Experimental determination of quantum dot size distributions, ligand packing densities, and bioconjugation using analytical ultracentrifugation. *Nano Lett.*, 8(9):2883–2890, 2008.

[43] M. Cappelezzo, C. A. Capellari, S. H. Pezzin, and L. A. F. Coelho. Stokes-Einstein relation for pure simple fluids. *J. Chem. Phys.*, 126(22):224516, 2007.

Chapter 3

Determination of gold nanoparticle sizes by the new Stokes-Einstein relation

3.1 Abstract

Sub-10 nm nanoparticles find promising applications in research and industry, however, it is still a challenge to determine the size accurately. Size predicted by the Stokes-Einstein relation for the nanoparticles was found about twice the structural size. Here, we report size determination of more realistic model nanoparticles, which are gold nanoparticles with ligands in aqueous liquids, than those presented in Chapter 2, by the new Stokes-Einstein relation. The new theory is obtained by allowing increases in local viscosity of solvent. Both atomistic simulation data and experimental data on the grafted nanoparticles are discussed in this chapter. We present that the structural sizes of simulated and experimental nanoparticles are predicted successfully by the new theory. The increased viscosity assumed for the new theory is estimated and confirmed independently by persistence times of solvent particles near the grafted nanoparticles. Effect of the ligands on the viscosity is further investigated by the number density profiles of atoms. Data suggests that the viscosity of solvent near the grafted nanoparticles is 2$\sim$3 times of the viscosity of bulk solvent. The ligands are found to strengthen the deviation of Stokes-Einstein relation by comparisons between the grafted and bare nanoparticles.

3.2 Introduction

Passivated gold nanoparticles (AuNPs), especially the monolayer-protected ultrasmall gold clusters ($\leq$ 2 nm in diameter),[1] are promising for applications in biological imaging,[2, 3] drug delivery,[4, 5] catalyst,[6, 7] optics,[8, 9] and electronics.[10] The corresponding properties, bioactivity, toxicity,[1] catalysis,[11] optical performance and charge transfer,[12] are size dependent. Therefore, an accurate size measurement is highly demanded. Size determination for small clusters is normally performed by sedimentation velocity analytical ultracentrifugation (SV-AUC).[13–15] The sizes, obtained by the SV-AUC, are calculated by the Stokes-Einstein relation (SER) assuming an equivalence between the hydrodynamic radius and the structural radius.[15] However, proteins,[16, 17] dendrimers,[18] CdSe quantum dots[13, 14] and grafted nanoparticles[15, 19, 20] are found diffusing much slower than that predicted by the SER. The SER is a combination of Stokes' law and Einstein relation. Note here what is in question is Stokes' law not the Einstein relation. Thus, modifications are needed for Stokes' law to obtain a new SER.

We have proposed a modified Stokes-Einstein relation by allowing an increase in solvent viscosity near a particle in Stokes flow, and the new theory has been tested by various types of particles in Chapter 2. Note here an increase in the local viscosity is the crucial requirement for the validity of the new Stokes-Einstein relation. It is reported that the local viscosity can be estimated by persistence times,[16] which, however, are difficult to measure by experiments. Hence we attain them from atomistic simulations to examine whether the persistence times of solvent near the ligands grafted AuNPs increase in a similar way with those of simple liquids near the bare nanoparticles or not. As discussed previously in last chapter, the bare nanoparticles do obey the new SER.

The persistence times of water were found to increase near proteins,[16] which are similar in size to AuNPs. This implies possible heterogeneity of solvent near the grafted AuNPs similar to that near the proteins. Therefore, we hypothesize here that there was an increased local viscosity of water near the grafted AuNPs, similar to that near the bare NPs presented in Chapter 2. The core of grafted gold nanoparticles could induce deviation of Stokes' law, according to our previous research on the bare nanoparticles.[21] Although we found that the ligands are not the source for the deviation from Stokes' law, they may still influence the local dynamics of solvent in a similar way with molecules possessing ligand-like structures, such as proteins and dendrimers. Increases in local viscosity of water around proteins have been revealed,[16] and we also detected a similar dynamic heterogeneity of solvent near model dendrimers in our earlier work.[21] We thus expect to see an increase in local viscosity of water near the AuNPs considering influences from both cores and ligands. The increase in local viscosity could make the application of modified Stokes' law to the AuNPs possible.

If the local viscosity of solvent near an AuNP is higher than that of the bulk solvent, the persistence times of solvent will also be higher.[16] Thus if the new Stokes-Einstein relation stands, we expect to observe higher persistence times.[16] The persistence time distributions may be influenced by ligand conformations as the size of nanoparticle varies. We therefore simulate various sizes of AuNPs with alkanethiol ligands in water. For the simulated AuNPs, we can directly calculate the persistence time distributions of water to detect any changes in the local viscosity and explore the validity of the new Stokes-Einstein relation.

In the following sections, we describe methods of molecular dynamics simulation as well as structures of the grafted and bare nanoparticles. Then we represent the persistence time theory for calculation of the local viscosities. The local viscosity of water near the grafted AuNPs is then discussed in comparison with that near the bare nanoparticles. In order to

further explore the role of ligands in the changes in local viscosity, discussion on conformations of the ligands is presented. We finally predict the sizes of grafted nanoparticles from simulations and experiments[2, 15, 22] using the new Stokes-Einstein relation. These results are discussed with a view to improving the size determination for nanoparticles up to 10 nm.

3.3 Simulation methods

3.3.1 Description of grafted gold nanoparticle models

Gold nanoparticles grafted with alkanethiol ligands have been modeled as shown in Figure 3.1. The cores composed of gold atoms are constructed from face-centered lattice.[23] Every other gold atoms on the surface of the rigid cores are selected for attaching a single ligand chain. The alkanethiol ligands (see Figure 3.2) are composed of $-SR-$ with R=$C_{12}H_{24}$ and a terminal group $-NH_3^+$. The ligands are presented by united atom model that represents a CH_2 group as a single united-atom.[20] Various sizes of AuNPs are simulated by varying the number of gold atoms in the core, including 16, 44, 80 and 140. They are close to the core nuclearities reported by both experiments[24, 25] and simulations.[26–28] We present them as formulas of $Au_{16}(SRNH_3^+)_7$, $Au_{44}(SRNH_3^+)_{19}$, $Au_{80}(SRNH_3^+)_{31}$ and $Au_{140}(SRNH_3^+)_{47}$, respectively. They are named as AuNP-x, where x stands for the number of gold atoms in the core.

Each AuNP with ligands was solvated in a water box with 5000 - 30000 water molecules under periodic boundary conditions. Then Cl^- ions were put inside the box to neutralize positive charges on the ligands. The water molecules were described by the TIP3P model. It was tested that this water model gives correct dynamics of methane.[29] Therefore it is capable of providing the correct results in this work. Partial charges, calculated from the work of Akola,[20] were put on the gold atoms on the surface at the base of each ligand. The

dimensions of simulation boxes range from 40 $\times$ 40 $\times$ 40 $\AA$ to 70 $\times$ 70 $\times$ 70 $\AA$ for the sake of time optimization. We have confirmed that the water density is consistent with that reported in the literature.[30]

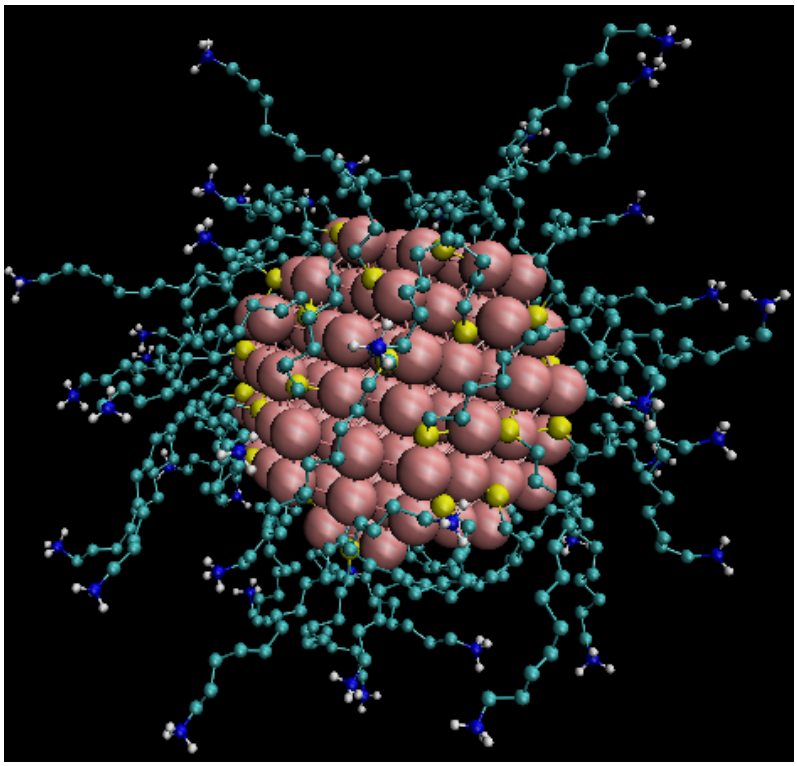

Figure 3.1: Snapshot of a gold nanoparticle grafted by alkanethiol chains with positively charged terminal group $Au_{140}(SC_{12}H_{24})_{47}NH_3^+$, where the Au atoms are represented in ochre, S in yellow, C in cyan, N in blue and H in white.

Constant structures of the gold cores were kept by the equilibrium distance between two atoms and spring constants. The bond length of Au-Au is 3.341 giving a diameter of the AuNPs close to that reported in previous studies.[20, 31] We checked that the bond length is constant during all time frames. Other bond lengths are $d_{Au-S} = 2.45$ $\AA$, $d_{C-S} = 1.83$ $\AA$, $d_{C-C} = 1.53$ $\AA$, $d_{C-N} = 1.47$ $\AA$ and $d_{H-N} = 1.01$ $\AA$. The internal bending energies are k_{111°(C-C-C) = 55.25 $kcal\ mol^{-1}\ rad^{-2}$, k_{100°(Au-S-C) = 55.25 $kcal\ mol^{-1}\ rad^{-2}$, k_{113°(S-C-C) = 55.25 $kcal\ mol^{-1}\ rad^{-2}$, $k_{109.5^\circ}$(H-N-C) = 45.21 $kcal\ mol^{-1}\ rad^{-2}$, $k_{109.5^\circ}$(H-N-H)

= 40.18 $kcal\ mol^{-1}\ rad^{-2}$ and $k_{109.5^\circ}$(N-C-C) = 55.25 $kcal\ mol^{-1}\ rad^{-2}$. The non-bonded atoms force fields are given by the Lennard-Jones potentials. The energy parameters (ϵ) and length parameters (σ) are listed in Table 3.1 taken from the works of Hautman,[32] Ghorai[33] and Heinz.[34]

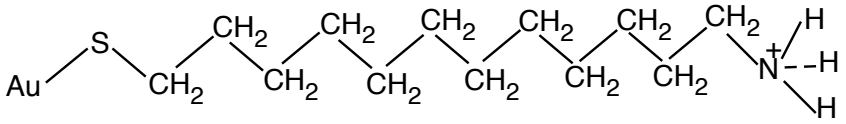

Figure 3.2: Schematic showing an alkanethiol chain with positively charged terminal group. The CH_2 groups are described by the united atom model. A single ligand was attached to each of the selected surface Au atoms.

Table 3.1: Parameters used in the Lennard-Jones potentials.

	ϵ/(Kcal mol^{-1})	σ/Å
Au	-5.290	2.951
CH_2	-0.118	3.905
S	-0.470	4.400
N	-0.200	3.700
H	-0.016	1.049
Na	-0.047	2.727
Cl	-0.150	4.540

All simulations were performed using the NAMD package.[35] Simulations were run for 10 ns for the energy minimization and equilibration of each system. Potential energy of the grafted AuNP/water systems and the ligand structures of AuNPs, characterized by the gyration radius R_g, have been checked to converge well after the equilibrium steps as shown in Figure A3.1 in the Appendix. The production simulations over 100 ns in NPT ensembles were then performed to ensure diffusive behaviours of the grafted AuNPs. We then performed a short simulation of 80 ps in NVT ensembles starting at ∼80 ns, with atomic trajectories stored every 40 fs for the analysis of local viscosities. We collected the data of persistence times at ∼80 ns for the smallest grafted AuNP and at ∼100 ns for larger ones.

Furthermore, we have run the simulations over 200 ns for the largest one and obtained the same potential energy, ligands structures and persistence times as we reported here. We thus ensure that the equilibrium state has been reached and the ligands have relaxed well when the persistence times are calculated.

The cutoff for the force fields calculation is 12 Å and all bonds are kept rigid with a time step of 2 fs. The Particle Mesh Ewald sum is applied to the calculation of full-system electrostatic interactions with a grid size of 1 Å. The temperature of 310 K is controlled by langevin dynamics with a damping coefficient of 5 ps^{-1} for the NVT ensembles. Langevin piston is used to maintain the system pressure to be 1.013 bar, with the oscillation time constant of 100 fs and damping time constant of 50 fs for the NPT ensembles.

3.3.2 Description of bare nanoparticle models

A sequence of bare composite nanoparticles without ligands on the surface were also simulated. The particles were constructed by selecting atoms in a cubically close-packed lattice within a radial distance of a central coordinate. The atoms interact with each other by rigid bonds. The solvent in which the bare nanoparticles diffuse is simulated by the Lennard-Jones liquids. The simulations were carried out in reduced units. Refer to Simulation methods section in Chapter 2 for more details of the description of bare composite nanoparticle models. Comparisons between the passivated gold nanoparticles and bare nanoparticles reveal information of the role of ligands in deviation of the Stokes-Einstein relation.

3.3.3 Localized viscosity estimated by persistence time

As presented in Chapter 2, two time intervals, the persistence time, t_p, and the exchange time, t_x, can be extracted from the motions of solvent particles, which are regarded as a

Continuous Time Random Walk.[16, 36] Persistence time is the waiting time from a random start until the next exchange event. Note here an exchange event happens when a particle moves a fixed distance (jump length) from its initial position. Exchange time is the waiting time between two exchange events. The persistence and exchange times are reported to be able to estimate local viscosity and local diffusivity, respectively. We only focus on the persistence times in this chapter, which are proportional to the local viscosities,

$$\eta(r) \propto kT\langle t_p \rangle_r, \tag{3.1}$$

where $\langle \cdot \rangle_r$ is the average over solvent particles initially at position r with the centre of mass (COM) of a diffusing nanoparticle being the origin. We assumed that the viscosity of solvent near a nanoparticle increases for the new Stokes-Einstein relation. In order to test the validity of the new theory using more realistic systems than the systems modeled without atom details in our earlier work, here we calculate the persistence times of water to estimate the local viscosities near the ligands grafted gold nanoparticles.

The persistence time may be regarded as a mean first passage time, which is the time taken by a particle to reach a given distance from its start for the first time.[37–40] We chose this distance to be 3 Å, the diameter of a water molecule,[41] as justified in the literature.[16] We calculated the coordinate of COM for each water molecule from the stored molecule dynamics (MD) coordinates. It is used to represent the position of a water molecule for the calculation of t_p presented in the following sections.

We perform the similar procedures with those in our previous work to calculate the persistence times. We divide the surrounding water region into spherical bins with the COM of grafted AuNPs being the center of spheres. The persistence time of all water molecules

in each bin and each time frame is then calculated. We take two steps to calculate the persistence time $\langle t_p \rangle$ at a certain distance to the COM of the ligands grafted AuNPs. Firstly, we average the persistence times of water molecules in each bin of a particular time frame. Secondly, the average of persistence times for a bin over all time frames is performed. The methods we use to average the persistence times for the grafted AuNP systems simulated by the atomistic models are the same as those for the bare NPs systems presented in Chapter 2 in order to be comparable.

For a single configuration (time frame) sampled from a MD trajectory, we calculate the harmonic mean of persistence times of water molecules in each bin,

$$\langle t_p \rangle_{r,f} = \frac{N_\mathrm{r}}{\sum_{i=1}^{N_\mathrm{r}} \frac{1}{t_p^i}}, \tag{3.2}$$

where f denotes the fth configuration sampled from a simulation trajectory, i denotes the ith water molecule in the bin at distance r from the COM of the AuNP, and N_r is the total number of the water molecules inside the bin. We then average the time intervals across all configurations by both arithmetic mean and harmonic mean,

$$\langle t_p \rangle_r^{arith} = \frac{1}{N_\mathrm{f}} \sum_{f=1}^{N_\mathrm{f}} \langle t_p \rangle_{r,f}, \tag{3.3}$$

and,

$$\langle t_p \rangle_r^{har} = \frac{N_\mathrm{f}}{\sum_{f=1}^{N_\mathrm{f}} \frac{1}{\langle t_p \rangle_{r,f}}}, \tag{3.4}$$

where N_f is the total number of the configurations. Note here N_f configurations mean N_f conformations of each nanoparticle. We calculated the average persistence times over 2000 conformational samples for each nanoparticle in this study. The local viscosities are then

estimated from these averaged local persistence times.

3.3.4 Size of grafted and bare nanoparticles

Two structural sizes of grafted AuNPs are calculated from the simulated trajectories. One is the radius of the core, and the other is the radius of the core together with the alkanethiol ligands. They are calculated as the distance between the center of mass of the gold core and the outermost atoms of the core and ligands, respectively.[20] The distance of each atom to the center of mass of the core is calculated per time frame and then all the obtained distances are averaged over all time frames. The sizes are calculated to compare with the position where the changes of local viscosities would happen, and to attain a clear picture of the role of ligands in the local dynamics. The structural size of the bare NPs is obtained by scaling sizes in reduced units calculated in Chapter 2.

In order to test the Stokes-Einstein relation, we further calculate the hydrodynamic radius of the grafted AuNPs using,

$$r_h = \frac{k_B T}{6\pi\eta_0 D}, \tag{3.5}$$

where r_h is the hydrodynamic radius, k_B is the Boltzmann's constant, T is the absolute temperature, η_0 is the shear viscosity of pure solvent and D is the diffusion coefficient of AuNPs. The diffusion coefficient of the grafted AuNPs is calculated by using the Einstein relation from simulated trajectories,

$$D_0 = \lim_{t\to\infty} \frac{1}{6t} \langle [\vec{r}(t) - \vec{r}(0)]^2 \rangle, \tag{3.6}$$

where $\vec{r}$ is the position vector and $\langle [\vec{r}(t) - \vec{r}(0)]^2 \rangle$ is the mean-squared displacement (MSD). The MSD is fitted linearly as a function of time t, and then the fitted slope is divided by six in order to calculate D_0. However, Yeh and Hummer[42] reported that D_0 underestimates the

true diffusion coefficient for systems involving long-range interactions. The reason is that the infinite time cannot be truly reached and thus effects of finite cubic size of a simulation box become evident. They then proposed a correction to the diffusion coefficient calculated from the molecular dynamic simulations to calculate the true diffusion coefficient D,

$$D = D_0 + \frac{\xi k_B T}{6\pi\eta_0 L}, \tag{3.7}$$

where $\xi \approx 2.837297$ is a constant and L is the length of the simulation box. We have carried out the same correction to the diffusion coefficient of the simulated AuNPs in water to calculate r_h. We then plot the calculated r_h as a function of their structural size to test the validity of SER, in comparison with the simulated bare NPs. The r_h of the bare NPs in Lennard-Jones liquids, only including short-range interactions, is also calculated from the Stokes-Einstein relation but with D calculated by the Green-Kubo expression,

$$D = \frac{1}{3}\int_0^\infty \langle \mathbf{v}(t) \cdot \mathbf{v}(0) \rangle \, \mathrm{d}t, \tag{3.8}$$

where the velocity correlation function $C_v = \langle \mathbf{v}(t) \cdot \mathbf{v}(0) \rangle$ has decayed to zero and the integration of the velocity correlation functions has converged well within the simulation time.

3.3.5 Calculation of number density of atoms

In order to further investigate the role of ligands in the local viscosity of solvent, we analyze conformations of the ligands. The atom number density of the ligands is calculated as a function of the radial distance from the center of mass of the gold cores. Atoms of sulfur, carbon, nitrogen and oxygen are considered in this study. The number of a single type atom in a shell around the core with a width of Δr is counted, and then the atom number is

divided by the volume of the shell to obtain the atom densities,

$$\rho = \frac{N}{\frac{4}{3}\pi(r_2^3 - r_1^3)}, \tag{3.9}$$

where ρ is the number density of atoms, N is the atoms number in the shell of $\Delta = (r_2 - r_1)$, and r denotes the distance between the atom and the center of mass $\vec{R}_{cm}$. The $\vec{R}_{cm}$ was calculated as the number average of all position vectors,

$$\vec{R}_{cm} = \frac{1}{M}\sum_{j=1}^{M}\vec{R}_j, \tag{3.10}$$

where M is the total atoms number in the core of nanoparticles, j denotes the jth atom and $\vec{R}_j$ is the position vector of atom j.

The number densities obtained in all simulated time frames are then averaged with samples stored every 10 ps. The conformation of ligands is investigated to explore the contribution of different atoms to the local viscosity.

3.4 Results and discussion

3.4.1 Local viscosity estimated by persistence times

We simulate gold nanoparticles with alkanethiol chains in water by atomistic simulations as described above. The local viscosity used to verify the assumption for the new Stokes-Einstein relation is estimated by the persistence times. We observe a similarity between the local viscosities of solvent around the grafted AuNPs and those around the bare NPs (see Figure 3.3). This implies that the viscosity given by the simple models presented in Chapter 2 is reasonably realistic.

Both arithmetic mean and harmonic mean are used to locally average the persistence times of water molecules around the grafted gold NPs as plotted in Figure 3.3. The persistence time of bulk water at 310 K is approximately 4 ps, in agreement with that of water in the lipid bilayer system.[16] Both of the two types of persistence time, calculated by the two types of average over multiple configurations, increase near the ligands grafted gold nanoparticles of various sizes. As a comparison, the persistence time distributions of solvent near the bare nanoparticles were also plotted in Figure 3.3. The increasing pattern in t_p to smaller r near the grafted AuNPs, seen from the shape of curves, is similar as that near the NPs without attached ligands or oligomers on the surface. It indicates a similar deviation from the traditional Stokes-Einstein relation for the two types of nanoparticles according to the mechanism we proposed for the breakdown of Stokes' law. If we observe a similar deviation, it would be confirmed that the deviation is caused by the solvent dynamic heterogeneity regardless of the surface structures. This is crucial for the size determination of a wide range of small particles by using the modified Stokes-Einstein relation. We will examine the extent of deviation from the SER for the grafted and bare NPs presented by the following discussions.

Table 3.2: Structural radius of the cores of grafted AuNPs, total radius of the AuNPs with ligands and structural radius of the bare NPs marked by dashed and solid lines in Figure 3.3 .

	$R_{core}/\mathring{A}$	$R_{AuNP}/\mathring{A}$		$R_{bare}/\mathring{A}$
AuNP-16	3.9	11.9	bare NP 1	4.4
AuNP-44	6.1	17.1	bare NP 2	6.0
AuNP-80	7.7	19.5	bare NP 3	7.6
AuNP-140	9.1	22.6	bare NP 4	9.2

The ratios of the maximum local viscosity of water near the grafted AuNPs to the viscosity of bulk water given by the arithmetic and harmonic average are $\sim$3 and $\sim$2, respectively.

The smaller ratio given by the harmonic mean results from less weight given to the large persistence times. Here both of the two types of average reveal increases in the persistence times. Neither is clearly superior. They contain different information. The increase in persistence times only weakly depends on the size of nanoparticles, which agrees with that for the bare nanoparticles. The effect of increases in viscosity must vanish as the AuNPs grow in size because the SER is valid for macroscopic particles.

The position where the changes in persistence time happens near the grafted AuNPs is investigated here for a more clear picture of the origin of increase in the local viscosity. The persistence times increase between the two dashed lines in each plot in Figure 3.3. The dashed lines are the outermost boundary of the core and ligands, respectively. It indicates that the water molecules penetrate into the ligands. The interactions between the ligands and water affect the dynamics of water. The t_p starts to increase near the outside border of grafted AuNPs, referred as R_{AuNP}, to smaller r. Then it increases sharply and reaches to the maximum near the inner border of the grafted AuNP (R_{core}). It suggests that the ligands of grafted AuNPs influence the dynamics of water by slowing down the diffusive motions. The results for the bare nanoparticles suggest that the core also has effect on slowing down the dynamics of surrounding solvent. Taking the results together, we conjecture that both dense gold cores and ligands contribute to the increase in the local viscosity.

In order to further explore the role of ligands in local dynamics of solvent near a diffusing nanoaprticle, we compare the persistence time distributions of water near the grafted gold nanoparticles to those of solvent near the bare nanoparticles. In spite of the similarity between them mentioned above, there are still dissimilarities between the persistence times of solvent near the two types of nanoparticles, including the magnitude, the position and width of peak of the plots, which might imply effects of ligands on the local dynamics.

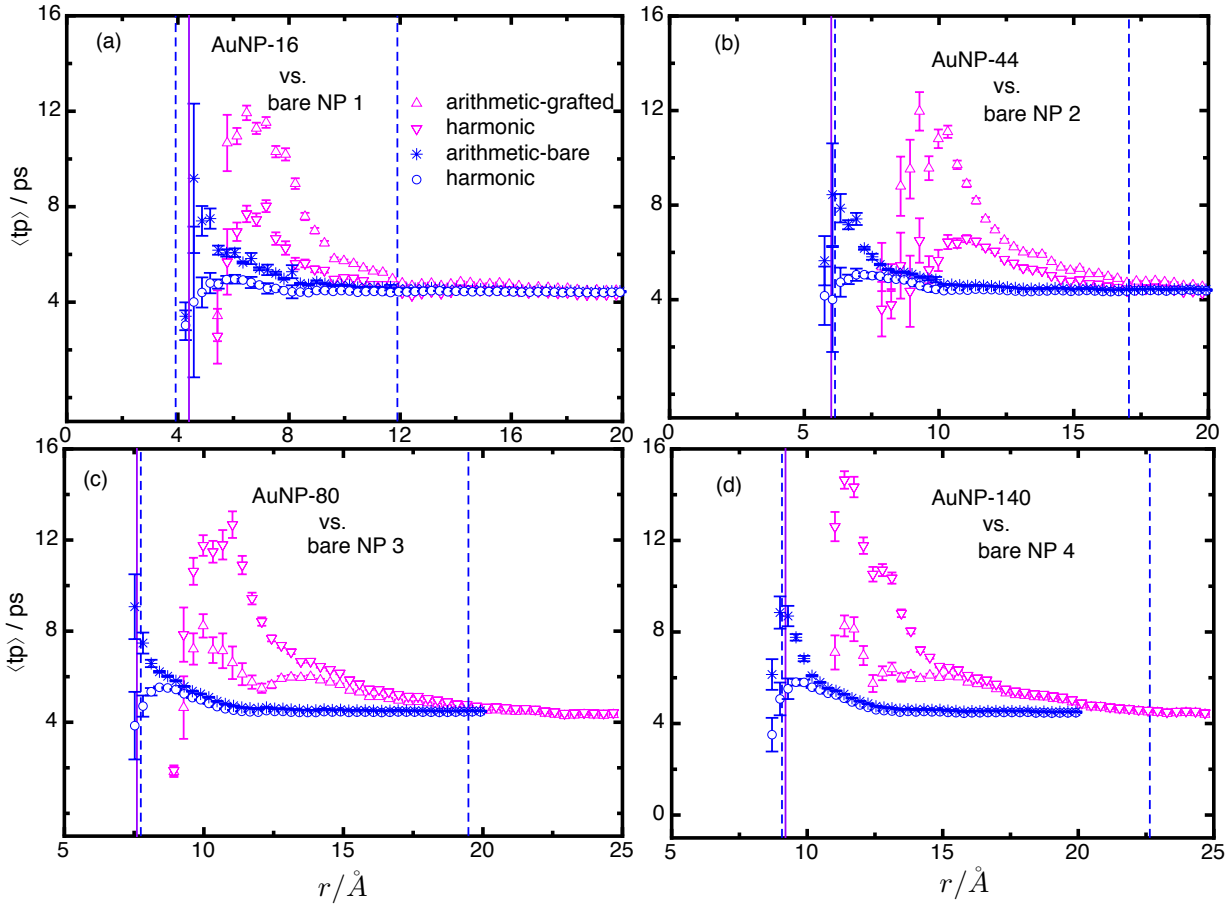

Figure 3.3: Persistence time t_p as a function of r near the AuNPs with alkanethiol ligands and the bare NPs. r is the distance to the COM of gold cores or the bare NPs. The length and time in reduced units for the bare NPs were converted to Å and ps, respectively, by multiplying the length parameter $\sigma = 2.95$ $\mathring{A}$ which is the diameter of a gold atom, and by multiplying the ratio of the t_p of bulk water to simple liquids 13.3 ps. Each grafted AuNP is compared to a bare nanoparticle of the closest size. The two dashed lines in each plot are the structural radii of the gold cores (R_{core}) and the total radii including the ligands (R_{AuNP}), respectively. The solid lines are the structural radii of the bare NPs (R_{bare}). The radii of both the grafted AuNPs and bare NPs are listed in Table 3.2. The persistence times of solvent particles inside each circular bin were averaged by a harmonic mean. The $\langle t_p \rangle$ obtained from multiple configurations were averaged by both arithmetic mean and harmonic mean. The 'AuNP-x' stands for x gold atoms existing in the gold core (see above for details). The 'bare NP x' stands for the xth bare NP.

We compare the grafted and bare NPs. Each pair of NPs has approximately the same structural radius of the cores. In order to make the comparison meaningful, the length and

time in reduced units for the bare NPs were converted to Å and ps, respectively. The length parameter is 2.95 $\mathring{A}$ which is the diameter of a gold atom and the persistence time of bulk simple liquids is 4.4 ps which is the persistence time of the bulk water. After the units conversion of the two parameters, the persistence time distributions of solvent near the bare NPs were plotted in Figure 3.3.

Four pairs of NPs are compared, which are AuNP-16 vs. bare NP 1, AuNP-44 vs. bare NP 2, AuNP-80 vs. bare NP 3 and AuNP-140 vs. bare NP 4 as shown in Figure 3.3 (a), (b), (c) and (d), respectively. The structural sizes of the cores for each pair are comparable as shown in Table 3.2. The ratio of the maximum local viscosity to the bulk viscosity of solvent near the grafted AuNPs is ∼3 by arithmetic mean, and ∼2 by harmonic mean over multiple configurations. Both are larger than those near the bare NPs which are ∼2 and ∼1.3, respectively. This indicates that the ligands do influence the mobility of solvent molecules inside them, when the packing density is sufficient, just as demonstrated by the dendrimers[21] and proteins.[16] That the maximum local viscosity of solvent near the grafted AuNPs is larger than that near the bare NPs results from that the ligands produce a more rough interactive region between the grated NP and water, hindering the water from escaping, than that between the bare NP and Lennard-Jones liquid.[43]

The t_p curves are pushed further away from the surface of grafted AuNPs than that from the surface of the bare NPs. A distance, about 3 Å in the range of diameter of an atom, exists between the grafted AuNPs surface and the boundary of water. However, the simple liquids seem to penetrate into the bare NPs indicated by the solid lines especially for the largest one (bare NP 4 in Figure 3.3 (d)). It is because of the unideal spherical shape of the NPs, which are developed from a face-centered box. There are defects on the surface which are hole-like areas inside the ideal spherical sizes of the bare NPs. The solvent particles can get

access to these areas. The possibility of the defects is higher for the large bare NPs than the small bare NPs because of the larger surface area. While the water cannot get access to the inside of the ideal spherical size of the grafted gold cores, indicating that the high packing density of the atoms of the ligands on the surface of cores offsets the defects and makes the hole-like areas hard to be reached.

It is concluded that apart from the dense cores, the ligands also contribute to the increase in the local viscosity. The ligands strengthen the dynamic heterogeneity of water near the passivated gold nanoparticles seen from the above comparisons between the persistence time distributions of solvent near the grafted gold NPs and bare NPs. We therefore believe that the ligands and dense cores jointly contribute to the deviation of Stokes-Einstein relation.

3.4.2 Density profiles of grafted AuNP/water systems

We continue to investigate structures of the AuNP/water systems for a picture of effects of atoms of the ligands on the local viscosity. We present structural details of the ligands and water around the simulated AuNPs with ligands. The structural details are presented by density profiles of various atom species as shown in Figure 3.4 and 3.5. They were measured as a function of the radial distance from the center of mass of the gold cores at T=310 K. We emphasize possible effects of the structures on the persistence times of water indicated by the density profiles. Here we assume that the atoms affect persistence times most strongly in a small region around their positions.

The oxygen density profiles slightly overlap with those of the sulfur atoms for all of the four grafted AuNPs as shown in Figure 3.4 and 3.5, indicating that the water molecules penetrate into the ligands but only slightly into the sulfur atoms. We can also see it from the corresponding persistence time profiles. Existence of the sulfur atoms and interaction

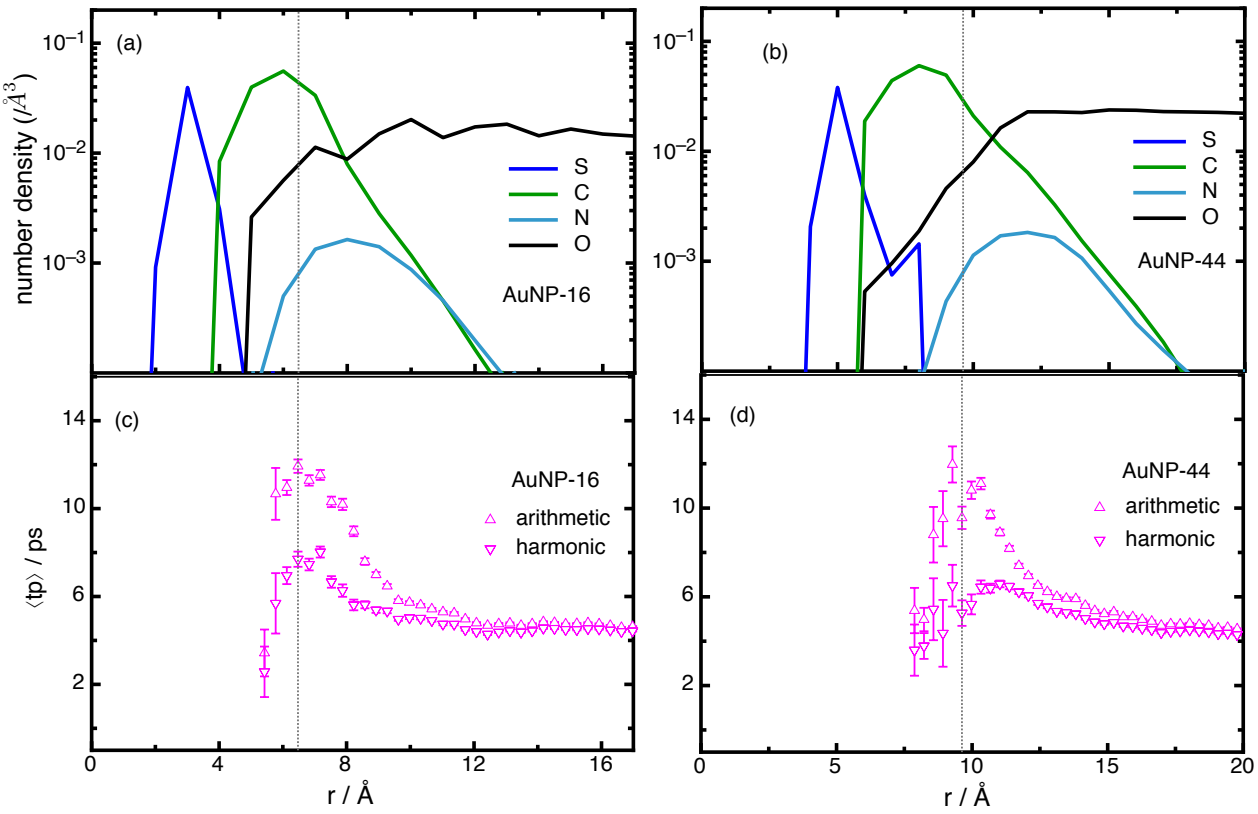

Figure 3.4: Radial density profiles of atoms S, C, N belonging to the alkanethiol ligands of the simulated AuNP-16 (a) and AuNP-44 (b) and the corresponding O in water molecules for each system; and persistence times from both arithmetic and harmonic average for the AuNP-16 (c) and AuNP-44 (d) systems. The dotted lines mark the positions of the peaks of the $\langle t_p \rangle$ plots. r is the distance to the COM of the gold core. The 'AuNP-x' stands for a gold NP with x core atoms.

bewteen the sulfur atoms and the water molecules may explain the further distance between the peaks of persistence time profiles and surface of cores for the grafted gold nanoparticles than that for the bare nanoparticles as shown in Firgure 3.3.

The alkane carbon profiles show the maximum density alongside the sulfur profiles, closely mirroring those of the persistence times near the four AuNPs. This can be seen from the dotted lines in Figure 3.4 and 3.5. Meanwhile, the oxygen profiles partly overlap with the carbon profiles, and decline from the bulk density as approaching to the maximum point

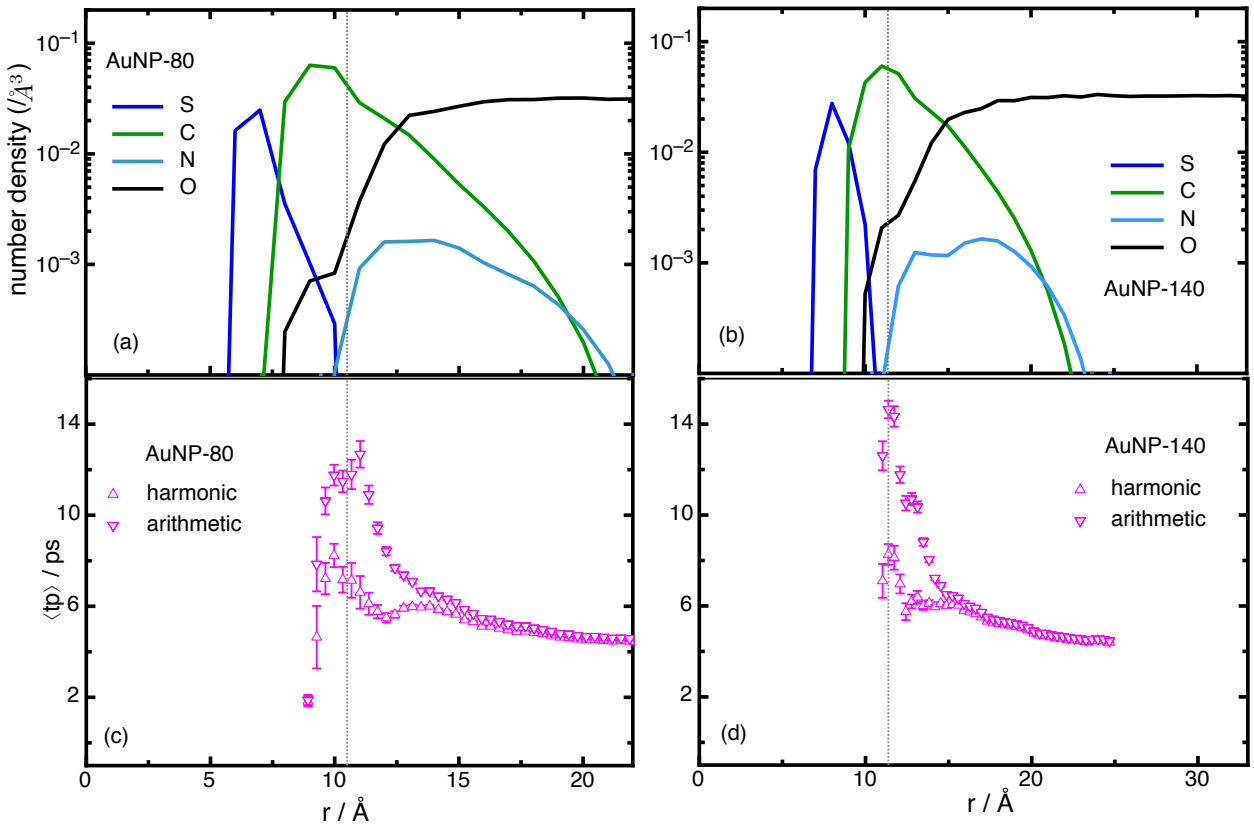

Figure 3.5: Radial density profiles for atoms of S, C, N belonging to alkanethiol ligands of the simulated AuNP-80 (a) and AuNP-140 (b) and the corresponding O representing water for each system; and persistence times from both arithmetic and harmonic average for the AuNP-80 (c) and AuNP-140 (d) systems. The dotted lines mark the positions of the peaks of the $\langle t_p \rangle$ plots. r is the distance to the COM of the gold core. The 'AuNP-x' stands for a gold NP with x core atoms.

of the carbon profiles, in agreement with the published results.[20, 44] These phenomena result from interactions between the alkane groups and water molecules. The comparisons between the atom number density profiles and persistence time profiles suggest that the carbon atoms create a more congesting environment near the gold cores than the peripheral. The congestion hinders the movement of the penetrated water molecules and thus elongates the persistent times near the grafted nanoparticles.

The nitrogen profiles locate near the water interface with broad peaks and low number

density. The persistence time profiles begin to increase as the water molecules penetrate into the $-NH_3^+$ groups, indicating that interactions between the terminal groups and water molecules also contribute to the increase in the local viscosity. The terminal group of the ligands is $-NH_3^+$, which is positively charged and believed to form hydrogen bonds with water.[20] Part of the contribution to the increase in the persistence times might come from the hydrogen bonds.

The above analysis suggests that the ligands studied here contribute to the increase in the local viscosity of water. The increase results from the cooperation of interactions between all atoms of the ligands and water, but the alkane groups dominate the magnitude of the largest increase in the local viscosities of water near the gold NPs based on the assumption of local effects mentioned above. We leave the study on more details of interactions between the ligands and water to the future, due to that the validity of the new Stokes-Einstein relation is not affected by the nature of interactions based on the results for nanoparticles with different structures presented in Chapter 2.

So far the increases in local viscosity near the nanoparticles are detected and estimated by the persistence times. The hypothesis for the new Stokes-Einstein relation is, therefore, independently confirmed. In the following, we apply the new theory to the grafted and bare nanoparticles and examine its validity.

3.4.3 Hydrodynamic and structural size of nanoparticles

A new Stokes-Einstein relation was obtained from solving the Navier-Stokes equations by allowing an increased local viscosity around a particle diffusing in a viscous fluid. The details are given in Chapter 2. The new theory should be used in place of the usual SER for the size measurement of nanoparticles up to 10 nm. Here we only represent the new hydrodynamic

radius solved from the new Stokes-Einstein relation,

$$\hat{r}_{\mathrm{h}} = \left(\frac{kT}{12\pi D\eta_0} - \frac{4\alpha s}{3}\right) + \sqrt{\frac{8}{3}\alpha s^2 + \left(\frac{kT}{12\pi D\eta_0} - \frac{4\alpha s}{3}\right)^2}, \tag{3.11}$$

where $\hat{r}_{\mathrm{h}}$ is the corrected hydrodynamics radius of a particle of arbitrary shape, s is the size of a solvent particle, s = 0.275 nm for water and 0.331 nm for Lennard-Jones liquid, α is the largest surface viscosity increase seen for any particle size, D is the diffusion coefficient of nanoparticles, η_0 is the shear viscosity of pure solvent, T is the absolute temperature and k_B is the Boltzmann constant. Note here since we found that the fitted values of s obtained in Chapter 2 for the composite bare nanoparticles and experimental nanoparticles are close to the diameter of solvent particles instead of the radius. Therefore, we assign diameter of solvent particles to s in this chapter.

Here we apply the new Stokes-Einstein relation to ligands grafted gold nanoaparticles in our simulations and experiments reported in literature. The hydrodynamic radii (r_h) calculated from the traditional Stokes-Einstein relation and structural radii (R) of the grafted AuNPs calculated from the sampled trajectories are plotted in Figure 3.6. The theory curves plotted can be obtained from solving Eq 3.11. Note here the structural radii of the four AuNPs are the size of the gold cores as argued for the size definition of CdSe quantum dots with core-shell structures in Chapter 2. The same procedures were taken for the bare nanoparticles for comparison.

In Figure 3.6(a), we observe that r_h grows faster than the corresponding R of both simulated AuNPs with ligands and bare NPs. This means that the traditional SER fails for the determination of true nanoparticle sizes. The theory curves agree well with the two sets of simulation data. That the theory curve of the ligands grafted AuNPs stays above the

theory curve of the bare NPs indicates smaller diffusion coefficient of the AuNPs than that of the bare NPs with the same size of cores. The comparison suggests that the ligands give contributions to the drag force on the diffusing gold nanoparticles investigated. This agrees with the role of ligands in the local viscosity concluded from the comparison of persistence times between the simulated ligands grafted NPs and bare NPs.

In Figure 3.6(b, c), we continue to apply our theory to experimental AuNPs in water and toluene, respectively. Let s equal the size of the solvent particles listed in Table 3.3 and then fit our new theory to the experimental size data. The fitted values of α, which is the maximum of the increase in viscosity seen for any size of the experimental AuNPs and our simulated AuNPs, are similar (Table 3.3). This is important for applications of the new theory in the future. With the known parameters, we calculate the increases in local viscosity (Δ) using the expression given in Chapter 2 when deriving the new Stokes-Einstein relation,

$$\Delta = 4\alpha \frac{s}{a}\left(1 - \frac{s}{a}\right), \tag{3.12}$$

where a is radius of an idealised spherical particle. We find that the increased local viscosity is consistent with that estimated by the persistence times as appropriate (see Figure A3.2 in the Appendix). Here the local viscosity obtained by the arithmetic average of persistence times is closer to that inferred from our new theory than that by the harmonic average.

Table 3.3: Parameters for the theory curves in Figure 3.6 and 3.7.

	α	s/nm
Simulated AuNPs in water	1.83±0.13	0.275
Simulated bare NPs	1.41±0.11	0.331
Experimental AuNPs in water	1.77±0.21	0.275
Experimental AuNPs in toluene	1.64±0.19	0.500

The simulations agree with experiments as shown by the theory curves in Figure 3.6 (d).

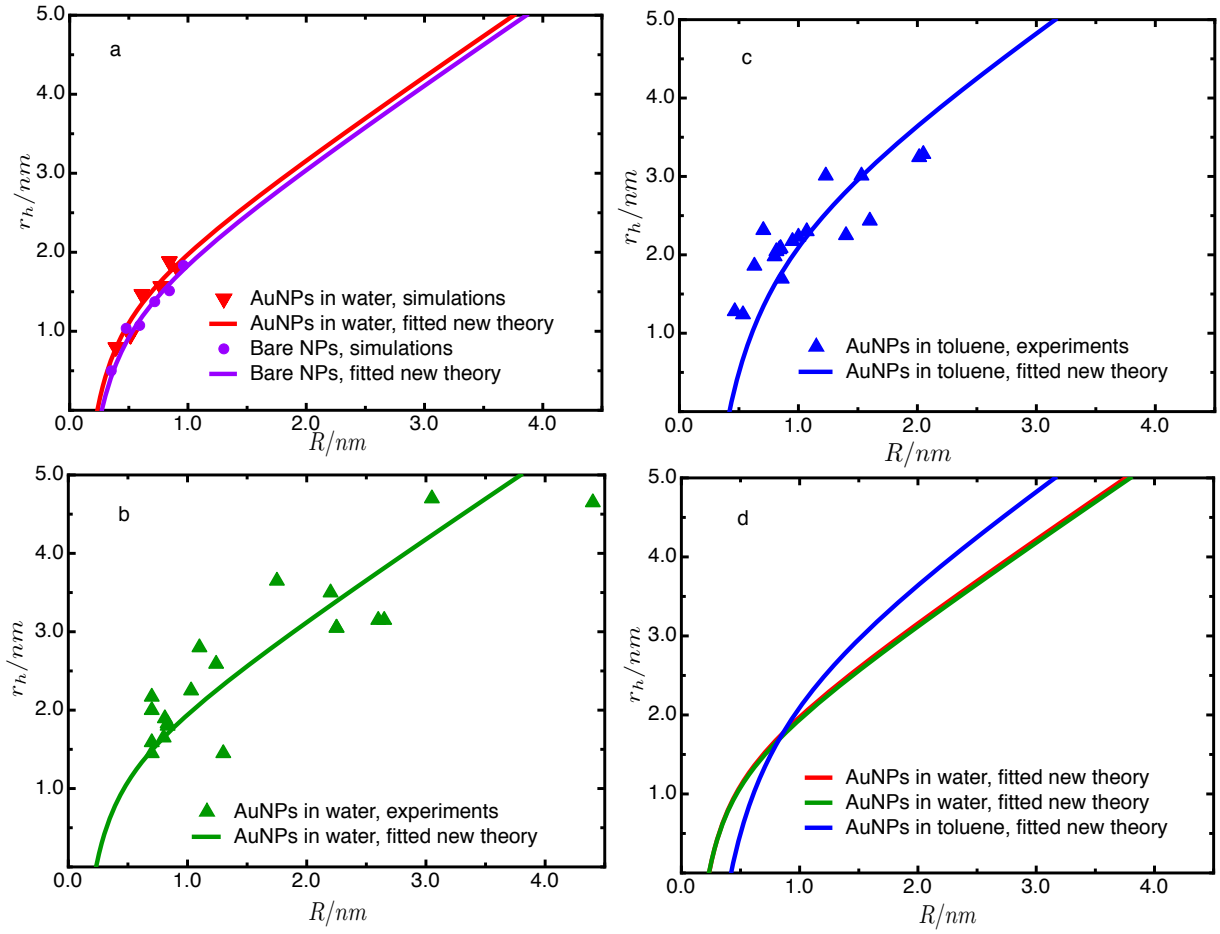

Figure 3.6: Hydrodynamic radius r_h of (a) simulated grafted gold nanoparticles in water and simulated bare nanoparticles in Lennard-Jones liquids and (b) experimental gold nanoparticles in water[2, 22, 45–51] and (c) experimental gold nanoparticles in toluene[52] as a function of the corresponding structural radius R; (d) the fitted theory curves of experimental and simulated AuNPs. The parameters of s and α for the theory curves are listed in Table 3.3.

Furthermore, the applications of the new SER to the AuNPs in water and toluene imply that the mechanism we proposed for the deviation of Stokes-Einstein relation and the new theory could be valid to nanoparticles in various solvents.

The agreement of experimental and simulated data with our new theory for the gold nanoparticles with ligands shown in Figure 3.6 implies that eq 3.11 is able to predict the true size of both the investigated AuNPs with ligands and bare NPs. To be more clear, we plot the

corrected hydrodynamic radii $\hat{r_h}$ in Figure 3.7. The hydrodynamic radii are successfully brought in agreement with the structure radii of both the grafted AuNPs and bare NPs. The experimental data is scattered due to that they are obtained by various research groups. Different equipments and measuring methods used in experiments may result in errors and lead to the data being scatted. The successful correction suggests that the new SER is applicable to the investigated nanoparticles with different surface structures and improves the accuracy of their size measurement.

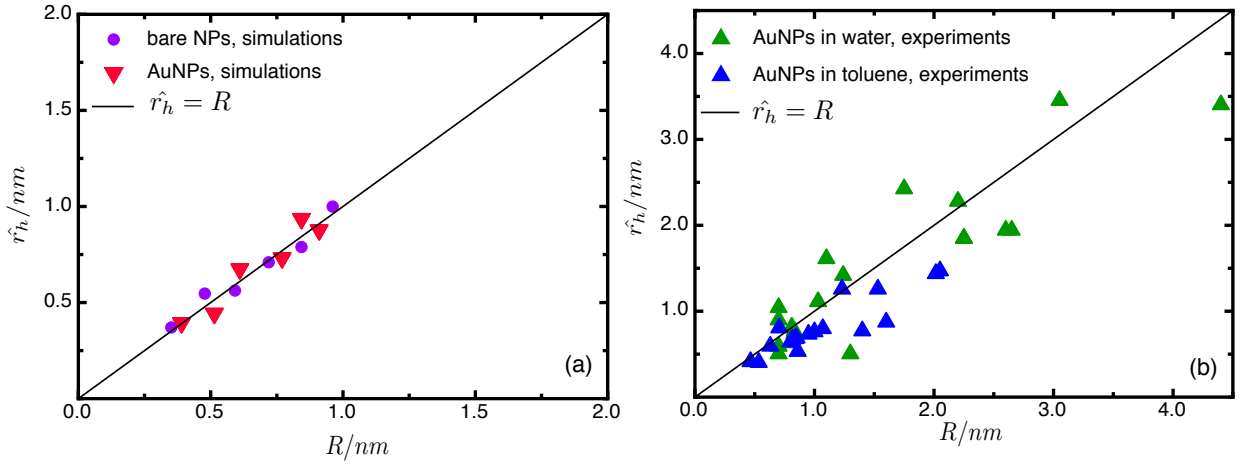

Figure 3.7: Corrected hydrodynamic radii ($\hat{r_h}$) of (a) simulated AuNPs with ligands and bare NPs and (b) experimental AuNPs as a function of the corresponding structural radius R. The $\hat{r_h}$ were calculated by eq 3.11 with parameters of α and s listed in Table 3.3 and the hydrodynamic radii r_h were calculated from the traditional Stokes-Einstein relation.

3.5 Conclusion

We find increases in the persistence times of solvent near the gold nanoparticles with ligands, similar with those near the bare nanoparticles. The results support the hypothesis that an increased local viscosity of solvent exists near the gold nanoparticles with ligands. We also find agreement between the simulations and experiments, between the experiments and theory, and between the simulation and theory. Investigation on the gold nanoparticles

together with the simulations of simple models and experiments of CdSe QDs presented in Chapter 2 suggest that the new SER is sound for size determination of nanoparticles in a few nanometers.

We obtain this conclusion by atomistic simulations of the grafted gold nanoparticles of various sizes, and comparisons between the grafted nanoparticles with the bare nanoparticles. These allow us to directly attain the increased local viscosities by extracting persistence time distributions from individual trajectories of atoms; to detect the role of ligands in this local dynamics by the comparison with the bare nanoparticles; to seek support of effects of ligands on the local viscosities from the density profiles of various atoms species; and to finally find an appropriate consistence between the simulations, experiments and our theory and to predict the sizes of nanoparticles accurately.

The results show similar increasing patters in the local viscosities of solvent near the grafted nanoparticles and bare nanoparticles. The fact that similar dynamic heterogeneity exists near nanoparticles of different structures implies that the validity of the new Stokes-Einstein relation is not sensitive to the surface structures. Thus the new theory could be applied to a wide range of nanoparticles for better size determination.

3.6 Appendix

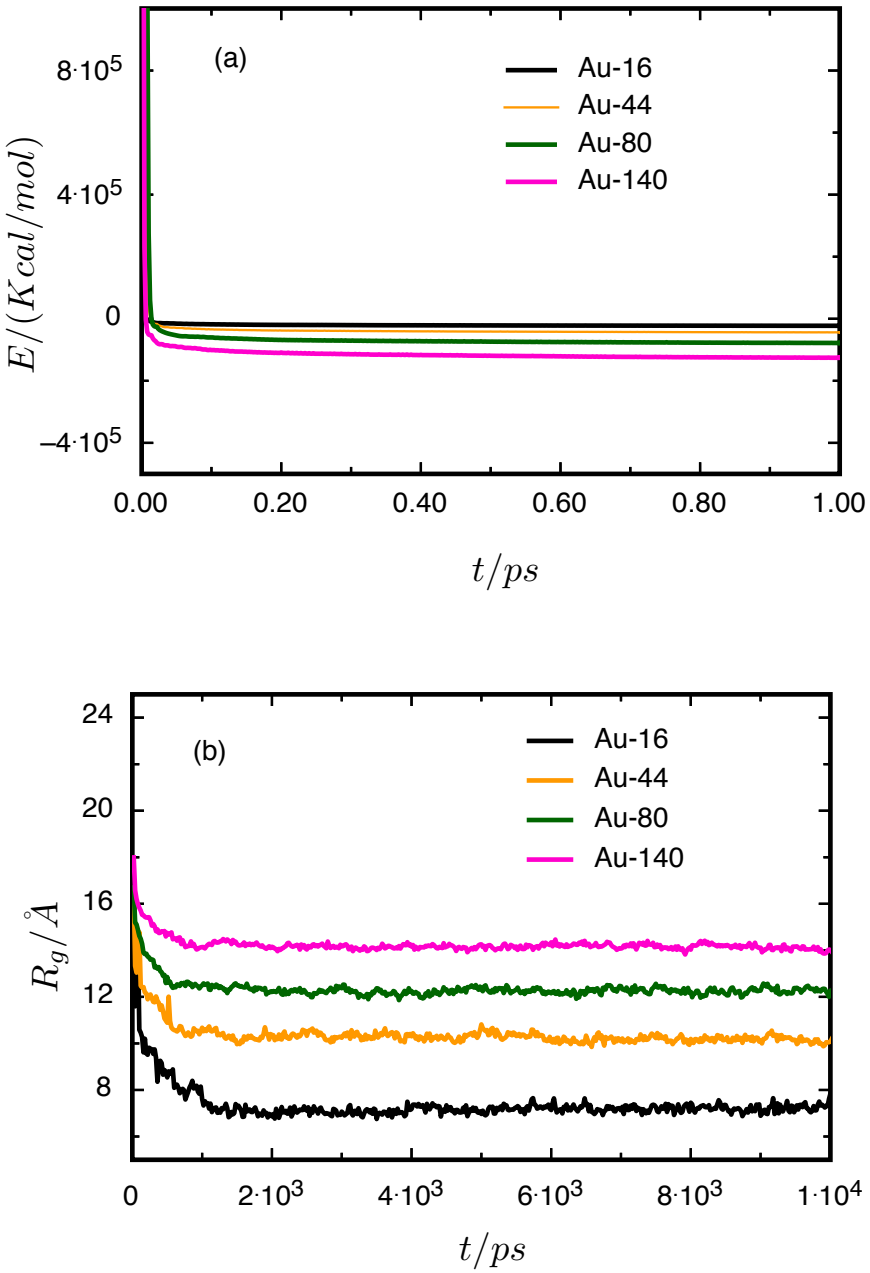

Figure A3.1: (a): Potential energy of gold nanoparticle/water systems; (b): Gyration radius of gold nanoparticles including ligands. The 'AuNP-x' stands for a gold NP with x core atoms. The converge of the potential energy and R_g confirms that the ligands have relaxed well.

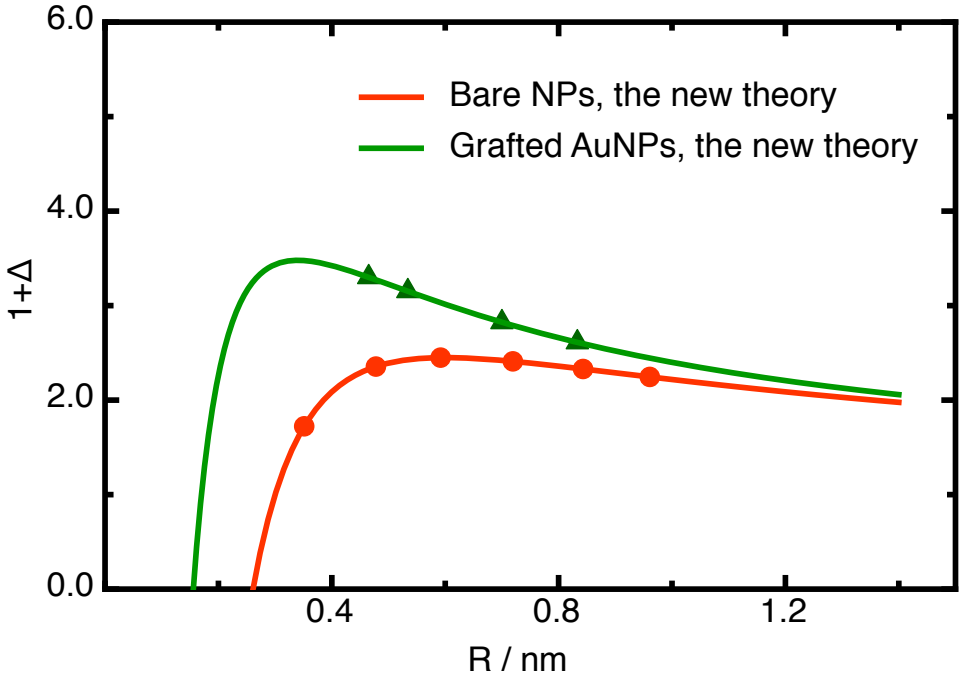

Figure A3.2: Local viscosity of solvent near bare NPs and grafted NPs calculated from the new theory with the fitted values of α and the given values of s in Δ. The green angles and red circles show the local viscosity near the AuNPs and bare NPs investigated from the new theory.

Bibliography

[1] A. Leifert, Y. Pan-Bartnek, U. Simon, and W. Jahnen-Dechent. Molecularly stabilised ultrasmall gold nanoparticles: synthesis, characterization and bioactivity. *Nanoscale*, 5(14):6224–42, 2013.

[2] A. A. Sousa, J. T. Morgan, P. H. Brown, A. Adams, M. P. S. Jayasekara, G. Zhang, C. J. Ackerson, M. J. Kruhlak, and R. D. Leapman. Synthesis, characterization, and direct intracellular imaging of ultrasmall and uniform glutathione-coated gold nanoparticles. *Small*, 8(14):2277–2286, 2012.

[3] C. A. Simpson, A. C. Agrawal, A. Balinski, K. M. Harkness, and D. E. Cliffel. Short-chain PEG mixed monolayer protected gold clusters increase clearance and red blood cell counts. *ACS Nano*, 5(5):3577–3584, 2011.

[4] P. Ghosh, G. Han, M. De, C. K. Kim, and V. M. Rotello. Gold nanoparticles in delivery applications. *Adv. Drug Deliv. Rev.*, 60(11):1307–1315, 2008.

[5] A. Kumar, H. Ma, X. Zhang, K. Huang, S. Jin, J. Liu, T. Wei, W. Cao, G. Zou, and X. Liang. Gold nanoparticles functionalized with therapeutic and targeted peptides for cancer treatment. *Biomaterials*, 33(4):1180–1189, 2012.

[6] Y. Zhu, Z. Wu, C. Gayathri, H. Qian, R. R. Gil, and R. Jin. Exploring stereoselectivity of Au_{25} nanoparticle catalyst for hydrogenation of cyclic ketone. *J. Catal.*, 271(2):155–160, 2010.

[7] A. S. K. Hashmi and G. J. Hutchings. Gold Catalysis. *Angew. Chem. Int. Ed.*, 45(47):7896–7936, 2006.

[8] T. G. Schaaff, M. N. Shafigullin, J. T. Khoury, I. Vezmar, R. L. Whetten, W. G. Cullen, P. N. First, C. Gutiérrez-Wing, J. Ascensio, and M. J. Jose-Yacamán. Isolation

of smaller nanocrystal Au molecules: Robust quantum effects in optical spectra. *J. Phys. Chem. B*, 101(40):7885–7891, 1997.

[9] M. Zhu, C. M. Aikens, F. J. Hollander, G. C. Schatz, and R. Jin. Correlating the crystal structure of a thiol-protected Au_{25} cluster and optical properties. *J. Am. Chem. Soc.*, 130(18):5883–5885, 2008.

[10] D. Adams, L. Brus, C. Chidsey, S. Creager, C. Creutz, C. Kagan, P. Kamat, M. Lieberman, S. Lindsay, R. Marcus, R. Metzger, J. Michel-Beyerle, M .and Miller, M. Newton, D. Rolison, O. Sankey, K. Schanze, J. Yardley, and X. Zhu. Charge transfer on the nanoscale: Current status. *J. Phys. Chem. B*, 107(28):6668–6697, 2003.

[11] A. Mohanty, N. Garg, and R. Jin. A universal approach to the synthesis of noble metal nanodendrites and their catalytic properties. *Angew. Chem. Int. Ed.*, 49(29):4962–4966, 2010.

[12] T. Gregory Schaaff, G. Knight, M. N. Shafigullin, R. F. Borkman, and R. L. Whetten. Isolation and selected properties of a 10.4 kDa gold: Glutathione cluster compound. *J. Phys. Chem. B*, 102(52):10645–10646, 1998.

[13] E. E. Lees, M. J. Gunzburg, T. L. Nguyen, G. J. Howlett, J. Rothacker, E. C. Nice, A. H. A. Clayton, and P. Mulvaney. Experimental determination of quantum dot size distributions, ligand packing densities, and bioconjugation using analytical ultracentrifugation. *Nano Lett.*, 8(9):2883–2890, 2008.

[14] B. Demeler, T. L. Nguyen, G. E. Gorbet, V. Schirf, E. H. Brookes, P. Mulvaney, A. O. El-Ballouli, J. Pan, O. M. Bakr, A. K. Demeler, B. I. Hernandez Uribe, N. Bhattarai, and R. L. Whetten. Characterization of size, anisotropy, and density heterogeneity of nanoparticles by sedimentation velocity. *Anal. Chem.*, 86(15):7688–7695, 2014.

[15] R. P. Carney, J. Y. Kim, H. Qian, R. Jin, H. Mehenni, F. Stellacci, and O. M. Bakr. Determination of nanoparticle size distribution together with density or molecular weight by 2D analytical ultracentrifugation. *Nat. Commun.*, 2(335):1, 2011.

[16] S. Pronk, E. Lindahl, and P. M. Kasson. Dynamic heterogeneity controls diffusion and viscosity near biological interfaces. *Nat. Commun.*, 5(3034):1, 2014.

[17] B. Halle and M. Davidovic. Biomolecular hydration: From water dynamics to hydrodynamics. *Proc. Natl. Acad. Sci. USA*, 100(21):12135–12140, 2003.

[18] P. K. Maiti and B. Bagchi. Diffusion of flexible, charged, nanoscopic molecules in solution: Size and pH dependence for PAMAM dendrimer. *J. Chem. Phys*, 131(21):214901, 2009.

[19] S. Goyal and F. A. Escobedo. Structure and transport properties of polymer grafted nanoparticles. *J. Chem. Phys*, 135(18):184902, 2011.

[20] E. Heikkilä, A. A. Gurtovenko, H. Martinez-Seara, H. Häkkinen, I. Vattulainen, and J. Akola. Atomistic simulations of functional Au_{144} $(SR)_{60}$ gold nanoparticles in aqueous environment. *J. Phys. Chem. C*, 116(17):9805–9815, 2012.

[21] X. Zhang, S. Tran, and A. A. Gray-Weale. The hydrodynamic drag on diffusing nanoparticles for size determination. *J. Phys. Chem. C*, 120(38):21888–21896, 2016.

[22] T. Tominaga, S. Tenma, H. Watanabe, U. Giebel, and G. Schmid. Tracer diffusion of a ligand-stabilized two-shell gold cluster. *Chem. Lett.*, 25(12):1033–1034, 1996.

[23] O. Lee and G. C. Schatz. Molecular dynamics simulation of {DNA}-functionalized gold nanoparticles. *J. Phys. Chem. C*, 113(6):2316–2321, 2009.

[24] R. Balasubramanian, R. Guo, A. J. Mills, and R. W. Murray. Reaction of $Au_{55}(PPh_3)_{12}Cl_6$ with thiols yields thiolate monolayer protected Au_{75} clusters. *J. Am. Chem. Soc.*, 127(22):8126–8132, 2005.

[25] P. J. Krommenhoek, J. Wang, N. Hentz, A. C. Johnston-Peck, K. A. Kozek, G. Kalyuzhny, and J. B. Tracy. Bulky adamantanethiolate and cyclohexanethiolate ligands favor smaller gold nanoparticles with altered discrete sizes. *ACS Nano*, 6(6):4903–4911, 2012.

[26] K. Tay and F. Bresme. Hydrogen bond structure and vibrational spectrum of water at a passivated metal nanoparticle. *J. Mater. Chem.*, 16(20):1956, 2006.

[27] M. Walter, J. Akola, O. Lopez-Acevedo, P. D. Jadzinsky, G. Calero, C. J Ackerson, R. L. Whetten, H. Grönbeck, and H. Häkkinen. A unified view of ligand-protected gold clusters as superatom complexes. *Proc. Natl. Acad. Sci. U.S.A.*, 105(27):9157–62, 2008.

[28] Y. Li, Z. Yang, N. Hu, R. Zhou, and X. Chen. Insights into hydrogen bond dynamics at the interface of the charged monolayer-protected Au nanoparticle from molecular dynamics simulation. *J. Chem. Phys*, 138(18):184703, 2013.

[29] V. K. Michalis, O. A. Moultos, I. N. Tsimpanogiannis, and I. G. Economou. Molecular dynamics simulations of the diffusion coefficients of light n-alkanes in water over a wide range of temperature and pressure. *Fluid Phase Equilib.*, 407:236–242, 2016.

[30] D. Paschek. Temperature dependence of the hydrophobic hydration and interaction of simple solutes: An examination of five popular water models. *J. Chem. Phys*, 120(14):6674, 2004.

[31] O. Lopez-Acevedo, J. Akola, R. L. Whetten, H. Grönbeck, and H. Häkkinen. Structure and bonding in the ubiquitous icosahedral metallic gold cluster $Au_{144}(SR)_{60}$. *J. Phys. Chem. C*, 113(13):5035–5038, 2009.

[32] J. Hautman and M. L Klein. Simulation of a monolayer of alkyl thiol chains. *J. Chem. Phys.*, 91(8):4994–5001, 1989.

[33] P. Kr. Ghorai and S. C. Glotzer. Molecular dynamics simulation study of self-assembled monolayers of alkanethiol surfactants on spherical gold nanoparticles. *J. Phys. Chem. C*, 111(43):15857–15862, 2007.

[34] H. Heinz, R. A. Vaia, B. L. Farmer, and R. R. Naik. Accurate simulation of surfaces and interfaces of face-centered cubic metals using 12-6 and 9-6 Lennard-Jones potentials. *J. Phys. Chem. C*, 112(44):17281–17290, 2008.

[35] L. Kalé, R. Skeel, M. Bhandarkar, R. Brunner, A. Gursoy, N. Krawetz, J. Phillips, A. Shinozaki, K. Varadarajan, and K. Schulten. NAMD2: Greater scalability for parallel molecular dynamics. *J. Comput. Phys.*, 151:283–312, 1999.

[36] Y. Jung, J. P. Garrahan, and D. Chandler. Dynamical exchanges in facilitated models of supercooled liquids. *J. Chem. Phys.*, 123(8):1–11, 2005.

[37] E. W. Montroll and G. H. Weiss. Random walks on lattices. II. *J. Math. Phys.*, 6(2):167, 1965.

[38] E. W. Montroll. Random walks on lattices. III. Calculation of first-passage times with application to exciton trapping on photosynthetic units. *J. Math. Phys.*, 10(4):753, 1969.

[39] P. Reimann, G. J Schmid, and P. Hänggi. Universal equivalence of mean first-passage time and Kramers rate. *Phys. Rev. E*, 60(1):R1–R4, 1999.

[40] L. O. Hedges, L. Maibaum, D. Chandler, and J. P. Garrahan. Decoupling of exchange and persistence times in atomistic models of glass formers. *J. Chem. Phys.*, 127(21):1–4, 2007.

[41] M. M. Teeter. Water structure of a hydrophobic protein at atomic resolution: Pentagon rings of water molecules in crystals of crambin. *Proc. Natl. Acad. Sci. USA*, 81(19):6014–6018, 1984.

[42] I. C. Yeh and G. Hummer. System-size dependence of diffusion coefficients and viscosities from molecular dynamics simulations with periodic boundary conditions. *J. Phys. Chem. B*, 108(40):15873–15879, 2004.

[43] J. R. Schmidt and J. L. Skinner. Brownian motion of a rough sphere and the Stokes-Einstein law. *J. Phys. Chem. B*, 108(21):6767–6771, 2004.

[44] D. S. Bolintineanu, J. M. D. Lane, and G. S. Grest. Effects of functional groups and ionization on the structure of alkanethiol-coated gold nanoparticles. *Langmuir*, 30(37):11075–85, 2014.

[45] G. Plascencia-Villa, B. Demeler, R. L. Whetten, W. P. Griffith, M. Alvarez, D. M. Black, and M. José-Yacamán. Analytical characterization of size-dependent properties of larger aqueous gold nanoclusters. *J. Phys. Chem. C*, 120(16):8950–8958, 2016.

[46] A. Bekdemir and F. Stellacci. A centrifugation-based physicochemical characterization method for the interaction between proteins and nanoparticles. *Nat. Commun.*, 7:13121, 2016.

[47] L. Shang, L. Yang, F. Stockmar, R. Popescu, V. Trouillet, M. Bruns, D. Gerthsen, and G. U. Nienhaus. Microwave-assisted rapid synthesis of luminescent gold nanoclusters for sensing Hg^{2+} in living cells using fluorescence imaging. *Nanoscale*, 4(14):4155–4160, 2012.

[48] S. Khan, A. Gupta, N. C. Verma, and C. K. Nandi. Kinetics of protein adsorption on gold nanoparticle with variable protein structure and nanoparticle size. *J. Chem. Phys*, 143(16), 2015.

[49] K. Salorinne, T. Lahtinen, S. Malola, J. Koivisto, and H. Häkkinen. Solvation chemistry of water-soluble thiol-protected gold nanocluster Au_{102} from DOSY NMR spectroscopy and DFT calculations. *Nanoscale*, 6:7823–6, 2014.

[50] J. Tournebize, A. Boudier, O. Joubert, H. Eidi, G. Bartosz, P. Maincent, P. Leroy, and A. Sapin-Minet. Impact of gold nanoparticle coating on redox homeostasis. *Int. J. Pharm.*, 438(1-2):107–116, 2012.

[51] E. Casals, T. Pfaller, A. Duschl, G. J. Oostingh, and V. Puntes. Time evolution of the nanoparticle protein corona. *ACS Nano*, 4(7):3623–3632, 2010.

[52] J. P. Wilcoxon, J. E. Martin, and P. Provencio. Size distributions of gold nanoclusters studied by liquid chromatography. *Langmuir*, 16(25):9912–9920, 2000.

Chapter 4

Local hydrodynamics of solvent near diffusing dendrimers: An investigation into generality of the new Stokes-Einstein relation

4.1 Abstract

We have obtained a new Stokes-Einstein relation for size determination and tested it by various nanoparticles. We assumed that the breakdown of the Stokes-Einstein relation results from the local increases in the viscosity. Here we investigate hydrodynamics of solvent near dendrimers to further test the generality of our new theory. We discuss simulations of dendrimers in comparison to nanoparticles, experimental data on dendrimers from literatures, and the new theory. Local viscosity and local diffusivity of solvent near dendrimers are estimated by persistence times and exchange times, respectively. We find that the local dynamics of solvent near dendrimers of low density remains almost the same as that of bulk solvent, while the motions of solvent particles slow down near dendrimers of high density. This is similar with the changes in local dynamics of solvent near the nanoparticles. According to the causes we proposed for deviation of the Stokes-Einstein relation, this is consistent with our findings that the Stokes-Einstein relation works for the dendrimers of low density, while it fails for the dendrimers of high density. The new Stokes-Einstein relation is then tested and we find that it predicts sizes of the dendrimers accurately. Taking this together with the results for nanoparticles presented in Chapter 2 and 3, we believe that the new theory is general.

4.2 Introduction

Deviations from the Stokes-Einstein relation (SER) have been found for dendrimers, nanoparticles and proteins.[1–3] In Chapter 2, we assumed that mechanism for the breakdown is an increase in viscosity of solvent near particles, referred as local viscosity. The assumption was made based on the reports that local viscosity of fluids near flat surfaces and globular proteins is higher than that of bulk solvent.[3–6] We have derived a new Stokes-Einstein relation based on this assumption. The new theory improves the accuracy for size measurement of nanoparticles as presented in Chapter 2 and 3. Since dendrimers have important applications in biomedicine[7–9] and the related properties, such as diffusion and magnetics, are size dependent, a better size determination is demanded. Therefore, here we test our new theory using dendrimers of various densities to explore the generality of the new theory by using molecular dynamics simulations.

We hypothesize that dynamic heterogeneity of solvent exists near dendrimers of high density, but not near dendrimers of low density. The ligand-like structures of dendrimers have density profiles similar to those of ligands attached nanoparticles,[10–13] therefore, we raise this the hypothesis based on the confinement of liquids by ligands.[14–17] When the length of ligands or grafting density of ligands is high enough, the miscibility of grafted nanoparticles in polymer melts is promoted.[18, 19] This means that the polymers in matrix are confined inside the compact structures of ligands and then transport together with the particles. On the contrary, if the ligand length is much shorter than that of the free polymers, or the grafting density of ligands is low, an aggregation of the grafted nanoparticles happens.[20–22] This means that the loose structures of ligands are not able to confine the free polymers in matrix around them, thus the dynamics of polymer melts near the nanoparticles maintains the same as those of bulk liquid.

One possible factor which could influence the solvent heterogeneity is the interaction force between the dendrimers and solvent particles. Many theoretical studies[23–26] have reported the effects of the interaction force on the diffusion of solutes. The Lennard-Jones particles were found diffusing much slower when the interaction force changes from repulsive to attractive.[23] Nanoparticles were also found diffusing gradually slower when the interaction force changes from weakly to strongly attractive.[25, 26] The slow diffusion results from that the particles are dressed with solvent particles with high packing density. The layer which is in vicinity of a solute is called solvention shell. The shell is formed when the attractive force is strong enough[24, 27, 28]

The hypothesis could be tested by two time intervals, which are persistence times and exchange times. They can be used to estimate the local viscosity and local diffusivity of the solvent, respectively. To explore effects of interaction force on the dynamic heterogeneity of solvent, the two time intervals of solvent particles near the dendrimers are needed to be calculated under different interaction force parameters. In order to investigate the generality of the dynamic heterogeneity of solvent, we compare the two time intervals of solvent near dendrimers with those near nanoparticles. We thus simulate two types of dendrimers, which are simple and complex dendrimers, and two types of nanoparticles, which are bare nanoparticles and grafted nanoparticles. The two time distributions can be calculated by the sampled individual trajectories from the simulations. These simulations also allow us to calculate the traditional and new hydrodynamics radius. Comparisons between the hydrodynamic and structural sizes are employed to explore the validity of both the traditional and our new Stokes-Einstein relation.

In the following section, we describe the simulation models of dendrimers, bare nanopar-

ticles and grafted nanoparticles. The calculation methods of persistence times and exchange times are then presented. We then analyze local hydrodynamics of solvent near dendrimers, and compare them with those near bare and grafted nanoparticles, and we report a similarity between the local dynamics of solvent near dendrimers of high density and nanoparticles. The new Stokes-Einstein relation is finally discussed together with the data of our simulated and other's experimental dendrimers and other's simulated dendrimers. Note the models we employed in this chapter have been depicted in Chapter 2 and 3. With the same sampled trajectories, further analysis on these models are performed here. We thus describe the models only briefly in the following section.

4.3 Simulation methods

4.3.1 Model details

Molecular dynamics simulations have been performed in canonical (NVT) ensembles for various dendrimers as shown in Figure 4.1. Seven dendrimers are simulated in this study. The dendrimers are named by the generation number (GN) and branch length (M). The dendrimers of a single generation (G=1) possess low density and thus they will be termed as simple dendrimers in the following. The dendrimers of increasing generations (G>1) possess high density and thus they will be termed as complex dendrimers in the following. The two types of dendrimers reveal information on validity of the mechanism we proposed for the breakdown of Stokes-Einstein relation.

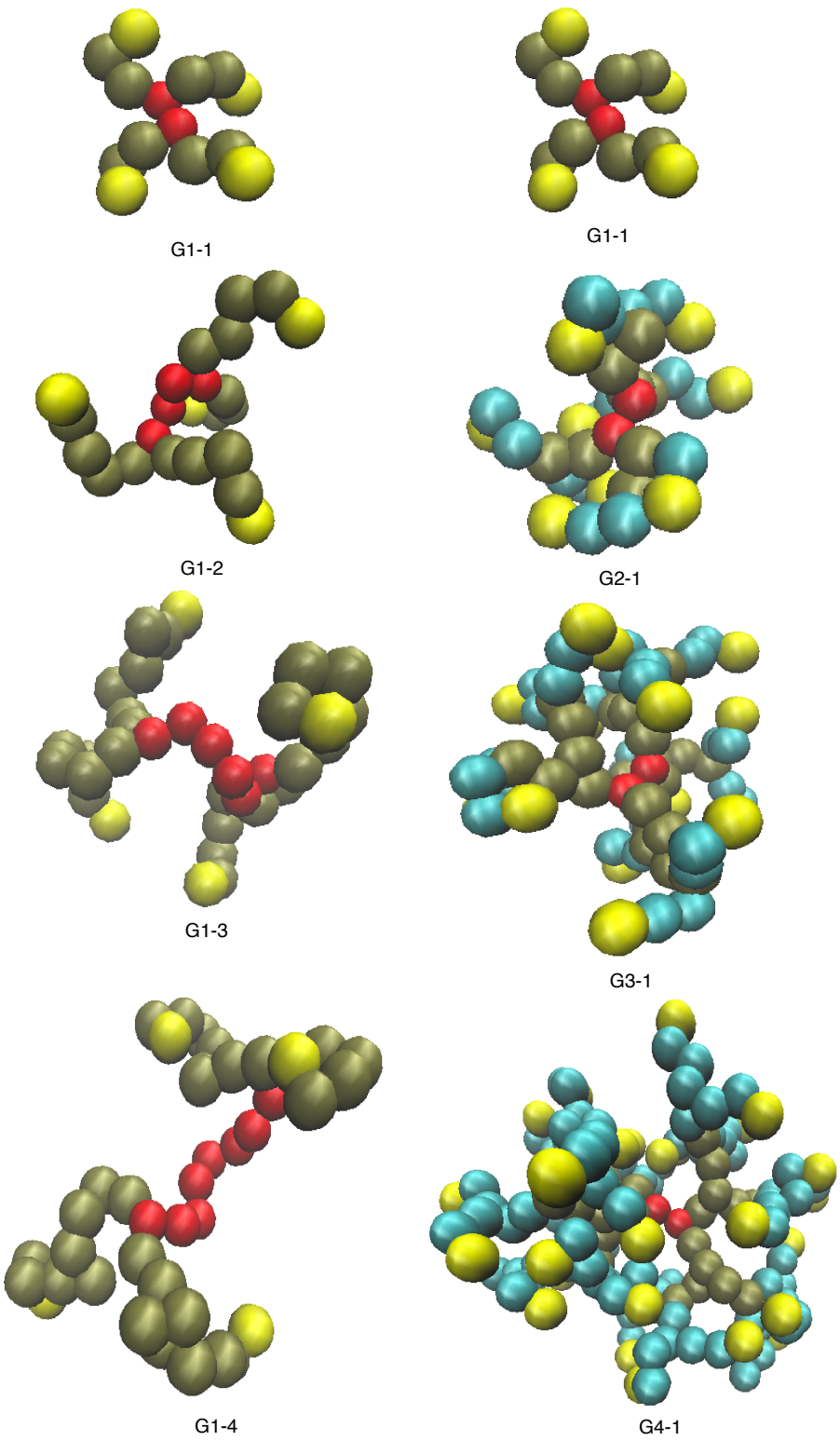

Figure 4.1: Snapshots of dendrimers with generic structures with formula GN-M. GN indicates the generation number and M is the length of a branch.

Soft spheres are used to mimic simple solvent for the dendrimers. Interactions between two neighbouring monomers of a dendrimer molecule are described by rigid bonds, and the monomers interact with solvent particles by the Lennard-Jones potential,

$$U_{ij}(r) = \begin{cases} 4\varepsilon[(\frac{\sigma}{r})^{12} - (\frac{\sigma}{r})^{6}] & r \leq r_c, \\ 0 & r > r_c. \end{cases} \tag{4.1}$$

Solvent particles interact with each other by the soft sphere potential,

$$U_{ij}(r) = \begin{cases} \varepsilon(\frac{\sigma}{r})^{12} & r \leq r_c, \\ 0 & r > r_c, \end{cases} \tag{4.2}$$

where $U_{ij}(r)$ is the potential between two atoms with r being the separated distance between the two atoms, ε is the interaction force parameter, σ is the length parameter and r_c is the cutoff radius.

The simulations of dendrimers were carried out in a cubic box under periodic boundary conditions. There are 2197 or 5832 atoms included in each dendrimer/solvent system with the box length being 16σ or 22.15σ, respectively. The time step is $\Delta t = 0.001 m^{\frac{1}{2}} \sigma \varepsilon^{-\frac{1}{2}}$ with m being the mass of an atom. The temperature is balanced by the Nosé-Hoover chain thermostat with a relaxation time of $\tau = 0.25$. Reduced units are used for the dendrimer simulations.

Two types of nanoparticle are also modeled to investigate the effects of structures on the local hydrodynamics of solvent. One is the bare nanoparticle as shown in Figure 4.2 (a). The system of one bare nanoparticle diffusing in solvent is simulated in a cubic box with periodic boundary conditions applied. There are 5324 particles included in each box with the

box length being 21.5σ. The bare nanoparticles are constructed by selecting atoms within a certain radius to the central coordinate. The atoms are held together by rigid bonds. Atoms of the bare nanoparticle interact with surrounding solvent particles by the Lennard-Jones potential. Any two solvent particles interact by soft sphere potential. The other type is gold nanoparticle grafted with alkanethiol ligands as shown in Figure 4.2 (b). The grafted nanoparticles are simulated by the NAMD package.[29] Solvent used for the grafted nanoparticles is water. The water is described by the TIP3P model.[30–32] The NAMD simulations are carried out in cubic boxes with periodic boundary conditions. The box length ranges from 40 to 70 $\mathring{A}$. The water density is checked to be consistent with that reported in the literature.[32] The cutoff radius for the force fields, taken from elsewhere,[33–36] is 12 Å, and all bonds are kept rigid. The time step is 2 fs. Particle Mesh Ewald sum is used for calculation of full-system electrostatic interactions with a grid size of 1 Å. The temperature of 310 K is controlled by langevin dynamics with a damping coefficient of 5 ps^{-1}.

More detials of the simulations of dendrimers and bare nanoparticles have been described in Chapter 2. The simulations of grafted gold nanoparticles were carried out following Heikkilä[37] and Lee's[38] work. More details have been described in Chapter 3. Same models as those in Chapter 2 and 3 have been employed in this chapter for further analysis of generality of the new Stokes-Einstein relation.

4.3.2 Local hydrodynamics from persistence and exchange times

As we have discussed in Chapter 2 and 3, local hydrodynamics of solvent can be described by two time intervals, persistence time, t_p, and exchange time, t_x. The two time intervals are defined for motions of a Continuous Time Random Walk. We only describe the method briefly in this chapter. t_p is calculated as the mean first passage time, which is the time taken by a solvent particle to reach a given distance from its start for the first time. t_x

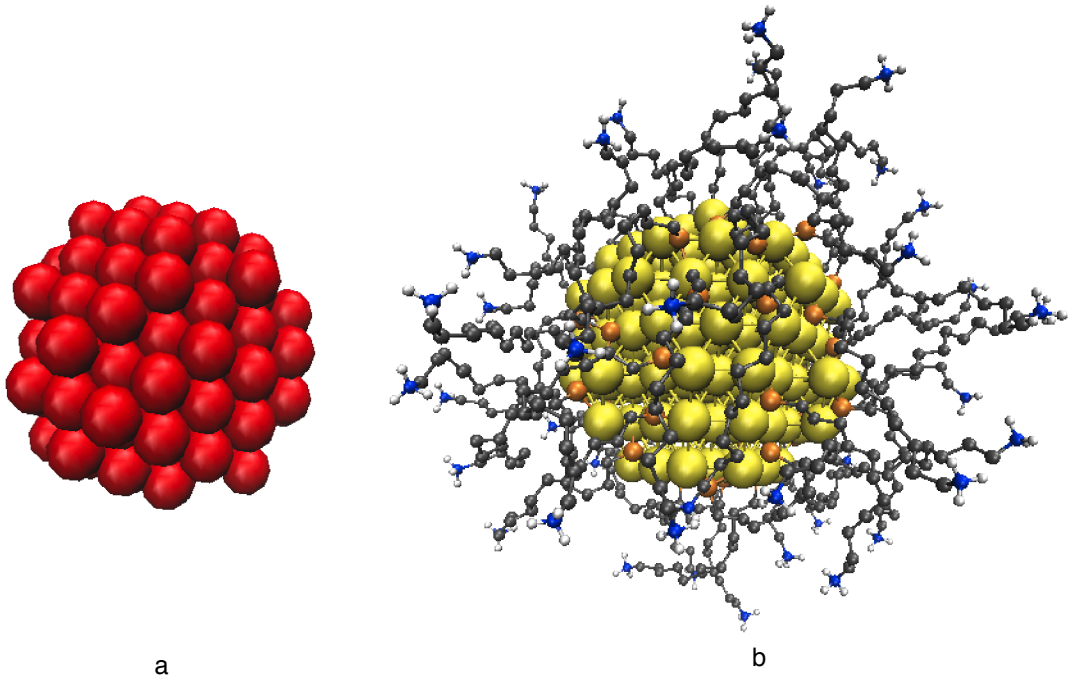

Figure 4.2: Snapshots of (a): a bare nanoparticle and (b):a gold nanoaparticle grafted by alkanethiol chains with positively charged terminal group $Au_{140}(SC_{12}H_{24})_{47}NH_3^+$, where gold atoms are represented in yellow, S in orange, C in gray, N in blue and H in white.

is the waiting time between two random walk jumps. A random walk jump occurs when a particle moved a given displacement, which is termed a jump length (d). The waiting time is calculated as the time taken by the particle between two successive random jumps in this simulation. The two types of time intervals have been illustrated by Figure 1.2 in Chapter 1. The jump length is chosen to be 1.1σ with σ being the length parameter for the dendrimers and bare nanoparticles, and 3 $\mathring{A}$ for the gold nanoparticles according to Pronk's justification.[3] The t_p and t_x are used here to estimate local viscosity and local diffusivity of solvent near the diffusing solutes, respectively,

$$\eta(r) \propto kT\langle t_p \rangle_r, \tag{4.3}$$

and

$$D(r) \propto \frac{1}{\langle t_x \rangle_r}, \tag{4.4}$$

where $\langle \cdot \rangle_r$ is the average over solvent particles at a distance r from the centre of mass of the solute, $D(r)$ is the diffusion coefficient of solvent particles at a distance r from the COM of solute and $\eta(r)$ is the local viscosity of the solvent also at a distance r.

In calculating the persistence and exchange times, we adopt a similar method described in Chapter 2 and 3, except that we use arithmetic average over all solvent particles in a divided bin for a single configuration (time frame) instead of harmonic average,

$$\langle t_p \rangle_{r,f} = \frac{\sum_{i=1}^{N_\mathrm{r}} t_p^i}{N_\mathrm{r}}, \tag{4.5}$$

and

$$\langle t_x \rangle_{r,f} = \frac{\sum_{i=1}^{N_\mathrm{r}} t_x^i}{N_\mathrm{r}}, \tag{4.6}$$

where f denotes the f^{th} time frame of trajectories in the simulation, i denotes the i^{th} solvent particle in the bin at a distance r from the COM of a solute, and N_r is the total number of the solvent particles inside the bin.

A harmonic average is then taken for the obtained persistence and exchange times of a bin across all time frames,

$$\langle t_p \rangle_r^{har} = \frac{N_\mathrm{f}}{\sum_{f=1}^{N_\mathrm{f}} \frac{1}{\langle t_p \rangle_{r,f}}}, \tag{4.7}$$

and

$$\langle t_x \rangle_r^{har} = \frac{N_\mathrm{f}}{\sum_{f=1}^{N_\mathrm{f}} \frac{1}{\langle t_x \rangle_{r,f}}}, \tag{4.8}$$

where N_f is the total number of the time frames. Local viscosities and diffusivity are then estimated from these persistence times and exchange times, respectively.

4.4 Results and discussion

We estimate the local dynamics of simple liquids near the diffusing dendrimers of various density profiles. The local dynamics investigated here includes viscosity and diffusivity, estimated by persistent times and exchange times, respectively. The behaviors of local time distributions are distinct between the dendrimers with a single generation and those with more than one generation. Note we refer to them as simple dendrimers and complex dendrimers, respectively, in the following. The simple dendrimers possess loose structures and the complex dendrimers possess compact structures as shown by the monomer density profiles in the following. We discuss local dynamics of solvent near dendrimers in comparison to those near nanoparticles. In order to test the new Stokes-Einstein relation, we compare the hydrodynamic radius of dendrimers with the corresponding structural radius of both simulated and real dendrimers.

4.4.1 Local diffusivity estimated by exchange times

We examine first the local diffusivity of solvent near all the seven dendrimers by the exchange time distributions as plotted in Figure 4.3. Note in this study we especially consider the local hydrodynamics of solvent near the surface of dendrimers, therefore, we need to approximately locate the surface. We estimate where the surfaces are from the atom density profiles. On approach to the surface of dendrimers from the bulk solvent, the exchange time

distributions of solvent particles keep constant near the simple dendrimers G1-1, G1-2, G1-3 and G1-4. It suggests that solvent particles near the simple dendrimers diffuse the same as those in the bulk liquid. Thus the diffusive motions of solvent are not confined by the branches of dendrimers with a single generation. This indicates that the solvent near the simple dendrimers is homogeneous.

In contrast, there are broadly raised areas of the exchange time profiles near the surface of complex dendrimers G2-1, G3-1 and G4-1. We observe ascending peaks as the generation number grows from 1 to 4 with the same branch length as shown in Figure 4.3. The solvent particles diffuse much slower near the surfaces than in the bulk. It means that the motions of solvent particles near the surface of complex dendrimers are confined and that the confinement becomes slightly more intense as the generation number increases. This suggests that the solvent near the three complex dendrimers are heterogeneous.

We observe distinct behaviors of the local diffusivity of solvent as the structures of dendrimers change. The structures are changed in two ways by varying the branch length and generation number. In order to further investigate the reason why the local diffusivity is different between the simple and complex dendrimers, we provide the structure details of all the dendrimers. Possible correlations between the density of dendrimers and the local diffusivity are investigated in the following section.

4.4.2 Local diffusivity and density profiles

As seen from Figure 4.3, the monomer density of simple dendrimers at the same distance r from the COM of dendrimers decreases as the branch length increases, corresponding to G1-1, G1-2, G1-3 and G1-4, respectively. This indicates looser and looser structures of the simple dendrimers, which could hardly confine the movements of solvent particles. The

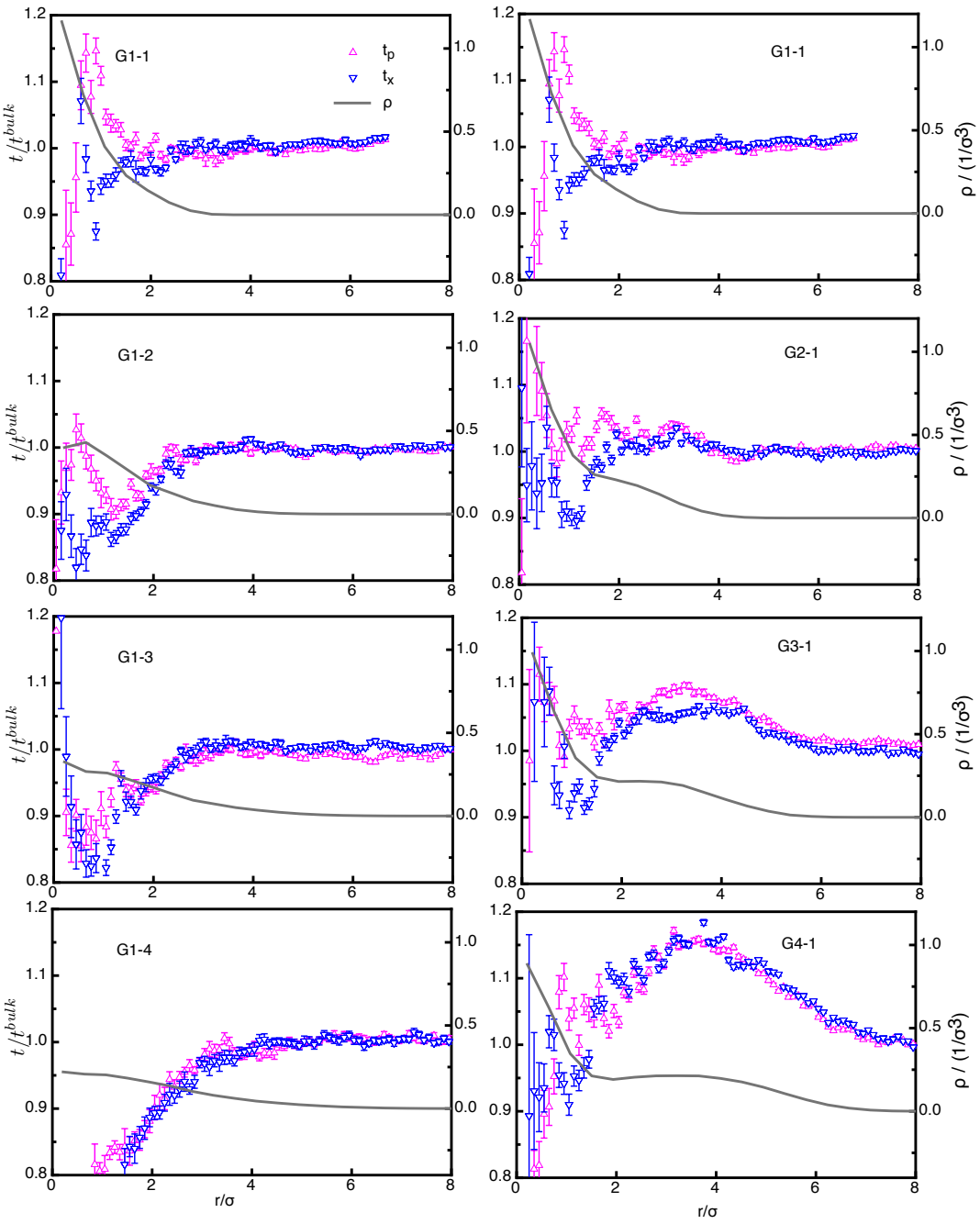

Figure 4.3: Local dynamics of solvent near dendrimers under $\epsilon = 1$. t_p is persistence time, t_x is exchange time, r is distance to the center of mass of dendrimers and ϵ is the interaction parameter. The error bars are plotted by standard deviation. The atom number densities are shown in solid curves.

nearly constant diffusivity reflected by the exchange times near the simple dendrimers could thus be explained.

While we do not observe the decrease of monomers density for the compact dendrimers as the size grows, corresponding to G2-1, G3-1 and G4-1. Instead, we see similar monomer density distributions at small r for all the four dendrimers. In addition, a plateau is observed near the surfaces close to the bulk solvent when the generation number increases to 2. It becomes longer as the generation number further increases, in agreement with that reported in the literature.[13] It shows that the monomer densities near the surface of the complex dendrimers G2-1, G3-1 and G4-1 close to the bulk solvent are higher than that near the simple ones G1-2, G1-3, and G1-4, respectively. The high monomer density of complex dendrimers favors confinement of motions of the solvent particles by frequent collisions. This explains the observed increases in the exchange times near the complex dendrimers.

Note where the increase in the local exchange times for the complex dendrimers happens covers the plateau of density profiles of G2-1, G3-1 and G4-1. The longer the plateau, the more barriers for the movements of solvent particles and thus the slower of the local diffusivity. We thus believe that it is this constant monomer density region that dominates the confinement of solvent particles near the surface of dendrimers.

4.4.3 Local viscosity estimated by persistence times

We further calculate the persistence times to estimate the local viscosity of solvent ss shown in Figure 4.3. We then compare them with the exchange time distributions in order to confirm the heterogeneity of solvent near the complex dendrimers.

As we can see, the persistence time distributions, beyond the surface of simple dendrimers,

keep constant as that of the bulk solvent. It suggests that there is no increase in the local viscosity near surface of the simple dendrimers. The persistence time distributions near the simple dendrimers almost overlap with the exchange time distributions except the area close to the center of mass of G1-1. It confirms that the hydrodynamics of solvent near the surfaces of simple dendrimers behaves the same as the bulk solvent.

We also observe similar distributions between the exchange times and persistence times near the complex dendrimers. They all begin to increase on approach to the surface of complex dendrimers from the bulk solvent, and reach to the maximum near the surface. This indicates a heterogeneity of solvent because of the decreases in the local diffusivity and increases in the local viscosity. We do not observe obvious decouple between exchange times and persistence times for G2-1, G3-1 and G4-1 as reported elsewhere for water near solid surfaces.[3]

Similar with the local diffusivity, the local viscosity of solvent near the simple dendrimers behaves the same with the bulk solvent, while the local viscosity increases near the complex dendrimers. Recall from our earlier work, the new Stokes-Einstein relation was solved based on an increased local viscosity. According to the new theory, the traditional Stokes-Einstein relation would apply successfully to the simple dendrimers, however it would fail for the complex dendrimers. The validity of the SER for the two types of dendrimers are tested in the following sections.

4.4.4 Effects of interaction parameter on local dynamics

In order to obtain a clear picture of the origin of the slow local hydrodynamics near the complex dendrimers, we change the interaction force between the monomers of dendrimers and solvent particles by increasing the interaction parameter ϵ from 1 to 4 in reduced units.

We calculate the exchange times and persistence times under $\epsilon = 4$ as shown in Figure 4.4. The exchange time and persistence time distributions are similar with each other for all the dendrimers investigated under the interaction parameter $\epsilon = 4$.

It shows distinct differences between the time distributions near the simple dendrimers and complex dendrimers. The time profiles increase slightly on approach to the surface of simple dendrimers from the bulk solvent. The amount of the increase is almost the same near the four simple dendrimers. While they increase much more near the complex dendrimers and again it illustrates higher increases when the generation number grows from 2 to 4. This indicates slower diffusivity and higher viscosity of solvent near the complex dendrimers than that near the simple dendrimers. These phenomena under $\epsilon = 4$ are the same as those under $\epsilon = 1$ except that the amount of increase in local dynamics is larger for all the dendrimers under $\epsilon = 4$ than that under $\epsilon = 1$.

4.4.5 Local hydrodynamics of solvent near nanoparticles

We employ the same average methods for the dendrimers to estimate the local hydrodynamics of solvent near both the bare and ligands grafted nanoparticles. The nanoparticles are comparable in sizes with the complex dendrimers as shown in Table 4.1. We estimate the local dynamics of solvent near the nanoparticles to investigate whether they are similar to those near the complex dendrimers in order to explore the generality of our new theory. The persistence times and exchange times of solvent particles near the bare nanoparticles and grafted gold nanoparticles are calculated as shown in Figure 4.5.

Both the persistence time and exchange time distributions near the bare nanoparticles are higher than those of the bulk solvent. The peaks become slightly higher as the size increases. It means slower local hydrodynamics, which is similar to that near the complex dendrimers.

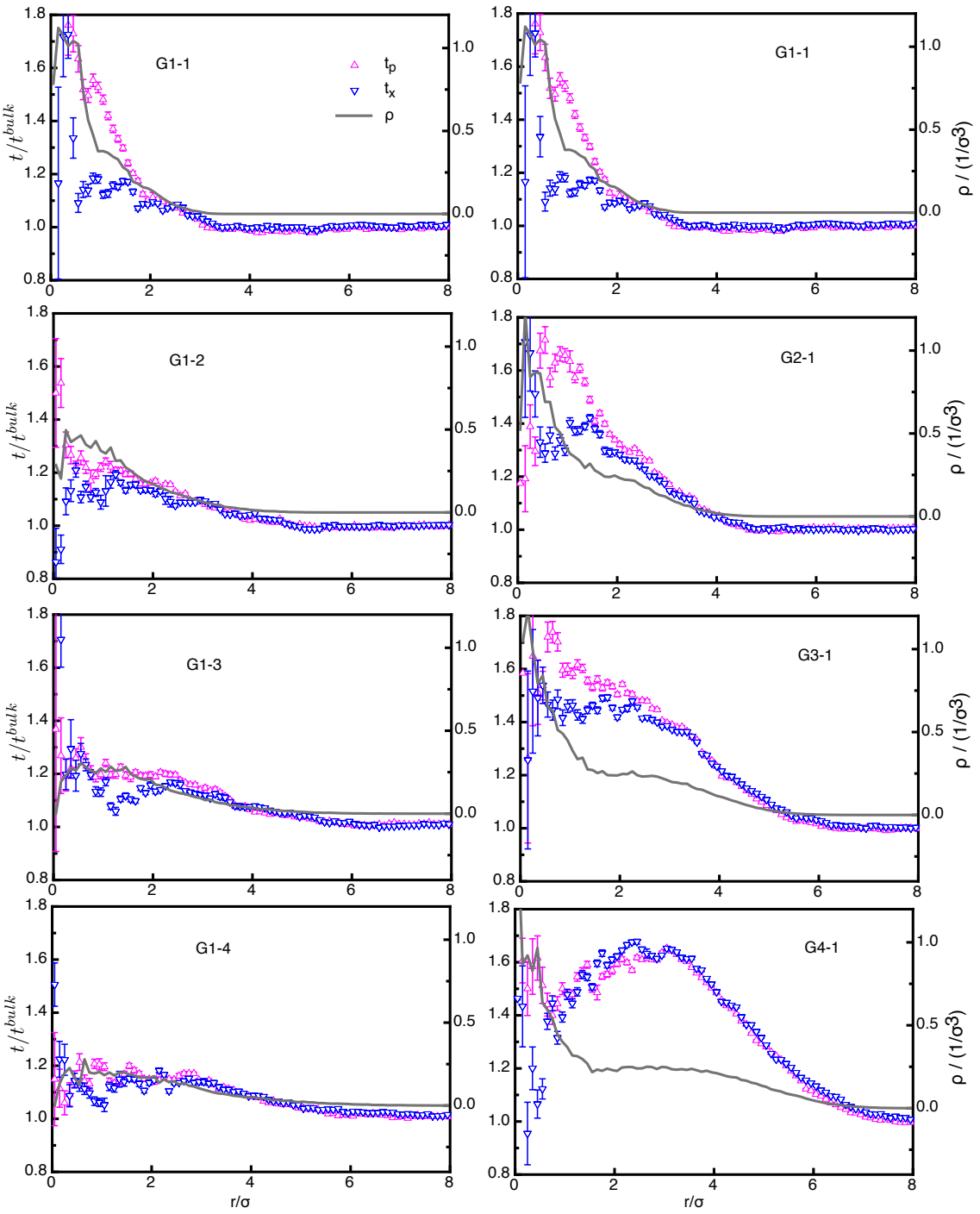

Figure 4.4: Local dynamics of solvent near dendrimers under $\epsilon = 4$. t_p is persistence time, t_x is exchange time, r is distance to the center of mass of dendrimers and ϵ is the interaction parameter. The error bars are plotted by standard deviation. The atom number densities are shown in solid curves.

Table 4.1: Radius of complex dendrimers, bare nanoparticles and grafted nanoparticles in reduced units. The radii of bare NPs and grafted AuNPs are scaled in order to compare with those of dendrimers. The radii of bare NPs in reduced units are multiplied by 1.7 and those of grafted AuNPs in $\mathring{A}$ are multiplied by $0.48/\mathring{A}$. Note here the size of grafted nanoparticles refers to the size of cores.

	R/σ		R/σ		R/σ
G1-1	1.76	bare NP 1	2.02	AuNP-16	1.87
G2-1	2.62	bare NP 2	2.75	AuNP-44	2.93
G3-1	3.52	bare NP 3	3.40	AuNP-80	3.70
G4-1	4.54	bare NP 4	4.15	AuNP-140	4.37

The persistence time and exchange time distributions of solvent near the diffusing gold nanoparticles with alkanethiol ligands also slightly increase as the size increases, even though the increase is not as distinct as those near the complex dendrimers and bare nanoparticles. The large errors near the grafted gold nanoparticles result from poor statistics of water molecules inside the ligands. We locate the peaks of the two time profiles for AuNP-16 at r $\approx$ 10 Å. The peaks become slightly higher for AuNP-44 and remain almost the same for AuNP-80 and AuNP-140.

We therefore see similar changes in hydrodynamics, which are increased local viscosity and decreased local diffusivity, of solvent near the complex dendrimers, bare nanoparticles and grafted nanoparticles. The changes in the local dynamics tend to be larger as the size of particles increases until reaching to the maximum, but this size dependence is weak.

The persistence time is the time any given microscopic structure is expected to persist.[3] The exchange time is equal to the persistence time for normal bulk liquids.[3, 39] The two time scales are thus determined by the changes in local structures of solvent. Any local interaction between the solvent particles and the surrounding particles could affect the changes in the persistence/exchange times. The two time scales increase near the three types of so-

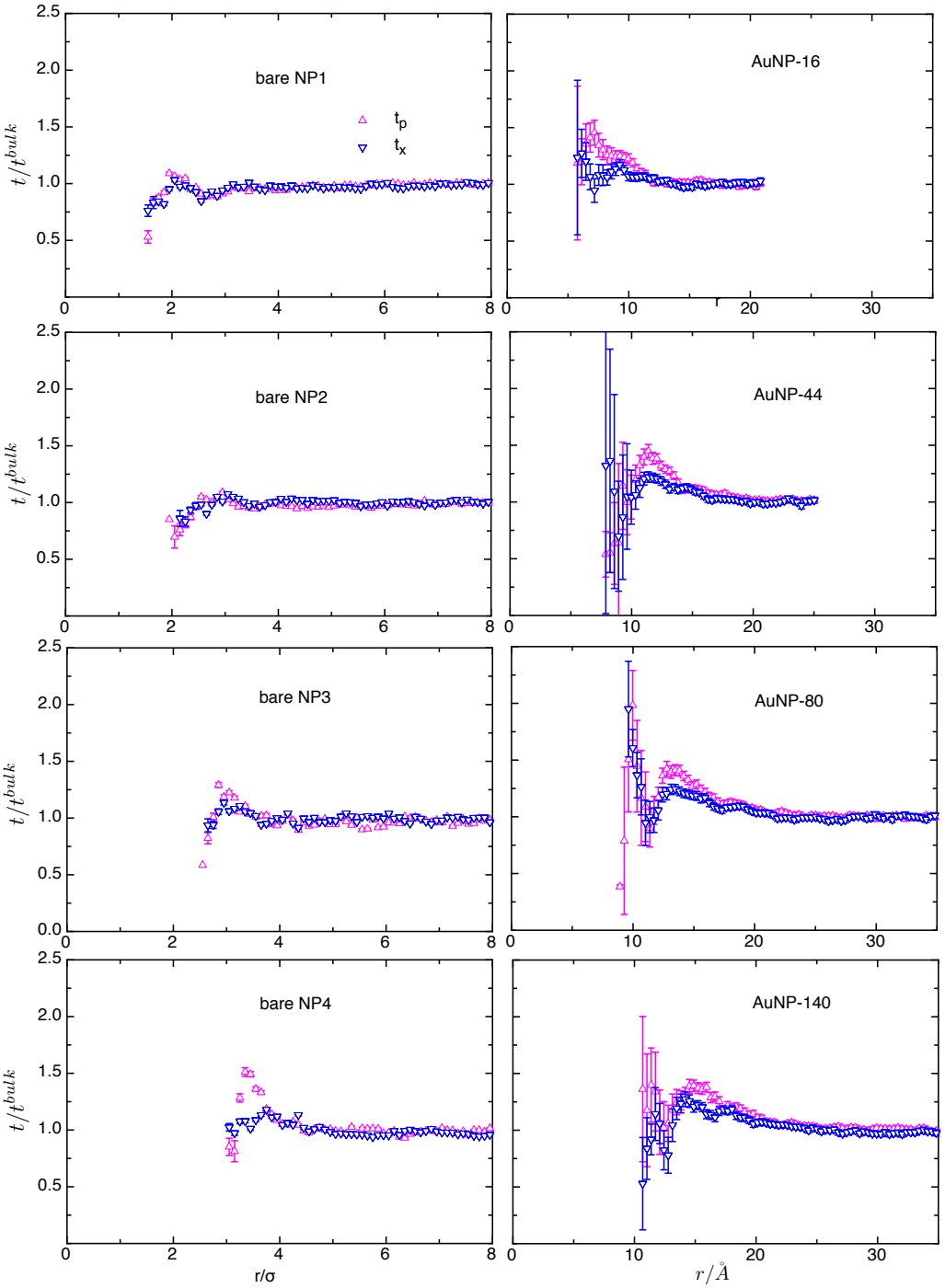

Figure 4.5: Local dynamics of solvent near bare nanoparticles (left column) and grafted nanoparticles (right column). t_p is persistence time, t_x is exchange time and r is the distance to center of mass of the nanoparticles. The error bars are plotted by standard deviation.

lute, which are complex dendrimers, bare nanoparticles and grafted nanoparticles, comparing with those of the bulk solvent. This phenomenon results from that interactions between the solute and solvent are different from those between pure solvent particles. The difference in interactions comes from the different structures. We now compare the difference between the structures of solutes to explore the determinant factor on the changes of the two local time scales. The three types of solute possess sufficient internal density and the the persistence times increase near them. While the simple dendrimers do not possess sufficient internal density and the persistence times keep nearly constant near them. Based on these facts, we believe that the interactions, which lead to the increases in the local time scales, are determined by the sufficient internal density of solutes.

For the complex dendrimers, the dense structures, where the solvent can diffuse into, constrain the motions of particles. Thus the dendrimers slow the dynamics of solvent nearby. The slowed dynamics is reflected by the increases in persistence times and exchange times. This could be interpreted by the relaxation of monomers. The monomers relax faster in loose structures, the simple dendrimers, than those in compact structures, the complex dendrimers. This indicates that the solvent particles moving into the branches of simple dendrimers experience more frequent effective collisions than those moving into the branches of complex dendrimers. The former is close to the fast motions of bulk solvent particles. The latter is related to the slow local dynamics of solvent. For the bare nanoparticles with structures where the solvent particles can barely diffuse into, the constrain on the motions of solvent nearby might result from attraction between the sufficient dense structures of bare nanoparticle and the surrounding solvent particles. For the grafted nanoparticles, both the physical constraints from the ligands and attraction from the core may contribute to the increases in the two time scales.

We note that the increased local viscosity might have similar physical effects with the draining effect resulting from hydrodynamic interaction between the monomers of ligand-like structures, including the dendrimers and grafted nanoparticles. The Kirkwood-Riseman theory assumes each monomer as a point source for the friction in solvent in considering the hydrodynamic interaction.[40, 41] The solvent particles "stick" inside the dense ligands-like structures by the friction and diffuse together with the solute at a slower rate than in the bulk solvent. The increased local viscosity is also reflected by the "slow" structures, suggested by that the persistence times and exchanges times near the complex dendrimers and grafted nanoparticles are much longer than those in the bulk solvent. However, the physical effects of the two are not equivalent due to that the increased local viscosity may also be contributed by other interactions between the solvent and solute apart from the hydrodynamic interaction. More details on the interactions between the solute and solvent are not investigated in this study and we leave it to the future research, due to that the validity of the new Stokes-Einstein relation only rely on the increases in the two time intervals regardless of the nature of interactions involved.

We hypothesized that the breakdown of Stokes-Einstein relation is caused by increases in the viscosity of solvent near a diffusing particle in a viscous fluid, and we modified the theory with this assumption to obtain a new Stokes-Einstein relation. In this section, we not only employ the persistence time to directly estimate the local viscosity, but also calculate the exchange time to confirm the slow dynamics. We thus independently provide confirmation for the assumption of the new Stokes-Einstein relation which we introduce again in the following part. With the similar increases in the local viscosity near the complex dendrimers, bare nanoparticles and grafted nanoparticles, we expect to see similar deviation from the Stokes-Einstein relation and also to see validity of the new theory for all of them. These have been confirmed for the bare and grafted nanoparticles as presented in Chapter 3. While for

the simple dendrimers, no evident increases in the local viscosity are observed by the two time intervals, therefore, we expect they obey the traditional Stokes-Einstein relation. In the following section, we thus examine these expectations by discussing the validity of the tradition Stokes-Einstein relation and the application of the new theory to the simple and complex dendrimers.

4.4.6 Hydrodynamic and structural radius

Recall our earlier work presented in Chapter 2, we modified the traditional Stokes' radius r_h and obtained the new hydrodynamic radius $\hat{r}_{\mathrm{h}}$ by allowing increases in local viscosity near a diffusing particle in a viscous liquid,

$$r_h = \frac{kT}{6\pi\eta_0 D}, \tag{4.9}$$

and

$$\hat{r}_{\mathrm{h}} = \frac{kT}{(6\pi\eta_0 + 4\pi\eta_0\Delta)D}, \tag{4.10}$$

where D is the diffusion coefficient of the particle, η_0 is the shear viscosity of bulk solvent, T is the absolute temperature, k is Boltzmann's constant and Δ is the dimensionless increase in viscosity. As described in Chapter 2, we expect the increase in local viscosity is zero, $\Delta = 0$, if the diffusing particle is in the same size with the surrounding solvent particles. When the size of solute grows, Δ decreases eventually to zero due to that the Stokes-Einstein relation (eq 4.9) is reported valid to predict size of macroscopic particles. Thus we believe that Δ must decay as the size of diffusing particle increases. The simplest equation meeting these requirements is,

$$\Delta = 4\alpha\frac{s}{a}\left(1 - \frac{s}{a}\right), \tag{4.11}$$

where α is the largest surface viscosity ratio increase seen for any particle size, a is the radius of an idealized spherical particle and s is the radius of a solvent particle. Note here the expression for Δ meets the physical constraints, but it might need further improvement for larger sizes. Our results are not sensitive to the choice of this formula over the size range studied here. We thus solve the new hydrodynamics radius $\hat{r}_{\mathrm{h}}$ by substituting eq 4.11 back to eq 4.10 and bringing a in agreement with $\hat{r_h}$,

$$\hat{r}_{\mathrm{h}} = \left(\frac{kT}{12\pi D\eta_0} - \frac{4\alpha s}{3}\right) + \sqrt{\frac{8}{3}\alpha s^2 + \left(\frac{kT}{12\pi D\eta_0} - \frac{4\alpha s}{3}\right)^2}, \tag{4.12}$$

where $\hat{r}_{\mathrm{h}}$ is a measured radius defined for a particle of arbitrary shape. It should be used in place of the usual SER for the size measurement for nanoparticles up to 10 nm.

We here apply the new Stokes-Einstein relation to the simple and complex dendrimers to test our expectations which are obtained based on the changes in the local viscosity and local diffusivity of solvent estimated by the persistence times and exchanges times, respectively. We utilize the comparison between hydrodynamic size and structural size of particles to examine the validity of Stokes-Einstein relation. If they equal to each other, the theory works; otherwise, it fails. Note here the structural size of dendrimers in this studies refers to the gyration of radius (R_g). The hydrodynamic radius is plotted against the corresponding structural radius of the simulated simple dendrimers (Figure 4.6(a)), the simulated complex dendrimers and real dendrimers (Figure 4.6(b)).

It shows that the hydrodynamic radii fall on the straight line for both $\epsilon = 1$ and 4 in Figure 4.6(a). It illustrates that the two sizes approximately equal to each other. Therefore, the Stokes-Einstein relation is valid for the simple dendrimers. This is consistent with our expectation from the local hydrodynamics estimated by the two time intervals according to

the new theory. Additionally, the weak heterogeneity near the simple dendrimers estimated by the slight increase in the local persistence times and exchange times under $\epsilon = 4$ is not intense enough to result in noticeable deviation from the Stokes-Einstein relation.

We continue to examine the complex dendrimers from both our simulations and experiments in the literature.[42] In Figure 4.6(b), the hydrodynamic radius r_h, calculated from the traditional Stokes-Einstein relation, grows much faster than the corresponding structural size R_g. In other words, the traditional Stokes-Einstein relation overestimates the sizes of complex dendrimers. This is consistent with our expectation obtained based on the heterogeneity of solvent near the dendrimers. We then plot the experimental size data of dendrimers polyamidoamine (PAMAM) from literature[42] to verify our simulation data. Appropriate agreement is found between the experiment and our simulations.

We now examine the validity of the new Stokes-Einstein relation for the three sets of complex dendrimers which deviate from the traditional Stokes-Einstein relation. In order to do so, the new hydrodynamic radius needs to be calculated to compare with the structural radius. Therefore, the values of s and α in eq 4.12 are required. For the simulated dendrimers, the traditional hydrodynamic radius is obtained by the simulation data, including diffusion coefficients of solutes and viscosity of solvent. The structural radius of dendrimers has been calculated by the trajectories sampled from the simulations. A continuous relation between the hydrodynamic radius and the structural radius can be solved from eq 4.9-4.11 by bringing $\hat{r_h}$ and a in agreement with R_g,

$$r_{\mathrm{h}} = R_g(1 + \frac{8s}{3R_g}\alpha(1 - \frac{s}{R_g})). \tag{4.13}$$

Fit eq 4.13 to the hydrodynamic-structural radius of the simulated complex dendrimers as

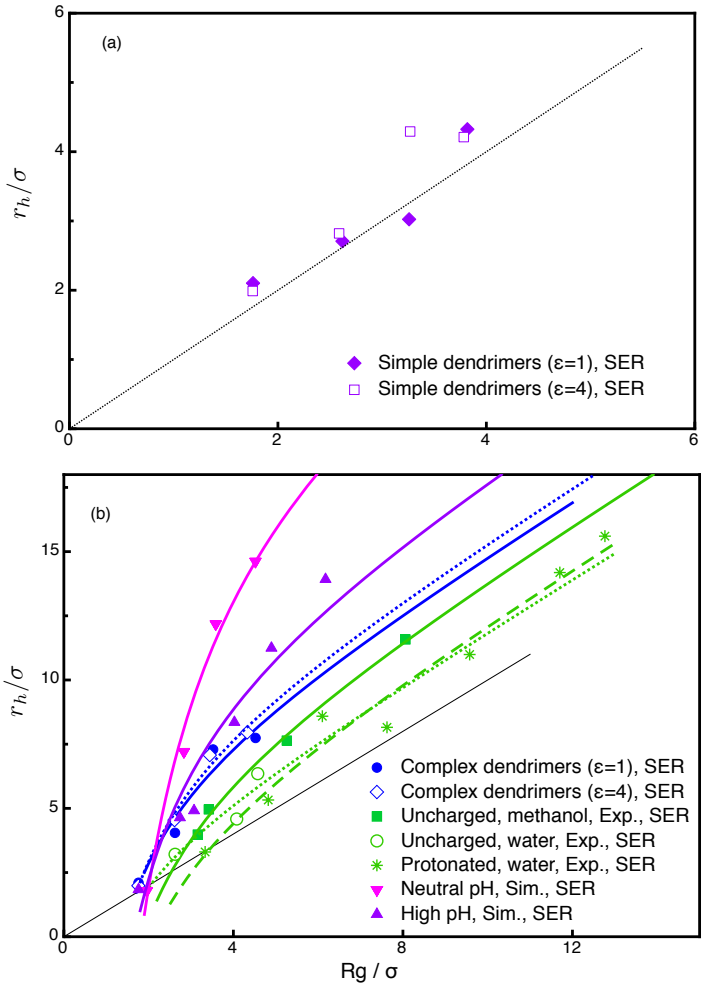

Figure 4.6: (a) Hydrodynamic radii of dendrimers G1-1,2,3,4 with fixed generation 1 by simulations. ϵ is the interaction force parameter. (b) Hydrodynamic radii ($r_{\rm h}$) of the dendrimers G1,2,3,4-1 with fixed branch length from simulations in comparison with dendrimers (PAMAM) in methanol from published experiments in green solid squares fitted by the green solid line,[42] in comparison with PAMAM in aqueous solution from published experiments in green circles fitted by dotted line[43] and green stars fitted by dashed line,[44, 45] and in comparison with those from published simulations[1] in purple and pink. Note here the $r_{\rm h}$ and R_g from literatures were scaled for clear comparisons. The curves are plotted from fitting eq 4.13 to the corresponding size data. The fitted parameters are shown in Table 4.2.

well as the dendrimers from experiments in the literature.[42] The two parameters α and s are obtained from the fitting as listed in Table 4.2. We have checked that the values of s are reasonably close to the size of solvent particles. Note here that the values of α close to each other is important for future practical applications of our new theory.

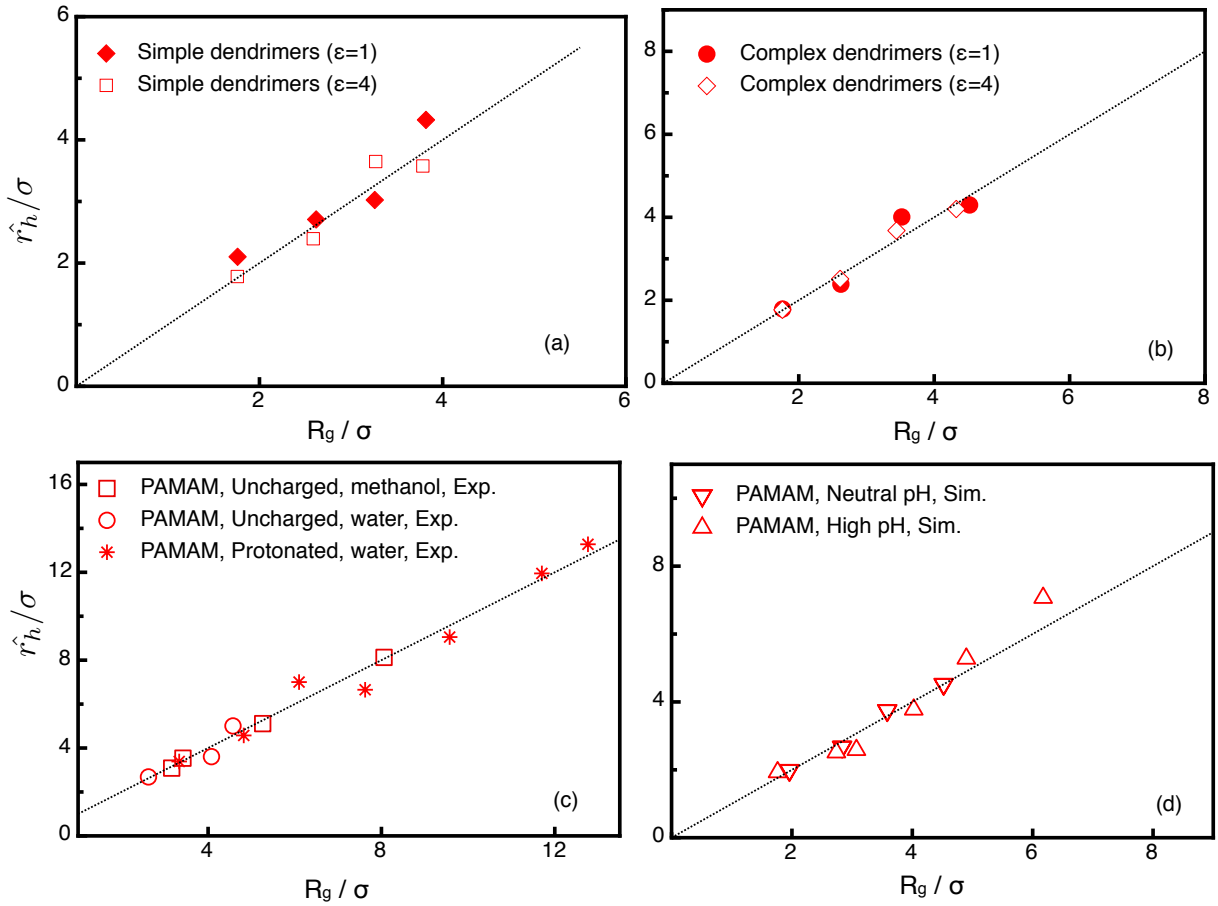

Figure 4.7: (a) The new hydrodynamic radii of the simple dendrimers; and (b) the new hydrodynamic radii of the complex dendrimers; and (c) the new hydrodynamic radii of PAMAM from experiments in literatures; and (d) the new hydrodynamic radii of PAMAM from simulations in literatures. The PAMAM are the same ones as shown in figure 4.6 (b). The new hydrodynamic radii are calculated by eq.4.12 using the fitted parameters α and s.

It has been reported that the size of dendrimers is influenced by different pH values.[1, 43, 46–50] We ignore this in the simple model of dendrimers without atom details, and so did the cited experimental size data of dendrimers. The experimental data closely match the simulation data. We now plot the size data from the simulations and experiments in literatures[1, 42–45] to test the possible effects of pH on the modified Stokes-Einstein. As shown in Figure 4.6 (b), the size data of simulated PAMAM under high pH values appropriately match the sim-

ulations in this study. While those under neutral pH value with protonated amine sites stay further above our simulated dendrimers without protonation. The hydrodynamic sizes of experimental dendrimers without charges are located a distance below those of our simulated hydrodynamic sizes, but the hydrodynamic sizes of the experimental and simulated dendrimers are still comparable. We apply the same fitting procedures to the two sets of simulation data in literature with high and neutral pH values as well as to those of uncharged and protonated PAMAM in aqueous solution from experiments in literature. The fitted dashed and dotted lines in green suggest that when the generations increases, the hydrodynamic radius of the protonated PAMAM grows slightly faster than the gyration radius. The effects of protonation on the size obtained in the experiments are not as significant as those observed in the simulations. The fitted parameters are listed in Table 4.2 for calculation of the new hydrodynamic radius.

The eq 4.12 and 4.13 are equivalent. Both are solved from eq 4.9-4.11 and thus both can represent the the new theory. Eq 4.12 is the true size as a function of hydrodynamic radius, and eq 4.13 is the hydrodynamic radius as a function of the true size. Therefore, the successful fittings in Figure 4.6 (b) show agreement between the simulation data, experiment data and the new theory. This implies that eq 4.12 can predict the true size correctly for the dendrimers under different pH values. With the known values of α and s obtained from the fitting, we are able to explicitly calculate the new hydrodynamic radius $\hat{r_h}$ of all the dendrimers using eq 4.12 as shown in Figure 4.7 (a) and (b). We see the new hydrodynamic radii of both simple and complex dendrimers fall on the straight line $\hat{r_h} = R_g$. This means that our new theory predicts the structural size accurately and absolutely improves the size determination for dendrimers.

The results of the neutral dendrimers in our simulations, and the neutral and protonated

dendrimers from both simulations[1] and experiments[42–45] in the literature indicate that the modified Stokes-Einstein relation works well for systems with changes in pH. This is true for the investigated systems in this study, but further study might be needed to explore more accurate effects of pH on the new theory for large size regime.

It remains to examine the magnitude in the local viscosity from the modified Stokes-Einstein relation using eq 4.11. With the fitted values of the two parameters α and s, the local viscosity-size curves are plotted for our simulated dendrimers and the experimental dendrimers in the literature[42] as shown in Figure 4.8. The local viscosity is $\sim$2 times of the bulk viscosity near the three sets of complex dendrimers. The values for dendrimers under $\epsilon = 4$ are slightly larger than that under $\epsilon = 1$. The increase in local viscosity near the experimental dendrimers is 1.5$\sim$2 times of the bulk viscosity. This suggests appropriate agreement between the simulation and experiment. The increased local viscosity inferred from the new theory is thus in appropriate consistence with that estimated independently by the persistence times mentioned above, even though the two are not exactly the same.

Table 4.2: Parameters of α and s in eq 4.11 and 4.12.

	α	s/σ
Complex dendrimers ($\epsilon = 1$)	1.26 $\pm$0.19	1.7
Complex dendrimers ($\epsilon = 4$)	1.39$\pm$0.10	1.7
Simulated PAMAM with high pH	1.82$\pm$0.22	1.9
Simulated PAMAM with neutral pH	3.39$\pm$0.22	2.0
Experimental uncharged PAMAM in methanol	1.04$\pm$0.27	1.0
Experimental uncharged PAMAM in aqueous solution	0.42$\pm$0.19	2.1
Experimental protonated PAMAM in aqueous solution	0.34$\pm$0.07	3.5

We also fit eq 4.13 to the hydrodynamic-structural radius of simple dendrimers. The fitted values of α are small which are $\sim$0 under $\epsilon = 1$ and $\sim$0.28 under $\epsilon = 4$. This means that the maximum increases in local viscosity is fairly small, in agreement with the estimations

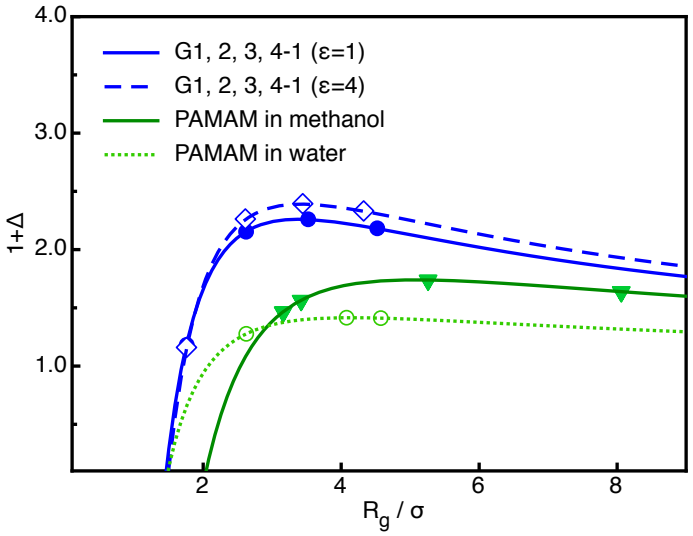

Figure 4.8: Curves of ratio of bulk viscosity to local viscosity $(1 + \Delta)$ as a function of R_g for the complex dendrimers from both simulations and experiments[42, 43] plotted by eq 4.11. The symbols indicate the increased local viscosity near a particular dendrimer.

by the persistence times.

We recall that we observed similar heterogeneity of solvent near complex dendrimers, bare nanoparticles and grafted nanoparticles with protonated amine group at the end of ligands and similar deviation from the Stokes-Einstein relation for them. Most importantly, our new theory is valid to predict true sizes of them. The three types of particles in nanoscale can represent nanoparticles with various structural features, including soft, solid, core-shell, neutral and charged particles. Taking together these results, we would say that the mechanism we proposed for the breakdown of the Stokes-Einstein relation is general and our new theory is also general.

4.5 Conclusion

Heterogeneity in solvent is detected near the diffusing complex dendrimers possessing compact structures, while the solvent is found homogeneous near the diffusing simple dendrimers

possessing loose structures. The results support the hypothesis on the dynamic heterogeneity of solvent near the two types of dendrimers. The mechanism of the breakdown for SER we proposed is then confirmed by the two types of dendrimers.

We find agreement among our simulations, experiments in literatures and our theory for the complex dendrimers. The generality examination of the new theory has to be limited to a certain number of nanoparticles. Here we have tested it by as many types of nanoparticles as we could. We thus conclude that the new theory is general for size determination of nanoparticles up to 10 nm.

We obtain this conclusion based on molecular dynamics simulation of four types of particles. They are a sequence of dendrimers of one single generation, a sequence of dendrimers of increasing generations, a sequence of bare nanoparticles of increasing sizes and a sequence of gold nanoparticles with alkanthiol ligands of increasing sizes. Simulations on these particles allow us to directly detect local dynamics of solvent near solute by persistence times and exchange times; to examine effects of interaction force between solute and solvent on the local dynamics; to observe similarities of local dynamics of solvent near nanoparticles of different structures; to show the validity and breakdown of the traditional Stokes-Einstein relation; and finally to find an appropriate agreement between our simulations, experiments from literature and the new theory for the dendrimers.

Taking together the results in this study and those in our earlier study, the validity of the new theory is observed for objects of different structures, including dendrimers of various monomer densities, bare nanoparticles and grafted nanoparticles with or without charges. The interactions between the solvent and solute are different for each of the studied objects. The new SER works well for the size determination in present of different interactions. We

thus believe that the nature of interactions, including those might not be described by the conventional hydrodynamic interactions, is not the dominant factor on the validity of the new SER. We, therefore, leave further investigation on the nature of interactions, which might help to understand the mechanism of the increased local viscosity, to future study.

In addition, the complex dendrimers possess core structures formed by soft branches. This implies that the new Stokes-Einstein relation could be applied to particles with soft cores including proteins and nanoparticles with cores formed by polymers. The size measurement would be improved for a wide range of nanoparticles by the new theory.

Bibliography

[1] P. K. Maiti and B. Bagchi. Diffusion of flexible, charged, nanoscopic molecules in solution: Size and pH dependence for PAMAM dendrimer. *J. Chem. Phys.*, 131(21):214901, 2009.

[2] X. Zhang, S. Tran, and A. A. Gray-Weale. The hydrodynamic drag on diffusing nanoparticles for size determination. *J. Phys. Chem. C*, 120(38):21888–21896, 2016.

[3] S. Pronk, E. Lindahl, and P. M. Kasson. Dynamic heterogeneity controls diffusion and viscosity near biological interfaces. *Nat. Commun.*, 5(3034):1, 2014.

[4] H. Hoang and G. Galliero. Local viscosity of a fluid confined in a narrow pore. *Phys. Rev. E: Stat. Nonlin. Soft Matter Phys.*, 86(2):1, 2012.

[5] L. Pozhar. Structure and dynamics of nanofluids: Theory and simulations to calculate viscosity. *Phys. Rev. E*, 61(2):1432, 2000.

[6] D. Ortiz-Young, H. Chiu, S. Kim, K. Voïtchovsky, and E. Riedo. The interplay between apparent viscosity and wettability in nanoconfined water. *Nat. Commun.*, 4(2482):1, 2013.

[7] C. C. Lee, J. A. MacKay, J. M. J. Fréchet, and F. C. Szoka. Designing dendrimers for biological applications. *Nat. Biotechnol.*, 23(12):1517, 2005.

[8] W. Tian and Y. Ma. Theoretical and computational studies of dendrimers as delivery vectors. *Chem. Soc. Rev.*, 42(2):705, 2013.

[9] J. S. Chahal, O. F. Khan, C. L. Cooper, J. S. Mcpartlan, J. K. Tsosie, L. D. Tilley, S. M. Sidik, R. Langer, S. Bavari, H. L. Ploegh, J. S. Chahal, O. F. Khan, C. L. Cooper, J. S. Mcpartlan, and J. K. Tsosie. Dendrimer-RNA nanoparticles generate protective immunity against lethal Ebola, H1N1 influenza, and Toxoplasma gondii challenges with a single dose. *Proc. Natl. Acad. Sci. U.S.A.*, 113(35):E5250, 2016.

[10] M. Ballauff and C. N. Likos. Dendrimers in solution: Insight from theory and simulation. *Angew. Chem. Int. Ed. (English)*, 43(23):2998, 2004.

[11] G. Del Río Echenique, R. R. Schmidt, J. J. Freire, J. G. Hernández Cifre, and J. García De La Torre. A multiscale scheme for the simulation of conformational and solution properties of different dendrimer molecules. *J. Am. Chem. Soc.*, 131(24):8548, 2009.

[12] S. Falkovich, D. Markelov, I. Neelov, and A. Darinskii. Are structural properties of dendrimers sensitive to the symmetry of branching? Computer simulation of lysine dendrimers. *J. Chem. Phys.*, 139, 2013.

[13] M. Muratt and G. S. Grest. Molecular dynamics study of dendrimer molecules in solvents of varying quality. *Macromolecules*, 29(4):1278–1285, 1996.

[14] F. Lo Verso, L. Yelash, and K. Binder. Dynamics of macromolecules grafted in spherical brushes under good solvent conditions. *Macromolecules*, 46(11):4716, 2013.

[15] F. Lo Verso, L. Yelash, S. A. Egorov, and K. Binder. Interactions between polymer brush-coated spherical nanoparticles: The good solvent case. *J. Chem. Phys.*, 135(21):214902, 2011.

[16] S. Goyal and F. A. Escobedo. Structure and transport properties of polymer grafted nanoparticles. *J. Chem. Phys.*, 135(18):184902, 2011.

[17] K. Binder and A. Milchev. Polymer brushes on flat and curved surfaces: How computer simulations can help to test theories and to interpret experiments. *J. Polym. Sci. B: Polym. Phys.*, 50(22):1515, 2012.

[18] C. Chevigny, F. Dalmas, E. Di Cola, D. Gigmes, D. Bertin, F. Boué, and J. Jestin. Polymer-grafted-nanoparticles nanocomposites: Dispersion, grafted chain conformation, and rheological behavior. *Macromolecules*, 44(1):122, 2011.

[19] J. Kalb, D. Dukes, S. K. Kumar, R. S. Hoy, and G. S. Grest. End grafted polymer nanoparticles in a polymeric matrix: Effect of coverage and curvature. *Soft Matter*, 7(4):1418, 2011.

[20] V. Ganesan and A. Jayaraman. Theory and simulation studies of effective interactions, phase behavior and morphology in polymer nanocomposites. *Soft Matter*, 10:13, 2014.

[21] Georgios G. Vogiatzis and Doros N. Theodorou. Structure of polymer layers grafted to nanoparticles in silica–polystyrene nanocomposites. *Macromolecules*, 46(11):4670, 2013.

[22] D. L. Green and J. Mewis. Connecting the wetting and rheological behaviors of poly(dimethylsiloxane)-grafted silica spheres in poly(dimethylsiloxane) melts. *Langmuir*, 22(23):9546, 2006.

[23] G. Srinivas, S. Bhattacharyya, and B. Bagchi. Computer simulation and mode coupling theory study of the effects of specific solute–solvent interactions on diffusion: Crossover from a sub-slip to a super-stick limit of diffusion. *J. Chem. Phys.*, 110(9):4477, 1999.

[24] J. R. Schmidt and J. L. Skinner. Brownian motion of a rough sphere and the Stokes–Einstein law. *J. Phys. Chem. B*, 108(21):6767, 2004.

[25] Z. Li. Critical particle size where the Stokes-Einstein relation breaks down. *Phys. Rev. E*, 80(6):061204, 2009.

[26] S. A. Egorov. Anomalous nanoparticle diffusion in polymer solutions and melts: A mode-coupling theory study. *J. Chem. Phys.*, 134(8):084903, 2011.

[27] D. I. Svergun, S. Richard, M. H. Koch, Z. Sayers, S. Kuprin, and G. Zaccai. Protein hydration in solution: Experimental observation by x-ray and neutron scattering. *Proc. Natl. Acad. Sci. U.S.A.*, 95(5):2267–2272, 1998.

[28] H. Ma. Density dependence of the entropy and the solvation shell structure in supercritical water via molecular dynamics simulation. *J. Chem. Phys.*, 136(21):0, 2012.

[29] L. Kalé, R. Skeel, M. Bhandarkar, R. Brunner, A. Gursoy, N. Krawetz, J. Phillips, A. Shinozaki, K. Varadarajan, and K. Schulten. NAMD2: Greater scalability for parallel molecular dynamics. *J. Comput. Phys.*, 151:283–312, 1999.

[30] W. L. Jorgensen, J. Chandrasekhar, J. D. Madura, R. W. Impey, and M. L. Klein. Comparison of simple potential functions for simulating liquid water. *J. Chem. Phys.*, 79(2):926, 1983.

[31] Y. Sun and P. A. Kollman. Hydrophobic solvation of methane and nonbond parameters of the TIP3P water model. *J. Comput. Chem.*, 16(9):1164, 1995.

[32] D. Paschek. Temperature dependence of the hydrophobic hydration and interaction of simple solutes: An examination of five popular water models. *J. Chem. Phys.*, 120(14):6674, 2004.

[33] O. Lopez-Acevedo, J. Akola, R. L. Whetten, H. Grönbeck, and H. Häkkinen. Structure and bonding in the ubiquitous icosahedral metallic gold cluster $Au_{144}(SR)_{60}$. *J. Phys. Chem. C*, 113:5035, 2009.

[34] H. Heinz, R. A. Vaia, B. L. Farmer, and R. R. Naik. Accurate simulation of surfaces and interfaces of face-centered cubic metals using 12-6 and 9-6 Lennard-Jones potentials. *J. Phys. Chem. C*, 112(44):17281, 2008.

[35] J. Hautman and M. L. Klein. Simulation of a monolayer of alkyl thiol chains. *J. Chem. Phys.*, 91(8):4994, 1989.

[36] P. Kr. Ghorai and S. C. Glotzer. Molecular dynamics simulation study of self-assembled monolayers of alkanethiol surfactants on spherical gold nanoparticles. *J. Phys. Chem. C*, 111(43):15857, 2007.

[37] E. Heikkilä, A. A. Gurtovenko, H. Martinez-Seara, H. Häkkinen, I. Vattulainen, and J. Akola. Atomistic simulations of functional Au_{144} $(SR)_{60}$ gold nanoparticles in aqueous environment. *J. Phys. Chem. C*, 116(17):9805–9815, 2012.

[38] O. Lee and G. C. Schatz. Molecular dynamics simulation of {DNA}-functionalized gold nanoparticles. *J. Phys. Chem. C*, 113:2316, 2009.

[39] David Chandler and Juan P. Garrahan. Dynamics on the way to forming glass: Bubbles in space-time. *Rev. Phys. Chem.*, 61:191–217, 2010.

[40] R Zwanzig, J Kiefer, and G H Weiss. on the Validity of the Kirkwood-Riseman Theory. *Proc. Natl. Acad. Sci. U.S.A.*, 60(2):381, 1968.

[41] John G. Kirkwood and Jacob Riseman. The intrinsic viscosities and diffusion constants of flexible macromolecules in solution. *J. Chem. Phys.*, 16(6):565–573, 1948.

[42] B. M. Tande, N. J. Wagner, M. E. Mackay, C. J. Hawker, and M. Jeong. Viscosimetric, hydrodynamic, and conformational properties of dendrimers and dendrons. *Macromolecules*, 34(24):8580, 2001.

[43] Verónica A. Jiménez, José A. Gavín, and Joel B. Alderete. Scaling trend in diffusion coefficients of low generation G0-G3 PAMAM dendrimers in aqueous solution at high and neutral pH. *Struct. Chem.*, 23(1):123–128, 2012.

[44] Yun Liu, Chun Yu Chen, Hsin Lung Chen, Kunlun Hong, Chwen Yang Shew, Xin Li, Li Liu, Yuri B. Melnichenko, Gregory S. Smith, Kenneth W. Herwig, Lionel Porcar, and Wei Ren Chen. Electrostatic swelling and conformational variation observed in high-generation polyelectrolyte dendrimers. *J. Phys. Chem. Lett.*, 1(13):2020–2024, 2010.

[45] Emilio Garcia-Fernandez and Pedro M R Paulo. Deswelling and electrolyte dissipation in free diffusion of charged pamam dendrimers. *J. Phys. Chem. Lett.*, 5(8):1472–1478, 2014.

[46] Juan J Freire, Ana M Rubio, and Carl Mcbride. Calculation of Conformational Properties and Rouse Relaxation Times of PAMAM-EDA Dendrimers under Different pH Conditions. *Macromol. Theory. simul.*, 25:403, 2016.

[47] Seungho Lee, Hai Doo Kwen, Sung Kwang Lee, and Sachin Vilas Nehete. Study on elution behavior of poly(amidoamine) dendrimers and their interaction with bovine serum albumin in asymmetrical flow field-flow fractionation. *Anal. Bioanal. Chem.*, 396(4):1581–1588, 2010.

[48] Prabal K. Maiti, Tahir Çağin, Shiang Tai Lin, and William A. Goddard. Effect of solvent and pH on the structure of PAMAM dendrimers. *Macromolecules*, 38(3):979–991, 2005.

[49] I Lee, B D Athey, a W Wetzel, W Meixner, and J R Baker. Structural molecular dynamics studies on polyamidoamine dendrimers for a therapeutic application: Effects of pH and generation. *Macromolecules*, 35(11):4510–4520, 2002.

[50] Mallory A Van Dongen, Bradford G Orr, and Mark M Banaszak Holl. Diffusion NMR Study of Generation-Five PAMAM Dendrimer Materials. *J. Phys. Chem. B*, 118:7195, 2014.

Chapter 5

Conclusions and outlook

In determining the size of spherical objects undergoing Brownian motions in a flow with low Reynolds number, the Stokes-Einstein relation (SER) is widely applied. The size of macroscopic spherical particles has been well predicted by the SER. However, as the resolution of equipments increases for the size measurement, the breakdown of the SER is found for particles smaller than 10 nm,[1–3] such as quantum dots, nanoparticles, proteins and dendrimers. This results from the neglect of consideration of the microscopic parameters. Potential applications, which are based on size dependent properties, of the small particles are limited by the failure of size determination. A new relation between the size and drag is thus needed for a better size measurement of the sub-10 nm particles. The heterogeneity of liquids has been detected previously near proteins by numerical methods,[4] and it was suggested as the origin of deviation of the SER for proteins.[5] Here we explore an accurate solution for the size determination of small particles diffusing in viscous liquids, based on the dynamical heterogeneity of solvent near the solute. In this thesis, we have presented a revised SER, and tested it using various types of model particles, which are bare nanoparticles, ligand grafted nanoparticles and dendrimers. The predicted sizes from the new theory are compared with the size data obtained from both simulations and experiments in literature.

In Chapter 2, a new expression of the SER is derived from solving the Navier-Stokes equations by assuming an increase in the local solvent viscosity near a diffusing spherical object. The traditional SER is also obtained from solving the Navier-Stokes equations but use the viscosity of pure solvent. The new drag force obtained here indicates that the deviation of traditional SER results from the shear forces rather than the normal force between the solute and solvent. We test this point of view by simulating the bare single-sited nanoparticles with smooth surfaces diffusing in simple liquids, so there is no tangential force exerted on the surface of the nanoparticles by the solvent. We find that they obey the traditional SER as expected. We further simulate the bare nanoparticles of rough surfaces. The rough nanoparticles are composed of a number of atoms. Both tangential and normal forces are exerted on the rough surfaces. It is found that the traditional SER fails in predicting their sizes. The two sets of bare nanoparticles show that the changes in the shear viscous forces lead to the failure of the traditional SER, in agreement with the new solution of the drag force in this study.

In order to test the validity of the new theory in predicting size of spherical particles in a few nanometers, we produce hydrodynamic radius vs. structural radius plots of a sequence of simulated bare single-sited nanoparticles, a sequence of simulated bare composite nanoparticles, three sequences of simulated complex dendrimers G1,2,3,4-1, a sequence of simulated simple dendrimers G1-1,2,3,4 and a sequence of experimental CdSe quantum dots. Similar deviations of the traditional SER are found for the bare composite nanoparticles, complex dendrimers and quantum dots. Their hydrodynamic radii grow much faster than the structural radii. While the true size of the simple dendrimers and bare single-sited nanoparticles are correctly predicted by the traditional SER. The interaction forces between the solute and solvent influence the extent of deviation only weakly based on the comparison between

the three sets of complex dendrimers under different interaction parameters. In addition, the ligands are found not the essential factor leading to the failure of the SER, as concluded from the comparison between the bare composite nanoparticles and core-shell nanoclusters (CdSe quantum dots). Furthermore, the high internal density of a solute is found relevant to the failure of the SER, as concluded from the comparison between the compact dendrimers G2,3,4-1 and loose dendrimers G1-1,2,3,4.

We apply the new SER to the particles aforementioned, and find agreements among our theory, our simulations and other's experiments. Our theory provides a continuous relation between the traditional Stokes' radii and the structural radii with two parameters, which are the radius of solvent particles (s) and the maximum increase in local viscosities of solvent near the solute (α). The two parameters are obtained from fitting our theory to the discrete data. With the two known parameters, the deviated Stokes' radii are corrected to the true sizes, with a purpose to improve the size measurement of nanoparticles up to 10 nm.

The assumption of increased viscosity for the new theory is then examined by the persistence times. The persistence times are reported to be proportional to the local viscosities. We thus estimate changes in the local viscosities of Lennard-Jones liquids near the simulated bare composite nanoparticles and dendrimers using the persistence times theory. We observe similar changes in the local viscosities of solvent near all the bare composite nanoparticles. They all increase to the maximum of ~ 1.3 times and ~ 2 times of the pure viscosity of solvent estimated by two different averaging methods, respectively. The value of increases in the local viscosities estimated by the persistence times are consistent with that inferred from our new SER. We also detect increases in the local viscosities of solvent near the dendrimers, but the changes are not as clear as those near the composite nanoparticles. We further investigate the local viscosities near the dendrimers in Chapter 4. Most importantly the

assumption of an increased local viscosity, made when solving the Navier-Stokes equations, is independently confirmed. We find that the deviations of traditional SER for predicting the size of nanoparticles up to 10 nm are consistent with the increases in local viscosities.

We have tested our new theory using the simple models in Chapter 2. In Chapter 3, we further test it using more realistic models considering atomic details, which are alkanethiol ligands passivated gold nanoparticles diffusing in the TIP3P water, simulated by the NAMD package. The essential prerequisite for the validity of the new SER is an increased local viscosity of solvent near the solutes. We employ the persistence times to estimate the local viscosities of water near the diffusing ligands grafted gold nanoparticles. The results show that the changing trends are similar near all the investigated gold nanoparticles. The local viscosities increase to the maximum, ~ 3 times of the viscosity of pure water, on approach to the center of mass of the grafted nanoparticles. Taking together the results of local viscosity near the bare and grafted nanoparticles, we conclude that the ligands strengthen the increase in the magnitude of local viscosity, even though they are not the essential cause for the increased viscosity.

The role of ligands in the local viscosities is further investigated. The results suggest that the innermost sulfur atoms push the solvent a certain distance away from the core surface, and the alkane groups and nitrogen atoms increase the magnitude of local viscosities, but with the alkane groups being dominant. We obtain this conclusion by comparing the sulfur, carbon and nitrogen atoms profiles with the persistence time profiles based on our assumption that atoms affect the persistence times most strongly in a small region around their position. The nature of interactions between the atoms and water are not further explored, because it does not influence the applicability of the new SER in this study. We emphasize the result that the dynamic heterogeneity of solvent produces the observed size-drag relation.

The effect is similar in the presence of different interactions. We leave a more detailed study of the interactions to future work.

The hydrodynamic radius of simulated gold nanoparticles with ligands is obtained by correcting the diffusion coefficient calculated from the MSD method. We plot them against their structural radius and then compare them with the hydrodynamics radius of the bare composite nanoparticles simulated in Chapter 2. The plot shows that hydrodynamic radius of the two types of nanoparticles grow much faster than the corresponding structural radii. Thus the SER fails for them. The extent of deviation for the grafted gold nanoparticles are slightly larger than that for the bare nanoparticles. This agrees with the role of ligands in the local viscosities. We then directly apply our new theory to the two types of simulated nanoparticles as well as the experimental nanoparticles with given size of solvent particles, s. The maximum values of the local viscosities, α, obtained from fitting our new theory to the discrete size data, is consistent with those estimated from the persistence times. Agreements are further found among simulations, experiments, and the new theory. We test the new SER against gold nanoclusters in two different solvents, toluene and water. The maximum increase in the local viscosities is found ~ 2 times of the viscosity of pure solvent by the new theory. This is consistent with those near the simulated gold nanoparticles inferred from the new theory and also agrees with those estimated from the persistence times. With the known s and α, we correct the deviated sizes successfully to the corresponding true structural sizes by the new theory. This shows that the new method leads to better size estimation when it is applied to real nanoparticles.

In Chapter 4, the same dendrimers simulated in Chapter 2 are further analyzed in terms of the changes in the local dynamics of solvent. We adopt a different averaging method from that applied in Chapter 2 for calculating the persistence times. We confirm the changes in

the local motion of solvent particles by both persistence times and exchange times. Two sequences of dendrimers, simple dendrimers G1-1,2,3,4 and complex dendrimers G2,3,4-1, are investigated. The local viscosity and diffusivity keep nearly constant near the simple dendrimers, while increases in the local viscosity and decreases in the local diffusivity of solvent are observed near the complex dendrimers. This indicates that the high internal density has an effect on increasing the magnitude of local viscosities as concluded in Chapter 2. We also studied the dendrimers under different interaction parameters ($\epsilon = 1$ and 4) between solute and solvent particles. The changing pattens in local dynamics are similar under these two interaction forces near a same dendrimer but with slight difference between the magnitude. This suggests that the interactions between the solute and solvent only weakly affect deviation of the SER.

We found that the changes in the local dynamics of solvent near the complex dendrimers are similar to those near the nanoparticles. This result is obtained from comparisons among the complex dendrimers, bare and grafted nanoparticles. The simulation details are presented in Chapter 2 and 3. The local time intervals increase to the maximum near all the three types of solutes. The similar increasing patterns of local viscosities of solvent are observed near solutes of both soft and solid internal structures. This indicates that the mechanism we propose for the deviation of SER, which is an increased local viscosity, is sound.

The results of hydrodynamic radius and structural radius show that the simple dendrimers obey the traditional SER. This is consistent with the nearly constant local viscosities, estimated by the persistence times, according to the assumption of mechanism for the deviation of SER. While deviation of the SER for the complex dendrimers, indicated by larger hydrodynmic radius than the structural radius, happens. This is also consistent with the increases in the local viscosities. We then apply the new SER to the simulated simple dendrimers,

simulated complex dendrimers under two different interaction parameters, simulated complex dendrimers under different pH values and experimental complex dendrimers. Fitting the continuous relation between the hydrodynamic radius and structural radius to the discrete size data, we obtain values of the maximum increase in local viscosities. They are in agreement with those estimated from the persistence times and exchange times. Finally, the Stokes' size of the simple and complex dendrimers are revised by the new SER, and we successfully obtain the true size of all the investigated dendrimers. This study indicates that the new SER is general.

Finally, the potential future directions which might be used to further test the new SER and improve the size determination of nanoparticles may be fulfilled by simulating metal nanoparticles in nonpolar solvent, such as hexane, in comparison to those in polar solvent, such as water. The local dynamics and validity of the new theory might be influenced by the polarity of solvent. Much remains to be studied about the hydrodynamic behaviors of solute and solvent from such a comparison. Another possible way to further test and improve our new theory is to simulate dendrimers with specific atomistic details in realistic solvents instead of the Lennard-Jones liquids. Proteins should also be investigated in the same way as nanoparticles and dendrimers to further test the new SER. The third possible direction may be the role of the nature of interactions between a solute and surrounding solvent in the deviation of SER. Even though we have detected increased local viscosities and confirmed the validity of the new theory regardless of the nature of interactions for the investigated particles, further studies on the nature of interactions might help to determine the origin of the increased local viscosity and thus understand the mechanism of deviation of Stokes' law to a deeper level.

In summary, this study presents a new theory for the size measurement of sub-10 nm objects

tested by simple particles in the first place. Then the validity of the new theory is further examined by more realistic nanoparticles. Finally, the results of dendrimers together with various types of nanoparticles suggest that the new theory is general. The mechanism we propose for the deviation from the traditional SER is an increased local viscosity of solvent. The increases are consistent between those estimated by the persistence times and those inferred by the new SER near the investigated objects throughout the three chapters. It is not possible to explore all existing objects in the size range where the traditional SER fails. Thus examinations of the generality of our theory have to be limited to certain objects. We have investigated as many types of particles as we could in this thesis, including bare nanoparticles, quantum dots, ligand grafted gold nanoparticles and dendrimers. They represent a wide range of objects, including those with compact, loose, soft, solid, charged, neutral and core-shell structures. The accuracy of size determination for the sub-10 nm objects would be significantly improved by the new Stokes-Einstein relation.

Bibliography

[1] E. E. Lees, M. J. Gunzburg, T. L. Nguyen, G. J. Howlett, J. Rothacker, E. C. Nice, A. H. A. Clayton, and P. Mulvaney. Experimental determination of quantum dot size distributions, ligand packing densities, and bioconjugation using analytical ultracentrifugation. *Nano Lett.*, 8(9):2883–2890, 2008.

[2] B. Demeler, T. L. Nguyen, G. E. Gorbet, V. Schirf, E. H. Brookes, P. Mulvaney, A. O. El-Ballouli, J. Pan, O. M. Bakr, A. K. Demeler, B. I. Hernandez Uribe, N. Bhattarai, and R. L. Whetten. Characterization of size, anisotropy, and density heterogeneity of nanoparticles by sedimentation velocity. *Anal. Chem.*, 86(15):7688–7695, 2014.

[3] R. P. Carney, J. Y. Kim, H. Qian, R. Jin, H. Mehenni, F. Stellacci, and O. M. Bakr.

Determination of nanoparticle size distribution together with density or molecular weight by 2D analytical ultracentrifugation. *Nat. Commun.*, 2(335):1, 2011.

[4] S. Pronk, E. Lindahl, and P. M. Kasson. Dynamic heterogeneity controls diffusion and viscosity near biological interfaces. *Nat. Commun.*, 5(3034):1, 2014.

[5] B. Halle and M. Davidovic. Biomolecular hydration: From water dynamics to hydrodynamics. *Proc. Natl. Acad. Sci. USA*, 100(21):12135–12140, 2003.